Collisional Redistribution of Light

in the Mercury–Krypton System.

by

Daniel Martin Segal. BSc.

A thesis submitted in partial fulfilment of the
requirements for the degree of Doctor of Philosophy
of the University of London.

March 1988.

Blackett Laboratory
Imperial College
London SW7 2BZ
England

Abstract.

We have performed experiments in which the polarization of collisionally redistributed near resonant light has been monitored. An excited state of an atom irradiated with near resonant light may be populated if that atom is undergoing collisions. The excited state relaxes yielding light at the resonant frequency and this light is said to have been collisionally redistributed. (Burnett 1985)

If the incident light is polarized the fluorescent light may also be, with the degree of polarization of the fluorescent light depending on the collision dynamics. Our experimental results have been analysed using a molecular model (Lewis *et al.* 1983) for the collision. In this model the atom-perturber complex is excited into a molecular orbital which rotates through the collision. The complex then decouples and the atom radiates at a later time. The rotation experienced during the collision accounts for the depolarization of the light. A knowledge of the interatomic potentials for the system under study is necessary for a quantitative application of the theory. There exist other effects that cause depolarization but are not related to the collision dynamics and care has been taken to allow for these effects in a sensible way.

Previous experiments have been performed in Sr–RG and Ba–RG (Alford *et al.* 1984) systems however the interatomic potentials were not well known for those systems. The 2537Å ($^3P_1$—$^1S_0$) line in Hg perturbed by Kr was chosen for the present work since the interatomic potentials for this system are well documented (eg. Fuke *et al.* 1984, Grycuk & Czerwosz 1981) making a quantitative test of the model possible.

To achieve tunable light near 2537Å the output of a high power dye laser system was frequency doubled in a LFM crystal. The use of short (5ns) pulses and gateable photon counting electronics, with the attendant gain in signal to noise ratio, has enabled us to perform a sensitive experiment in the ultra violet. We have plotted a curve of polarization of the redistributed light against detuning from resonance in the red wing. We have also measured the polarization of the redistributed light at two specific detunings in the blue wing.

We show the primitive form of the molecular model to be inadequate to account for our experimental results quantitatively. In order that the molecular model be worthy of pursuit it should however, be widely applicable and should survive, with little modification, reasonable changes in the system studied. Hg($^3P_1$—$^1S_0$)–Kr must be regarded as a system in which the applicability of the molecular model is marginal since it depends on the excited state interatomic potentials being well separated in the region of interest. Extensions and modifications to the model that overcome some of these difficulties have been put forward by Bieniek (1987).

Contents.

Chapter 1. Page

Introduction.

1.1 Historical Background. 12
1.2 Motivation For The Present Work. Hg($^3P_1$—$^1S_0$)–Kr as a Prototype System. 18
1.3 Thesis Outline. 19

Chapter 2

Theory.

2.1 Introduction. 21
2.2 Theory of Line Broadening by Nonresonant Collisions with Neutrals. 21
2.2.1 Fourier Transforms, Timescales and Interatomic Forces. 21
2.2.2 The Impact Limit of the Lineshape. 26
2.2.3 The Quasistatic Limit of the Lineshape. 29
2.2.4 A Molecular Approach to the Quasistatic Lineshape. 32
2.2.5 Satellites. 35
2.3 Collisional Redistribution. 37
2.3.1 Introduction. 37
2.3.2 The Molecular Model: General. 39
2.3.3. Choice of R_{dc}. 40
2.3.4. Formulation of the Molecular Reorientation Model. 43
2.3.5 Calculation of the Polarization of the Collisionally Redistributed Fluorescence. 47
2.3.6. The Average Over Collisions. 51
2.3.7. Parameterization in Terms of R_α/R_{dc}. 51

Chapter 3.

Interatomic Potentials.

3.1. Introduction. 54
3.2. Interatomic Potentials : General. 56
3.2.1. Dispersion Energy. 56
3.2.2. Short Range Repulsion; Methods for Calculation of the Potential. 60
3.2.3. Useful Analytic Forms. 61
3.2.4. Determination of Interatomic Potentials from the Spectroscopy of van der Waals Molecules. 62
3.2.5 Estimation of the Well Depth Under the Assumption of a Morse Potential. 62
3.2.6. The Rydberg-Klein-Rees (RKR) Inversion Method. 64
3.2.7. Combining Rules for the Determination of ϵ and r_m. 65
3.2.8. Determination of the Potential From Other Sources of Data .. 66
3.3 Interatomic Potentials for Hg-Kr. 67
3.3.1 General Remarks. 67
3.3.2 Potentials Proposed by Fuke *et al.* (1984). 69
3.3.3 Potentials Proposed by Grycuk and Czerwosz (1981). 74
3.3.3a. Experimental and Theoretical Approach. 74
3.3.3b Ground State Potential. 75
3.3.3c Excited State Potentials. 78
3.4 Summary ; Proposed Potentials for Hg-Kr. 80
3.4.1 Ground State. 80
3.4.2. Excited State $A^3 0^+$. 81
3.4.3. Excited State $B^3 1$. 82
3.4.4. Resulting Potentials. 82

Chapter 4.

Experimental Apparatus and Method.

4.1 Introduction. 86
4.2 Overview of the Apparatus. 86

4.3 Lasers and Optics. 88
4.3.1 Pump Laser. 88
4.3.2 Dye Laser: General. 89
4.3.3 Oscillator. 89
4.3.4 Amplifier Chain. 93
4.3.5 Dye Laser Performance. 94
4.3.6 Frequency Doubler. 94
4.3.7 Optical System: Layout and Alignment. 95
4.3.8 Polarization Rotator. 97
4.4 Cells. 97
4.4.1 Heated Filter Cell. 97
4.4.2 Experimental Cell. 98
4.5 Data Acquisition and Control. 100
4.5.1 Photomultiplier. 100
4.5.2 CAMAC: General. 101
4.5.3 Pulse Delay Generator (PDG). 101
4.5.4 Analogue to Digital Converter (ADC). 104
4.5.5 Photon Counting: PM Amplifier, Discriminator and Scaler. ..104
4.6 Signal Level. 105
4.6.1 Line–centre Signal. 105
4.6.2 Detuned Signal. 108

Chapter 5.

Data Correction and Results.

5.1. Introduction. 111
5.2 Time-Dependent, Finite-Pressure Correction. 111
5.2.1 Theoretical Background. 111
5.2.2 Application to the Case of Hg-Kr. 113
5.3 Depolarization as a Result of Hyperfine Structure. 115
5.4 Depolarization as a Result of Radiation Trapping. 119
5.5 Depolarization of Resonance Fluorescence by External Magnetic Fields (The Hanle Effect). 121
5.6 Corrected Data. 126

5.6.1 Competition Between Depolarizing Processes: Timescales. ... 126
5.6.2. Application of the Theory of Radiation Trapping to our Experimental Geometry. ... 127
5.6.3 Experiment to Determine the Correction for Radiation Trapping. ... 129
5.6.4 Corrected Red Wing Detuning Data. ... 129
5.6.5 Blue Wing Detuning Data. ... 131

Chapter 6.

Analysis.

6.1 Introduction : Qualitative Features. ... 133
6.2 Quantitative Analysis Performed by Lewis *et al.* of Sr–Ar Results. ... 133
6.3 Mercury – Krypton Analysis. ... 138
6.3.1 Impact Limit Polarization. ... 138
6.3.2 Choice of R_{dc} for Hg-Kr. ... 140
6.3.3 Polarization Curve for Hg–Kr; Red Wing. ... 141
6.3.4 Blue Wing. ... 143
6.4 Extensions to the Molecular Model. ... 145
6.5 Beyond the Molecular Model. ... 146
6.5.1 Validity of Approximations. ... 146
6.5.2 Classical Trajectories and Quasistatic Excitation. ... 148
6.5.3 Excitation, Reorientation and Decoupling. ... 149

Chapter 7

Conclusions and Suggestions for Further Work.

7.1 Summary. ... 151
7.2 Conclusions. ... 152
7.3 Suggestions for Further Work. ... 153
7.3.1 Improvements to the Experimental set up. ... 153
7.3.2 Further Experiments. ... 154

List of Figures.

Chapter 1. Page

1.1 Collision perturbing energy levels. 13
1.2 Schematic redistribution experiment. 15
1.3 The Lowest Energy Levels in Hg. 18

Chapter 2.

2.1 Phase interruptions in the Impact Approximation. 27
2.2 Satellite associated with a minimum in the difference potential. 36
2.3 Transition between $|\Sigma\rangle$ and $|\Pi\rangle$ character during a collision. 42
2.4 Schematic potentials for a $^1P_1$–$^1S_0$ transition. 44
2.5 Geometry in the collision plane. 45
2.6 Orbital reorientation during a collision. 46
2.7 Experimental geometry. 48
2.8 Variation of polarization with X_α. 53

Chapter 3.

3.1 Typical interatomic potential: parameters used in Chapter 3. .. 55
3.2 Geometry for calculating the van der Waals interaction between two H atoms in their ground states. 58
3.3 Fluorescence excitation spectrum of Hg–Kr in a supersonic free jet in the vicinity of the Hg $^3P_1$—$^1S_0$ line. 70
3.4 Plots of $\Delta G_{v'+1/2}$ vs. v' for (a) A and (b) B states of Hg($^3P_1$—$^1S_0$)–Kr. 72
3.5 X,A and B state potentials after Fuke *et al.* (1984). 73
3.6 Reduced absorption coefficient for the red wing of the Hg 2537 Å line in the presence of $1.9 \times 10^{19} at/cm^3$ of Kr. 76
3.7 Transmission of a cell containing a mixture of Hg and Kr. 77
3.8 Hg($^3P_1$—$^1S_0$)–Kr ground and excited state potentials after Grycuk & Czerwosz (1981). 79
3.9 Potentials to be used in molecular model calculations. 84

3.10 Difference potentials based on the potentials of figure 3.9. 85

Chapter 4.

4.1 Experimental layout. 87
4.2 Laser System. 90
4.3 Dye laser calibration curve. 92
4.4 Frequency spread of tunable ultra violet output. 99
4.5 Block diagram of data acquisition and experimental control system. 102
4.6 Pulse timing. 103
4.7 Transient digitizer plots of line centre signal. 106

Chapter 5.

5.1 Plot of $1/\beta$ vs. pressure for Sr($^1P_1$–$^1S_0$)–Ne. 114
5.2 Plot of $1/\beta$ vs. pressure for Hg($^3P_1$—$^1S_0$)–Kr. 116
5.3 The origin of depolarization via radiative trapping. 120
5.4 Geometry for the theoretical description of the Hanle effect. 123
5.5 Decay of alignment via secondary collisions and the Hanle effect. 125
5.6 Experiment to determine degree of radiative trapping. 130
5.7 Red wing polarization data. 132

Chapter 6.

6.1 Ba–Xe interatomic difference potential, polarization spectrum and line shape. 134
6.2 Polarization redistribution spectrum for the red wing of Sr–Ar: Comparison with theory. 135
6.3 Polarization redistribution spectrum for the red wing of Hg($^3P_1$—$^1S_0$)–Kr: Comparison with theory. 144
6.4 Improved theoretical curves for the polarization redistribution spectrum of Sr–Ar. 147

List of Tables.

Chapter 3. Page

3.1 Summary of potentials proposed by Fuke *et al.* 1984. 74
3.2 Summary of potentials to be used in chapter 6. 83

Chapter 5.

5.1 Hyperfine structure of the Hg 2537Å line. 117
5.2 Blue wing polarization data. 131

Chapter 6.

6.1 Values of σ_R and $\sigma^{(2)}$ for Hg($^3P_1$—$^1S_0$)–Kr. 139

For Helen

Chapter 1.

Introduction.

1.1 Historical Background.

Atomic spectroscopy has a long and distinguished history, having been central to the development and refinement of quantum mechanics. The study of atomic and molecular spectra has continued as a subject of great interest in its own right. This results from the insights it affords into atomic and molecular structure and dynamics. Much of the information available about molecular interactions in particular, can be summarized in the form of an interaction potential surface. The study of molecular spectra is one of the most powerful tools in the elucidation of these potentials.

With the benefit of hindsight it may seem obvious that the positions and intensities of spectral lines carry much important information. It is less obvious that the widths and shapes of these lines are just as rich in information, yet the field of spectral line shapes dates back to Michelson in the late 19th century. As our experimental abilities have progressed, finer and finer details of the interactions have become susceptible to investigation. The recent availability of tunable dye lasers has revitalized the field and has made extremely delicate experiments possible.

Using an instrument of arbitrarily large resolving power, spectral lines emitted by an isolated, stationary atomic system appear to have a 'natural' width associated, through the energy–time uncertainty relation, with the lifetime of the excited state. When an atom is not isolated but is perturbed by interactions with its environment the spectral lines are broadened and can even change shape. For a metallic vapour, the environment consists of the other atoms in the gas and since collisions with these other atoms become more frequent as the pressure is increased this broadening mechanism is known as collision or pressure broadening. Figure 1.1 illustrates the way in which collisions perturb a radiating atom. The frequency of the emitted light is perturbed during the collision resulting in a phase shift between the wave train being emitted before

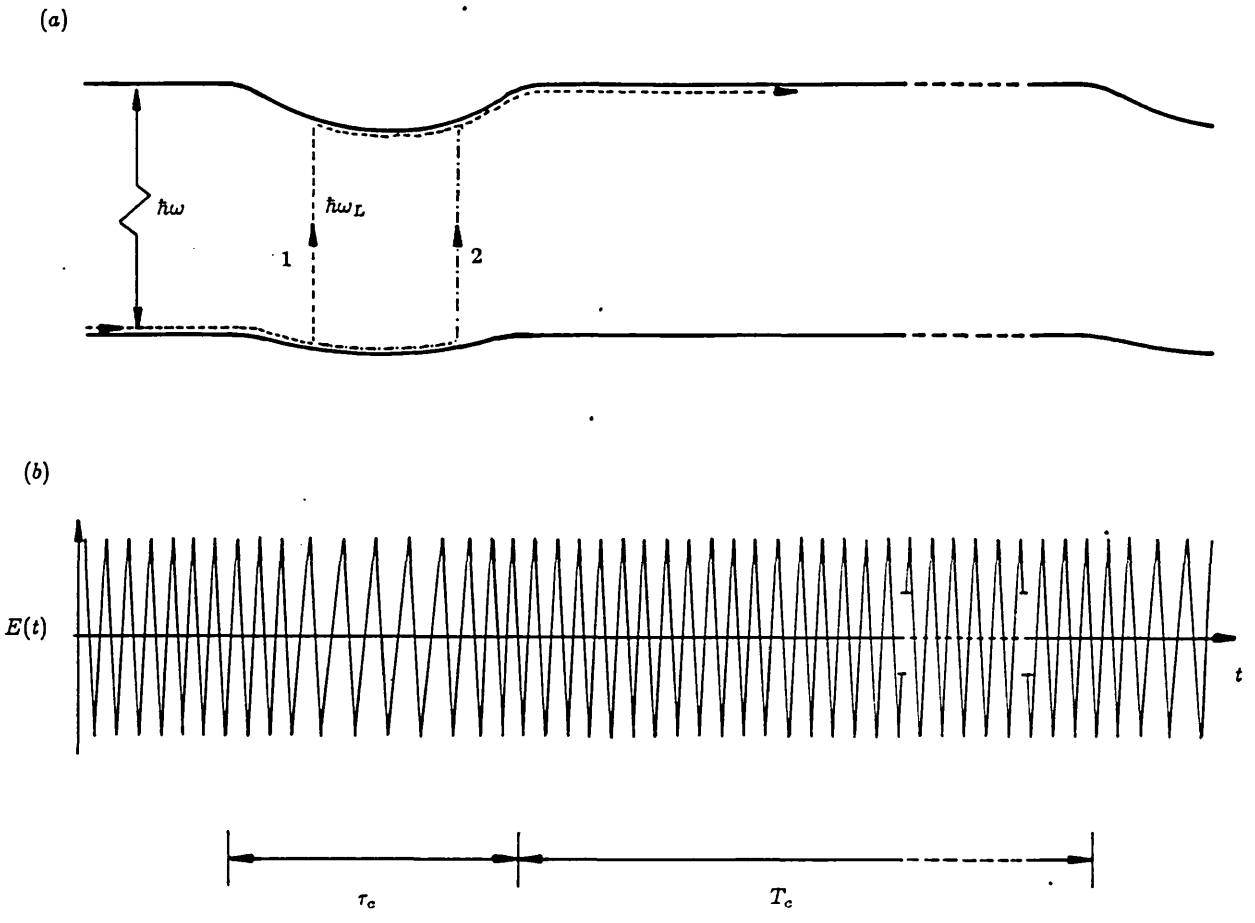


Figure 1.1 Collision perturbing energy levels. (a) For attractive ground and excited state potentials, energy levels are suppressed during a collision. (b) The phase of the emitted wave train is different before and after the collision as a result of the change in frequency during the collision. The period of oscillation is drawn unrealistically large. Note the time between collisions T_c is greater than the collisional duration τ_c. When excitation occurs *during* a collision by absorption of a photon $\hbar\omega_L$, the interaction may proceed along either route 1 or 2. Interference between the two routes leads to oscillations in the lineshape $I(\omega)$ for a given trajectory. Such oscillations are often averaged out when many trajectories are included.

and after the encounter. Despite the seeming simplicity of these ideas a comprehensive theory for the lineshape, valid at all detunings from the resonant frequency ω_0 is very difficult to provide.

It is usual to find the problem discussed in two distinct regimes: the impact and quasistatic approximations. Essentially the impact approximation deals with light that is radiated between collisions. A spread in frequency results when the stochastically interrupted wave train is Fourier analysed. The quasistatic approximation essentially deals with radiation emitted *during* the collision at frequencies other than ω_0. While the impact lineshape therefore furnishes us with information on the collision, through the total phase shift accrued, the quasistatic lineshape depends in a more detailed way on the dynamics of the collision.

The basic ideas of collisional redistribution are illustrated in figure 1.2. An optically active atom in its ground state is situated in a bath of structureless perturbers with which it undergoes collisions. A laser of frequency ω_L and polarization ϵ_L is shone onto the atom and the light scattered in a particular direction is collected and analysed in terms of its frequency and polarization. The scattered spectrum consists of an elastic Rayleigh peak centred at ω_L and an inelastic fluorescence peak centred at the resonant frequency ω_0. The energy difference $\hbar\omega_L - \hbar\omega_0$ is made up by a loss or gain of kinetic energy in the collision and the photon is said to have been "redistributed" in frequency. The polarization of the Rayleigh peak is identical to the polarization of the input radiation, though the polarization of the fluorescence may have been altered.

If we consider the collision to adiabatically deform the energy levels of the active atom as the interaction progresses then absorption of the photon can be taken to occur at a specific point in the collision. The active atom spends roughly half the collision in the ground state and the other half in the excited state. The field of collisional redistribution can therefore be regarded as an example of so called half–collisions.

By varying the laser frequency ω_L it is possible to cause excitation at different points in the collision. By studying the redistributed spectrum we can obtain direct information on the interatomic potential. This is a remarkable achievement since we are studying processes that occur on a timescale set by the

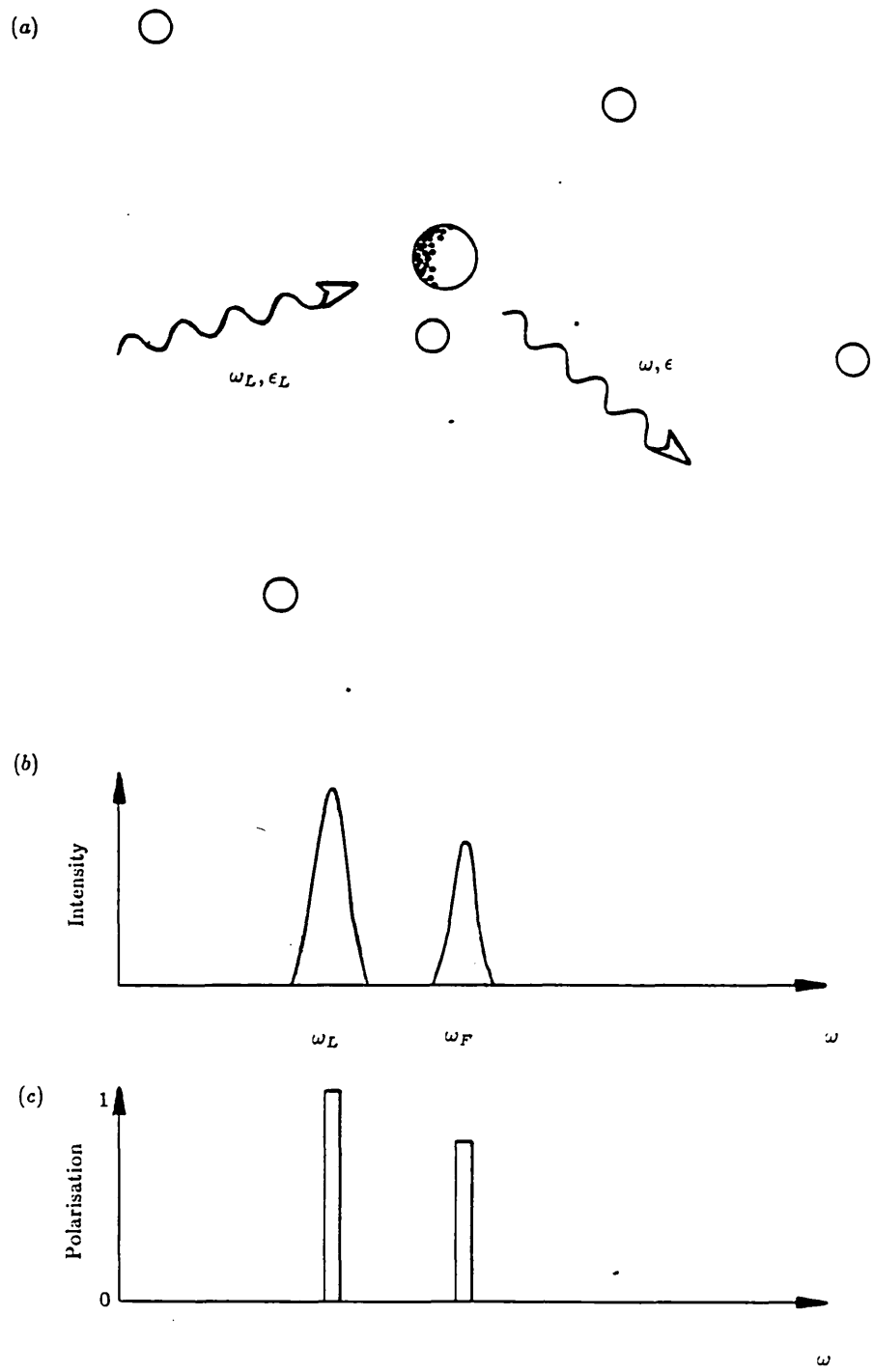


Figure 1.2 Schematic redistribution experiment. (a) Light of frequency ω_L and polarisation ϵ_L is scattered off an atom undergoing collisions with perturbers in a thermal cell. (b) Frequency response $I(\omega)$ consisting of an elastic Rayleigh peak at ω_L and an inelastic redistributed fluorescence peak at ω_0 (c) Polarisation redistribution spectrum of scattered light assuming a $J = 0 \rightarrow J = 1$ transition.

collisional duration. These durations are typically very short indeed ($\sim 1ps$), yet the tunability of the laser radiation allows us to effectively plot the time evolution of the collision complex whilst the laser fluence achievable makes the signal level tolerable.

The theory needed to account for collisional redistribution has evolved to meet the demands of ever more extreme experimental tests. Huber (1969) and Mollow (1970) developed an early form of redistribution theory applicable to a two level atom undergoing collisions within the impact approximation. Omont, Smith and Cooper (1973) extended this work by including the possibility of m_J degeneracy. Ballagh and Cooper (1977) went further by working out several specific cases relevant to given experimental geometries. Nienhuis and Schuller (1977) and Voslamber and Yelnik (1978,1979) put forward theories valid in limited parts of the wing. Cooper (1979) proposed a theory applicable to the quasistatic wing and Burnett *et al.* (1980a,1980b,1980c) synthesized the preceding theories into a unified theory valid at all detunings. Nienhuis (1983) published a theory which uses a different formalism to that of Burnett *et al.* but which reaches the same conclusions. Due to the analytical complexity of the above theories a semiclassical theory, based on a physically simple molecular model for the collisions, has been described by Lewis *et al.* (1983). This model can be applied whenever the interaction can be assumed to proceed adiabatically along well characterized and well separated interatomic potentials. The theory of Burnett and Cooper is far more general being restricted only by the binary collision approximation (see §2.2.1).

This model assumes excitation to occur in the middle of a collision, to a state of definite angular momentum with respect to a molecular axis pointing along a line joining the two nuclei. The colliding atoms are taken to follow classical straight line trajectories and the effect of the collision is to geometrically rotate the angular momentum states. At some time after the collision the atom radiates from these reoriented states. The reorientation experienced during the collision manifests itself as depolarization of the fluorescence.

The first collisional redistribution experiments were performed by Carlsten *et al.* (1977) on Strontium perturbed by Argon. Corney and McGinley (1981) have performed similar experiments on Calcium perturbed by Argon. These

experiments studied the redistribution line shape only. Studying Strontium perturbed by argon, Thomann *et al.* (1980) performed the first collisional redistribution experiments in which the polarization of the fluorescence was monitored and thus gained information not available through line shape analysis alone. Kroop and Behmenburg (1980) performed similar experiments for the Sodium–Argon system. It should be noted that experiments in the Na($^2P_{3/2}$—$^2S_{1/2}$)–Ar system suffer from complications that arise due to spin–orbit coupling. The presence of fine structure makes the interpretation of the depolarization data much more difficult.

Since the experiments of Thomann *et al.* covered a limited range of detunings in the red wing Alford *et al.* (1983) performed systematic experiments in the same system, for much larger detunings in both the red and blue wings. They also performed experiments in Barium–Rare Gas systems (Alford *et al.* 1984) in which the collisional redistribution lineshape and polarization were measured. Behmenburg, Kroop and Rebentrost (1985) conducted experiments in which the input light was circularly polarised and the fluorescence was analysed for circular polarization.

Collisional redistribution is closely related to other areas of study, such as photodissociation and half-reactions, that fall into the category of half-collisions. In photodissociation a bound ground state molecule is excited into a dissociative upper state. The polarization of the fluorescence from the fragments thus produced has been observed (de Vries 1982) and analysed in a fashion similar to the analysis of collisional redistribution experiments (Vigue *et al.* 1981, Greene & Zare 1982). In a half reaction experiment absorption of a photon in the middle of a reaction produces product distributions different from those obtained in the absence of the laser field.

These related subjects have been discussed by Foth *et al.* (1982) and by Telle (1984). Workers in a particular area of half collision studies can greatly benefit from the insights gained in the other areas. This has been recognized by the community and a spirit of co-operation has emerged in recent years.

1.2 Motivation For The Present Work. Hg($^3P_1$—$^1S_0$)–Kr as a Prototype System.

When a new type of spectroscopy emerges the first case to which it is applied is often the $^1P_1 - ^1S_0$, $J = 0 \rightarrow 1$ resonance transition. For this case experiments benefit from the large oscillator strength and the theoretical interpretation benefits from the relative simplicity of the analysis. As the theory becomes established more complicated cases can be studied. It is therefore somewhat surprising that the Hg 2537 Å $^3P_1 - ^1S_0$ transition has often been employed as a prototype.

Lord Rayleigh (1922) discovered the magnetic depolarization of resonance fluorescence using this transition. Hanle (1924) performed further experiments on this effect which now bears his name. The first magnetic double resonance and optical pumping experiments were carried out on this transition by Brossel, Bitter and Kastler (see eg. Brossel & Bitter (1952)). The reasons for its frequent use are largely to do with its experimental convenience. The large degree of Spin–Orbit interaction ensures that the oscillator strength is within a factor of fifty of the strongest true resonance lines whilst the fact that Hg is the only metal which is a liquid at room temperature makes it easy to study in the vapour phase. The true resonance line at 1840Å is experimentally inconvenient as it lies in the vacuum ultra violet (see figure 1.3). Naturally occurring Hg is a mixture of even and odd isotopes leading to a complicated hyperfine structure. This added complication has often been avoided by the use of pure even isotopes.

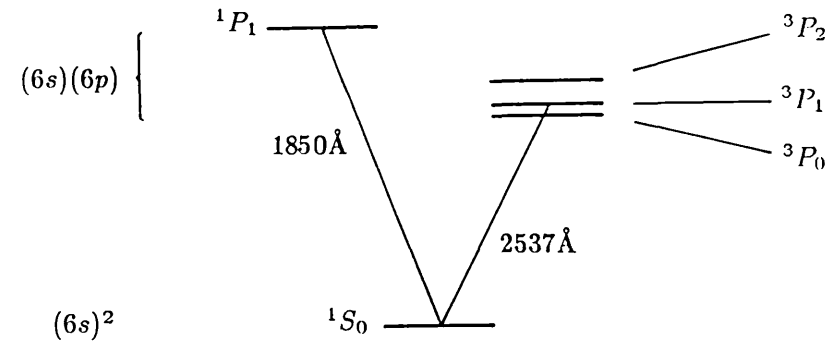


Figure 1.3 The Lowest Energy Levels of Hg.

After a discussion of what has been achieved using collisional redistribution up to and including the work of Alford *et al.* (1984), Burnett (1985) addresses the subject of future work writing : "...The next step is obvious : we must have a quantitative test of redistribution theories for cases where the quasi-line shapes, both temperature and frequency dependence can be analysed fully. This will afford a test bed for the extra quantitative information redistribution can provide." The ability to perform such a full analysis depends on our knowing the interatomic potentials as input data for the theory under test.

The interatomic potentials for Hg($^3P_1$—$^1S_0$)–RG systems have been the subject of many experimental investigations (see Chapter 3 for references). Such studies were accelerated in the early 1980's as a result of the proposal that these systems were possible candidates for a high power excimer laser.

In deciding to study the Hg($^3P_1 - ^1S_0$)–RG systems we have made the same choice as others in that we sacrifice some of the simplicity associated with a $^1P_1 - ^1S_0$ transition in favour of experimental expediency. To a large extent the choice has been made for us by our dependence on other authors to furnish the interatomic potentials.

1.3 Thesis Outline.

Chapter 2 is a discussion of the theory necessary for an understanding of the results and analysis presented later in the thesis. The chapter is split up into two distinct topics; spectral line broadening and collisional redistribution. In the treatment of both of these subjects physical pictures are emphasized. The line broadening discussion sets out the major approximations made and discusses the regions of their validity. Since much of the analysis to follow proceeds under the assumption of a molecular model for the collision complex the line shape discussion concludes with a description of a molecular approach to the problem. In the section on collisional redistribution the derivation of a general expression for the polarization as a function of detuning is given. This derivation is accomplished within the framework of a molecular model.

Throughout chapter 2 the subject of interatomic potentials recurs and since this subject is at the heart of the motivation for the present work a discussion

of this topic is presented in chapter 3. Chapter 3 is also split up into two major sections. The first is a general discussion of methods for elucidating interatomic potentials from various types of experimental data. At this point there is a strong link to the discussion in chapter 2 of temperature dependent line shape studies. The second section rests on the first and discusses experiments by other authors specific to the Hg $(^3P_1 - ^1S_0)$–Kr case. The chapter ends with an assessment of the available interatomic potentials and an affirmation of the potentials which are taken to be the best choice in the region of interest to the present work.

Chapter 4 turns to the experimental apparatus and method and includes a discussion of the experimental signal level. Under ideal conditions one would perform these experiments in such a way that the measured polarization depends only on the amount of reorientation experienced by the optically active atom during the collision. The experimental signal was however found to be too low under such conditions. Consequently the experiments have been performed in a regime in which other depolarizing processes were in play. The polarizations thus measured were lower than those predicted by the reorientation model, however since these other processes were either well understood or experimentally determinable, they could be allowed for and the results corrected accordingly. The theoretical background to these other effects and the means for correcting the data are the subjects of chapter 5. We conclude chapter 5 by presenting our corrected results.

In chapter 6 these results are analysed. Since our analysis follows closely the analysis by Lewis *et al.* of similar experimental results to ours (but for the case of $Sr(^1P_1 - ^1S_0)$–Ar collisions), their work is outlined at the beginning of the chapter. In this chapter we point out the differences that occur in the case of a $^3P_1 - ^1S_0$ transition.

Chapter 7 presents our conclusions and makes suggestions for means of extending and improving the present work. This chapter also includes a discussion of further work in the field, indirectly related to ours.

Chapter 2

Theory.

2.1 Introduction.

This chapter addresses itself to those aspects of atomic theory that will prove important in understanding the experiments performed and in the analysis of the results obtained. It is split up into two major sections; the first (§2.2) dealing with the theory of spectral line broadening via non resonant collisions with neutrals and the second (§2.3) with the theory of collisional redistribution.

2.2 Theory of Line Broadening by Nonresonant Collisions with Neutrals.

Allard and Kielkopf (1982) have provided a comprehensive review of this field. The reader is referred to this article for a more complete discussion and for an extensive bibliography.

2.2.1 Fourier Transforms, Timescales and Interatomic Forces.

We consider a simplified atom with two energy levels E_g and E_e between which a radiative transition takes place. To a first approximation we would expect radiation at a single frequency ω_0 where

$$\omega_0 = (E_e - E_g)/\hbar \tag{2.1}$$

Classically the electric field would be described by

$$E(t) = E_0 exp\{-i\omega_0 t\} \tag{2.2}$$

The power spectrum $I(\omega)$ is proportional to the square of the Fourier transform of E(t).

$$I(\omega) \propto \left[\left(\frac{1}{2\pi}\right)^{1/2} \int_{-\infty}^{\infty} E(t) e^{i\omega t} dt\right]^2 \tag{2.3}$$

This function is sharply peaked at $\omega = \omega_0$ for an infinite wavetrain, corresponding to monochromatic emission. Of course the idea of an infinite wavetrain is unphysical since the atom will radiate away its energy, and will eventually be found in its ground state. The finite lifetime of atomic states necessitates the inclusion of a damping term (Corney 1977) in *eq*.2.2 giving

$$E(t) = E_0 exp\{-i(\omega_0 + i\frac{\gamma}{2})t\} \tag{2.4}$$

which, when substituted into *eq*.2.3 gives

$$I(\omega) = I_0 \frac{(\gamma/2\pi)}{(\omega - \omega_0)^2 + \gamma^2/4} \tag{2.5}$$

This is known as a Lorentzian lineshape. It has a full width at half maximum (FWHM) equal to γ. The above derivation is classical and the damping constant has been introduced phenomenologically, however a quantum mechanical calculation (Weisskopf & Wigner 1930) gives exactly the same result. The broadening mechanism discussed here is called natural or radiative broadening. Under most conditions and certainly under the conditions in the experiments to be described in this thesis, natural broadening is negligible in comparison to broadening as a result of collisions between the radiating atom and perturbers.

One way of approaching the problem of so-called pressure or collision broadening, within a classical framework is to assume that the frequency of the oscillating dipole in *eq*.2.4 is perturbed during a collision. Lenz (1924) and Weisskopf (1932) suggested that the effect of the collision is to change the phase of the dipole through

$$E(t) = E_0 e^{-i\omega_0 t} e^{-i\eta(t)} \tag{2.6}$$

Where natural broadening has been neglected and $\eta(t)$ is the total phase change at time t due to the collision or collisions and is given by

$$\eta(t) = \int_{-\infty}^{t} \Delta\omega(t) dt \tag{2.7}$$

Substituting *eq*.2.6 into *eq*.2.3 we have

$$I(\omega) \propto \frac{E_0^2}{2\pi} \left[\int_{-\infty}^{\infty} dt e^{i(\Delta\omega t - \eta(t))} \right]^2 \tag{2.8}$$

Equation 2.8 can be regarded as the general equation for the lineshape in a classical phase shift theory of line broadening. There exist quite diverse theories of line broadening that share a common starting point in their use of this formula but diverge by virtue of subsequent approximations made. For now we note that the integral in *eq.*2.8 can only be appreciable when the integrand is non-oscillatory. This occurs when the exponent in equation 2.8 is constant *ie.* when $(d/dt)(\Delta\omega t - \eta(t)) = 0$, giving

$$\omega - \omega_0 = \dot{\eta}(t) \tag{2.9}$$

This is known as the stationary phase condition. It can be satisfied in two ways. A trivial solution exists when $\Delta\omega = 0$ and η is constant in time. This solution describes the atom radiating at the unperturbed frequency, predominately *between* collisions. As we will see the stationary phase condition can also be fulfilled at large detunings, at specific points given by equation 2.17. Evaluation of *eq.*2.8 taking only the contributions near these points of stationary phase describes the atom radiating, predominately *during* a collision, at the perturbed frequency. The difference between these two cases is of fundamental importance and will be returned to in the following sections. At this stage we denote

$$t_i = \frac{1}{\Delta\omega} \tag{2.10}$$

and call t_i the time of interest for producing light at a detuning of $\Delta\omega$. The significance of this timescale will become clear when the timescales describing the collision have been examined. The two timescales of importance are τ_c and T_c, the average collisional duration and the mean time between collisions respectively. The mean free time can be found using

$$\frac{1}{\gamma_c} = T_c = \frac{\lambda}{\overline{v}} = \frac{1}{\overline{v} n_\rho \sigma_R} \tag{2.11}$$

(Corney 1977) where λ is the mean free path, $\overline{v}$ the average relative velocity between atom and perturber and σ_R is the optical collision cross section (see § 2.2.2) and has the value of $227 \times 10^{-16} cm^2$ for Hg perturbed by Kr (Lewis

* $\Delta\omega$ is strictly time dependent however it is slowly varying in comparison with $\eta(t)$. Even when $\Delta\omega$ is constant $\eta(t)$ increases linearly with time.(see eq.2.7)

1980). For the experiments that we have performed T_c is found to be $\sim 28ns$. The collisional duration can be calculated using

$$\tau_c = \frac{R_W}{\overline{v}} \tag{2.12}$$

where R_W is estimated from

$$\sigma_R \approx \pi R_W^2 \tag{2.13}$$

The subscript W will become clear in § 2.2.2.* In this way τ_c is found to be $\approx 2.6ps$ for Hg-Kr collisions. It is apparent that $T_c \gg \tau_c$ and therefore to a good approximation only collisions between an atom and a single perturber need be considered. This is called the binary collision approximation (BCA). For the Hg-Kr system, the BCA will break down when $T_c \approx \tau_c$ which, using *eqs*.2.11–2.13 is found to occur at a number density given by

$$n_p = \frac{\sqrt{\pi}}{\sigma_R^{\frac{3}{2}}} \tag{2.14}$$

which has the value of $5 \times 10^{20} cm^{-3}$ corresponding to a pressure of ~ 61 atmospheres.

The calculation of collisionally broadened lineshapes is a highly complex subject with a rich literature. The complexities are greatly reduced by treating the problem in one of two limiting regimes known as the impact limit and the quasistatic limit. The impact limit is defined by

$$t_i \gg \tau_c \tag{2.15.a}$$

while the quasistatic limit is defined as the opposite extreme

$$t_i \ll \tau_c \tag{2.15.b}$$

There exist so-called "unified theories" (*eg.*Anderson & Talman 1956, Vidal *et al.* 1969, Voslamber 1969, Szudy & Baylis 1975,1977) that describe the entire line profile however these theories do not lend themselves to simple intuitive interpretation. Such theories reduce to the results of the impact and quasistatic approximate theories in the appropriate limits. In the impact limit the time of interest for producing light at a detuning of $\Delta\omega$ is long compared to the collision

* W stands for Weisskopf. $R_W \equiv \rho_W$ is the Weisskopf radius of §2.2.2.

time. This means that only the integrated effect of a collision can be felt and that most of the radiation actually occurs between strong collisions. In the quasistatic limit the radiation is emitted on a timescale short compared to the collisional duration, at a well defined interatomic separation and at a perturbed frequency.

Study of the quasistatic lineshape therefore yields detailed information about the perturbing potential. This force can be described by assigning an interatomic potential surface upon which the atoms move during the collision. Any function of r that approaches zero for large r can be approximated by an expansion in powers of $1/r$. A single term will often suffice giving

$$\Delta V_k = \frac{C_n}{r^n} \quad \text{with } k = e, g \tag{2.16}$$

where ΔV_k is the change in energy of the k level of the transition. The change in frequency of the transition is given by

$$\Delta\omega = \frac{\{\Delta V_e(r) - \Delta V_g(r)\}}{\hbar} \tag{2.17}$$

$$= \frac{(C_n^e - C_n^g)}{\hbar r^n} \tag{2.17b}$$

In the case of Hg perturbed by Kr the interaction is largely of the dipole-induced dipole or van der Waals type with $n = 6$. *Eq.*2.17 is only approximately correct for the interaction between Hg and Kr. The actual form of the interaction will be discussed in Chapter 3.

A third type of broadening mechanism exists called Doppler broadening. It results from the apparent shift in the wavelength of the signal coming from a source moving towards or away from the observer. The atomic motion is random with a Maxwellian distribution of velocities. The resulting line shape is Gaussian (Thorne 1977), with a width of $\delta\nu_D$ given by

$$\frac{\delta\overline{\nu}_D}{\overline{\nu}_0} = 7.16 \times 10^{-7}\sqrt{\left(\frac{T}{M}\right)} \tag{2.18}$$

where M is the mass number. For the Hg 2537 Å line, and at room temperature $\delta\overline{\nu}_D \approx .03cm^{-1}$. As will be shown in the next section the impact region pressure

broadened lineshape is Lorentzian with a halfwidth comparable to the Doppler width. A correct description of the impact regime lineshape would therefore involve a convolution of the Doppler and pressure broadened shapes known as a Voigt profile. It will be noted however that although the halfwidths are comparable for the two processes the Lorentzian shape is dominant in the wings. Doppler broadening and pressure broadening are not strictly independent and correlations between the two processes do exist. These correlations do not affect the considerations given here.

2.2.2 Impact Limit

Lorentz was responsible for one of the earliest pressure broadening theories. He assumed that an atom would radiate at its resonant frequency ω_0 until quenched by a hard collision. E(t) then consisted of periods of radiation at ω_0 of differing lengths T_c, coming from *different* atoms in an ensemble. T_c was taken to follow a Poisson distribution and the Fourier transform of E(t) yielded the Lorentzian lineshape

$$I(\omega) = I_0 \frac{(1/T_c)}{(\omega_0 - \omega)^2 + (1/T_c)^2} \tag{2.19}$$

where T_c is the mean time between collisions. The model gave good qualitative agreement with experiment in that the shape was correct however it was unable to predict the correct width if T_c was calculated using *eq*.2.11 and using known gas kinetic cross sections for σ_R . The experimental widths suggested cross sections between one and two orders of magnitude greater than the gas kinetic cross sections. The theory was also unable to account for the shift in the position of the centre of the line that often accompanies pressure broadening.

Weisskopf was able to solve the first anomaly by clarifying what was meant by a collision. He realized that it was unnecessary for the collision to quench the atom and that the stochastically varying E(t) of the Lorentz theory (see fig 2.1) could be created in a *single* atom by collisions that interrupt the phase of the dipole. His starting point was *eq*.2.7 and took r of *eq*.2.17 to be

$$r = (\rho^2 + \overline{v}^2 t^2)^{\frac{1}{2}} \tag{2.20}$$

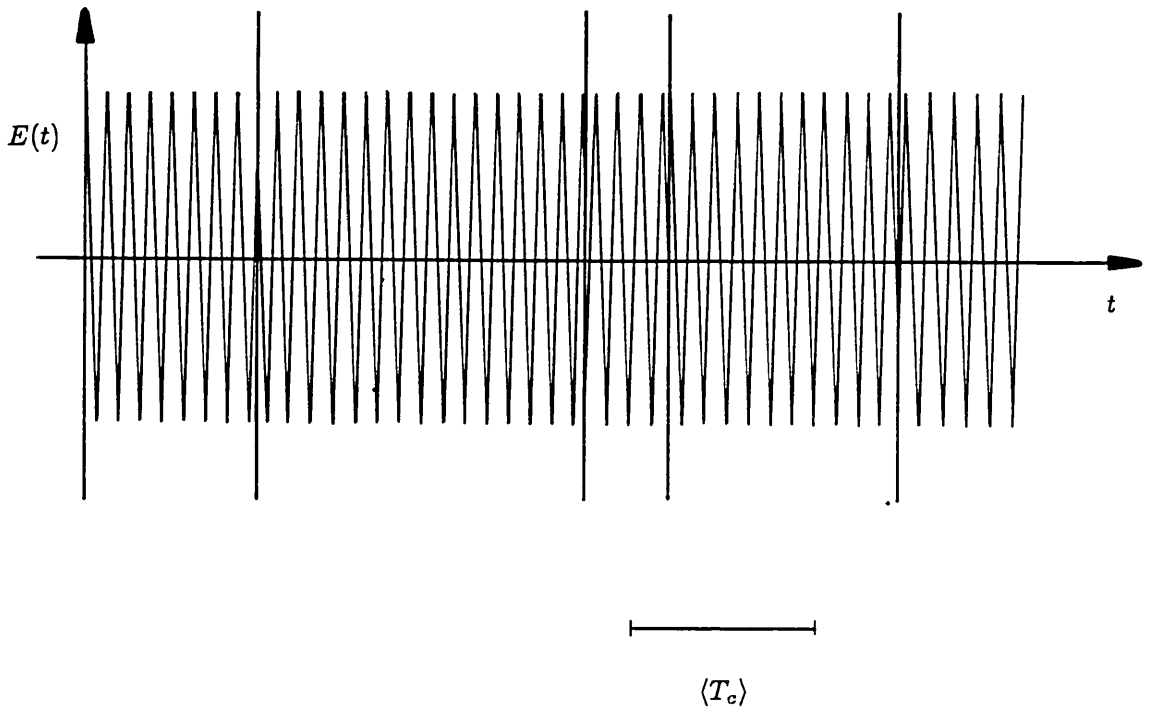


Figure 2.1 Phase interruptions in the Impact Approximation. Collisions, represented by the vertical bars, stochasitically interrupt the phase of the wave train. The period of oscillation is greatly exaggerated for clarity. The average time between collisions $\langle T_c \rangle$ is shown.

where ρ = impact parameter. With this value of r he obtained

$$\eta(\rho) = \frac{3\pi C_6'}{8\overline{v}\rho^5} \tag{2.21}$$

with $C_6' = C_6^e - C_6^g$ and $n = 6$ for a van der Waals interaction. Weisskopf assumed arbitrarily that a phase shift of greater than unity caused the wave train being emitted after the collision to be completely incoherent with the one being emitted before the collision. With $\eta(\rho) = 1$ we have

$$\rho_W = \left(\frac{3\pi C_6'}{8\overline{v}}\right)^{1/5} \tag{2.22}$$

where ρ_W is the Weisskopf radius. The resulting lineshape is Lorentzian with a halfwidth at half maximum given by

$$\gamma_c = N\pi \left(\frac{3\pi C_6'}{8\overline{v}}\right)^{2/5} \overline{v} \tag{2.23}$$

The Weisskopf theory gives approximate quantitative agreement with experimental results and is noteworthy for its establishment of the link between the interatomic potential and the lineshape through *eq.*2.23. The choice of $\eta(\rho) = 1$ as the criterion for the occurrence of a collision was however arbitrary. Furthermore the theory did not predict a shift.

Physically the shift is due to weak, distant collisions which are occurring all the time. For an attractive potential the frequency is always lowered by such collisions and the phase shift per collision is less than unity. The result is that the emitted light is shifted to the red. A theory that included these small phase shifts and correctly predicted a shifted line was first developed by Lindholm (1945) and Foley (1946). Lindholm introduced a complex damping constant which resulted in an "optical"collision cross section with a real part

$$\sigma_R = 2\pi \int_0^\infty \{1 - \cos\eta(\rho)\}\rho\, d\rho \tag{2.24}$$

and an imaginary part

$$\sigma_I = 2\pi \int_0^\infty \rho \sin\eta(\rho)\, d\rho \tag{2.25}$$

The result was a shifted Lorentzian given by

$$I(\omega) = \frac{I_0}{\pi} \frac{N\sigma_R\bar{v}}{(\omega - \omega_0 + N\sigma_I\bar{v})^2 + (N\sigma_R\bar{v})^2} \tag{2.26}$$

The integrands of equations 2.24 and 2.25 depend on ΔV through the $\eta(\rho)$ term. Most of the contribution to σ_R comes from the region $\rho < \rho_W$ whilst most of the contribution to σ_I comes from the region where $\rho > \rho_W$ (see Corney 1977). This agrees with the previous arguments in that the shift is caused predominately by weak distant collisions whilst the width is due to hard, dephasing collisions. The above theory is known as adiabatic impact theory. It gives good agreement with experiment provided none of the inherent assumptions are violated and subject to the condition that the interatomic potential is well known.

This classical discussion of line–broadening in the impact limit serves to point out the essential features of this regime. The most important thing to note is that it is the *integrated* effect of hard collisions that dominates the lineshape. A limited amount of information about the interatomic potential can be extracted from impact lineshape data if a simple analytical form can be assigned to the potential *a priori*.

Thus far in the discussion we have made the classical path approximation in which the perturbers are taken to follow classical straight line trajectories. The approximation is valid so long as the de Broglie wavelengths of the colliding particles are less than the average distance of closest approach during a collision. This approximation is valid for the case of Hg perturbed by Kr (see § 6.5.2) but may break down for collisions involving light particles such as the electron-ion collisions found in a Hydrogen plasma. Fully quantum mechanical theories exist (Cooper 1967) which do not make the classical path approximation and extend the validity of the impact approximation to cover such systems. The quantum mechanical theories reduce to their classical analogue for the systems studied here.

2.2.3 Quasistatic Limit

The quasistatic limit is characterized by $t_i \ll \tau_c$ which means that details of the collision are important in determining the lineshape. As we shall see, study

of the quasistatic lineshape can yield much information about the interatomic potentials involved. A derivation of the line profile in this regime can be approached in a number of ways. Holtsmark (1919) was the first proponent of the theory. He assumed that the collisional duration was so long that the perturbers could be regarded as being stationary (hence the name quasistatic). The BCA is once again made and the interaction energy ΔE between a given atom/perturber pair is regarded as causing a shift $\Delta\omega = \Delta E/\hbar$ in the radiated frequency. The second step is to perform a statistical average over all atom/perturber pairs yielding the line profile for the assembly of atoms.

Kuhn (1934) performed the statistical average by taking a single perturber for each emitting atom situated somewhere at random in a sphere of radius R_s corresponding to an arbitrary cut off for the interaction. The intensity of light shifted by $\Delta\omega(r)$ is given by the probability of finding a perturber at r within a spherical shell of volume $4\pi r^2\,dr$ giving

$$I(\omega)\,d\omega \propto 4\pi r^2\,dr \tag{2.27}$$

This is the basic Quasistatic result. Substituting for r from eq.2.17b and using the expression for C_6' given in the previous section we have

$$I(\omega) \propto \frac{C_6'}{(\Delta\omega)^{\frac{3}{2}}} \tag{2.28}$$

for the van der Waals interaction. The quasistatic result can alternatively be derived using the general classical equation for the lineshape, *eq*.2.8 putting

$$\Delta\omega(t) = \frac{\Delta V(R(t))}{\hbar} = \left[V_e(R(t)) - V_g(R(t))\right]/\hbar \tag{2.29}$$

The exponential integrand in the equation is a rapidly oscillating function for most regions of t. It is therefore appropriate to evaluate the integral using the method of stationary phase which gives

$$I(\omega) \propto \left| \sum_j \left(\frac{2\pi}{|\Delta\dot{V}(R(t_j))|} \right)^{\frac{1}{2}} exp\left[i\Delta\omega t_j - \frac{i}{\hbar}\int_{-\infty}^{t_j} \Delta V(R(t))\,dt \right] e^{\pm i(\pi/4)} \right|^2 \tag{2.30}$$

with the stationary phase points specified by

$$\Delta\omega = \Delta V(R(t_j)) \tag{2.31}$$

Here $\Delta\dot{V}(R(t_j))$ is the time derivative ofΔV evaluated at the stationary phase point $R(t_j)$. The sign of the final exponential in *eq*.2.30 is given by

$$+ \rightarrow \Delta\dot{V}(R(t_j)) < 0$$

$$- \rightarrow \Delta\dot{V}(R(t_j)) > 0 \tag{2.32}$$

In a situation where there is more than one stationary phase point evaluation of the square in *eq*.2.30 gives rise to interference terms. Such interference terms can lead to undulations in the line profile known as supernumary oscillations however when the stationary phase points are well separated the interference terms average to zero on performing the average over collisions. If the stationary phase points are not well separated the method of stationary phase is inapplicable and *eq*.2.30 is not valid. Evaluation of 2.30 with the cross terms neglected can be shown to yield the quasistatic result (Alford 1984).

The physical basis of the quasistatic theory is the Franck-Condon principle (FCP). The FCP can be expressed both classically and quantum mechanically. Classically it says that molecular electronic transitions occur at definite internuclear separations where the jump can be made without affecting the kinetic energy of the nuclei. The probability of making a jump is calculated using the method of stationary phase described above. Quantum mechanically the jump occurs with a probability proportional to the overlap integral between the wave functions in the ground and excited states. The point at which the jump takes place is termed the Condon point. The quasistatic approach consists of considering the atom/perturber pair as a quasi-molecule and using the Franck-Condon principle (FCP) to decide where a transition will take place.

We can now rewrite *eq*.2.17 as

$$\hbar\Delta\omega = \Delta V(R_c) = V_e(R_c) - V_g(R_c) \tag{2.33}$$

with the $\Delta V(\infty) = 0$ convention adopted and where R_c is the Condon point.

2.2.4 A Molecular Approach to the Quasistatic Lineshape.

It is by now apparent that study of the quasistatic line profile can yield detailed information about the interatomic potentials and will be of the greatest interest here. Since the molecular approach gives such good intuitive pictures of the phenomena and since it forms the basis of the molecular reorientation model used to interpret the data it will be useful to look at this approach in greater detail. Jablonski (1931) was the first to use quantum mechanics to work out the spectrum of light emitted during the collisions, treating the atomic collision complex as a quasi-molecule. The following discussion of his contribution follows the review of Allard and Kielkopf.

The initial kinetic energy of the perturber is E_i. It collides with an active atom with energy $\underset{\wedge\hbar}{\omega_0}$ in its excited state. As a result of the collision the perturber either gives up to, or receives from the active atom, some of its kinetic energy. The perturber leaves the collision with a kinetic energy E_f and the active atom emits a photon with energy $\hbar\omega$. By conservation of energy we find

$$\Delta\omega = \xi/\hbar \tag{2.34}$$

where $\xi = (E_i - E_f)$. $I(\omega)$ is then determined by the probability distribution, $W(\xi)$, for the collision to impart/absorb the required energy to/from the perturber. The distribution $W(\xi)$ is calculated within the framework of the Born-Oppenheimer (BO) approximation (see Bransden & Joachain 1983). The BO approximation assumes that the electrons, which move much faster than the nuclei, have time to adjust their wavefunctions adiabatically to accommodate the slight changes of the potential in which they find themselves. The potential is a function of the internuclear separation and the electrons act, not as point charges but as a charge cloud which deforms adiabatically. The ability of the wavefunctions to deform means that transitions between states are not induced by the collision. The approximation breaks down when possible BO states lie close together in energy in which case the states become mixed.

The adiabatic phase shift theories of Lindholm and Foley tacitly assume the Born Oppenheimer approximation to be valid in their neglect of quenching

collisions. The BO approximation allows the total wave function of the quasi-molecule to be written in product form

$$|\psi\rangle = |\phi\rangle|\chi\rangle \tag{2.35}$$

where $|\phi\rangle$ is the electronic wavefunction of the radiator and $|\chi\rangle$ describes the *motion* of the perturber. The electric dipole transition probability of the system is proportional to the square of the matrix element

$$D_{if} = \langle\psi_i|d|\psi_f\rangle \tag{2.36}$$

where d is the electric dipole moment operator and acts only on the electronic wavefunctions. This gives

$$D_{if} = d_{if} A_{if} \tag{2.37a}$$

$$d_{if} = \langle\phi_i|d|\phi_f\rangle \equiv \text{dipole transition moment} \tag{2.37a}$$

$$A_{if}^2 = \langle\chi_i|\chi_f\rangle^2 \equiv \text{Franck} - \text{Condon factor} \tag{2.37b}$$

If d_{if} remains fixed during the collision (Allard & Kielkopf 1982) then the probability that the energy of the perturber will change by ξ is just A_{if}^2. Thus the Franck-Condon factor determines the spectrum.

The perturber states are denoted by quantum numbers v and l where v is the number of nodes in the radial eigenfunction and l is the angular momentum or rotational quantum number. The differential contribution to the lineshape $I(\omega)\,d\omega$ from collisions with incident energy E_i is calculated as

$$I(\omega)\,d\omega = W(\xi)\,d\xi \tag{2.38a}$$

$$= A_{if}^2 \frac{dv_f}{dE_f} Q_l\,dl\,d\xi \tag{2.38b}$$

Here $Q_l\,dl$ is the probability that an incident perturber has an angular momentum between l and dl and dv_f/dE_f is the density of final state energy levels. This expression must be integrated over velocity and impact parameter to yield the final lineshape. The impact parameter integration effectively performs an average over l. The Franck-Condon factors are evaluated using JWKB wavefunctions for $|\chi\rangle$ and employing the method of stationary phase. The resulting

lineshape including the velocity and impact parameter averages can be written in the form

$$I(\omega) \propto \int f(v)dv \int 2\pi b\, db \frac{2v_i(\infty)}{v_i(R_c)} \left|\frac{dR}{d\xi}\right| \tag{2.39}$$

Here $f(v)$ is the Maxwellian velocity distribution given by

$$f(v)\, dv = 2\pi(\pi kT)^{-3/2} exp(\frac{-E_i}{kT}) E_i^{\frac{1}{2}}\, dE_i \tag{2.40}$$

b is the impact parameter, R_c is the Condon point and $v_i(R)$ is the radial velocity of the perturber for the initial state of the system and is given by

$$v_i(R) = v_i(\infty)\left(\frac{E_i - V_i(R)}{E_i} + \frac{b^2}{R^2}\right)^{\frac{1}{2}} \tag{2.41}$$

Carrying out the velocity and impact parameter integrations yields (Hedges *et al.* 1972)

$$I(\omega) = 2\pi(\pi kT)^{-3/2} \times \int_{\epsilon}^{\infty} exp\left(\frac{-E_i}{kT}\right)[E_i - V_i(R_C)]^{\frac{1}{2}} \times 4\pi R_c^2 \left|\frac{dR_c}{d\xi}\right| dE_i \tag{2.42}$$

The lower limit ϵ depends on whether the potential $V_i(R)$ is repulsive or attractive. For a positive, repulsive potential $\epsilon = V(R_c)$ since energies lower than this will not allow R_c to be reached. For an attractive potential the lower limit is given by $\epsilon = 0$. Making the substitution $x = (E - V)/kT$ the integral may be evaluated to yield

$$I(\omega) = \sum_c \left[4\pi R_c^2 \left|\frac{dR_c}{d\xi}\right|^{-1}\right] exp\left[\frac{-V_i(R_c)}{kT}\right] \qquad V_i(R_c) > 0 \tag{2.43a}$$

and

$$I(\omega) = \sum_c \left[4\pi R_c^2 \left|\frac{dR_c}{d\xi}\right|^{-1}\right] exp\left[\frac{-V_i(R_c)}{kT}\right] \times \frac{\sqrt{\pi}}{2} \int_{\frac{-V_i}{kT}}^{\infty} e^{-x} x^{\frac{1}{2}}\, dx \quad V_i(R_c) < 0 \tag{2.43b}$$

Ignoring the exponential term in *eq.*2.43*a* gives the simple quasistatic result due to Khun *eq.*2.27. The Khun formula results from assuming an equal probability of finding a perturber at any R_c. In reality this is not the case and the distribution of perturbers will depend on the ground state potential curve via a

Boltzmann factor which describes the relative ability of the perturber to climb up the potential barrier and get close to the atom.

In the Hg-Kr system the ground state potential is not completely repulsive and therefore $I(\omega)$ should properly be described by *eq.*2.43*b* which allows for bound ground state molecules formed during three body interactions. This point will be elaborated when the potential curves for Hg-Kr are discussed in Chapter 3.

Analysis of the quasistatic lineshape given by *eq.*2.27 allows the difference potential ΔV to be mapped out without assuming any *analytical* form for the potential. The inclusion of the Boltzmann factor means that, through a temperature dependent experiment, the ground state potential V_g can also be deduced. The excited state potential can then be found by straight subtraction of V_g from ΔV. Such temperature dependent lineshape studies have been carried out for a number of cases (*eg.* Hedges *et al.* 1972, Drummond & Gallagher 1974) but are quite difficult to perform. In the case of alkali-rare gas systems it is difficult to cover a large differential temperature range since the lower temperature limit is set by the melting point of the alkali metal whilst the upper limit is set by the extreme difficulties encountered in attempting to contain the highly corrosive alkali vapours at high temperature. Experiments of this sort have been quite successful in generating potential curves in Hg($^3P_1$—$^1S_0$)–RG systems (see Chapter 3 for references) since Mercury, with a high vapour pressure at room temperature, poses less of a problem.

2.2.5 Satellites.

A satellite is a bump in the lineshape often found in the quasistatic wings of pressure broadened lines. The phenomenon is associated with an extremum in the difference potential *ie.* at a position where there are equal (non-zero) forces on the active atom in the two states of interest. At an extremum $d\Delta V/dR = 0$ and the classical expression for $I(\omega)$ experiences a singularity. Whilst this is not actually observed an enhancement of the line profile does occur, leading to a satellite (see figure 2.2). The failure of the classical theory to give an exact profile for the satellite is the result of a breakdown in this region of the

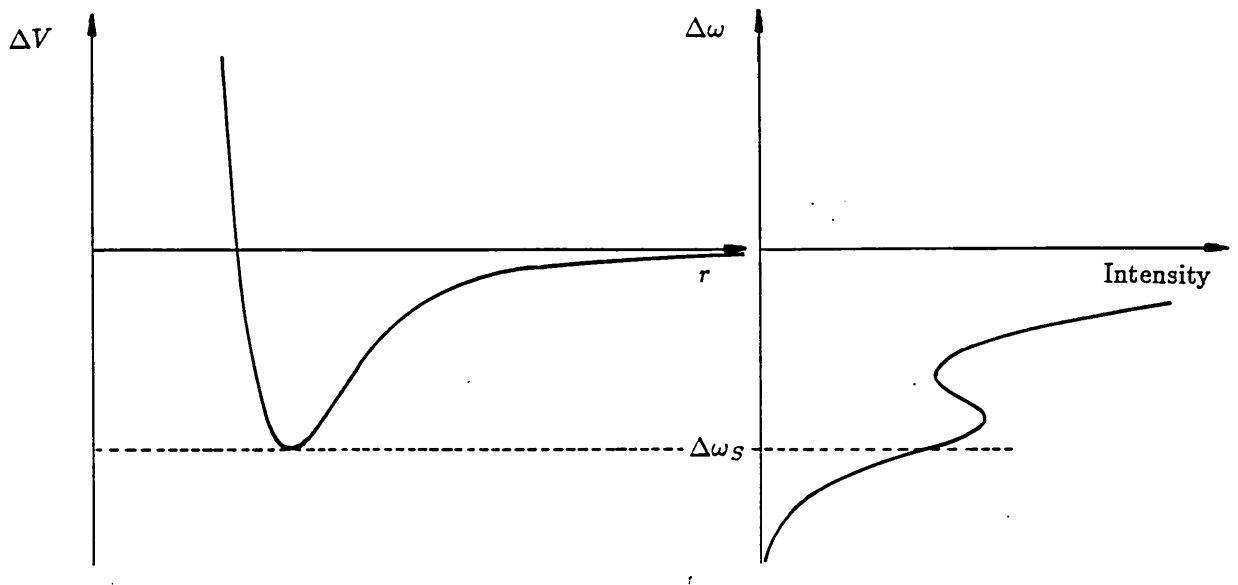


Figure 2.2 Satellite associated with a minimum in the difference potential. At an extremum in the difference potential the colliding pair spend more time emitting at frequencies near $\Delta\omega_S$, resulting in an enhancement of emission at the satellite frequency.

approximations used to obtain the classical quasistatic result. In particular, in the vicinity of a satellite the points of stationary phase used in both the classical theory and the molecular theory lie close together leading to a breakdown of the stationary phase method.

A correct description of the line profile in the region of a satellite is one instance in which a quantum mechanical approach (or semi-classical approach that takes greater care in its application of the method of stationary phase) is essential. Sando and Wormhoudt (1973) developed a semi-classical theory for the shape of satellites based on the Jablonski molecular approach. They point out that the singularity in the classical lineshape, and the zero intensity outside the satellite, are a direct result of the conservation of momentum in the classical Franck-Condon principle. In a quantum mechanical treatment the intrinsic uncertainty in the momentum of the perturber removes the singularity. They compare their semi-classical results with the results of fully quantum mechanical theory and find good agreement.

Sando and Wormhoudt find the depth $\Delta\omega$ of the well in the difference potential to correspond to a detuning at a point beyond the satellite where the intensity is $\sim$ 65% of the peak satellite intensity (see fig 2.2). In the region beyond a satellite there is often no potential to which to excite. Such a region is called antistatic. Sando and Wormhoudt showed the intensity in such a region to decay exponentially with detuning.

2.3 Collisional Redistribution.

2.3.1 Introduction

In section 2.2 we saw how analysis of the lineshape $I(\omega)$ could yield detailed information about the interatomic potentials. The information recoverable in this way was limited to describing the shape of the potential curves. Designation of angular momentum labels for these curves could only be achieved by making certain assumptions about the interactions.

In a typical collisional redistribution experiment an atom is excited *during* a collision by light at the laser frequency ω_L and the fluorescence is detected

from the subsequently free atom at the resonant frequency ω_0. The polarization of the exciting light can be controlled and the polarization of the fluorescence monitored. This constitutes a new ingredient and holds the promise of allowing angular momentum properties of the collision to be investigated. Any theory of collisional redistribution is bound to be more complicated than its complementary lineshape theory by virtue of the necessity to deal with this new ingredient. In particular the collision can cause reorientation of the excited dipole and hence depolarize the subsequent radiation. The necessity to describe the polarization spectrum of the fluorescence as well as its intensity spectrum acts as a further constraint on the potentials extracted from the data inversion technique.

The field of Collisional redistribution has been reviewed by Burnett (1985). The reader is referred to this review for a more detailed discussion of the physics involved and for its bibliography. Historically the interest in collisional redistribution has come from the astrophysical community. Stellar atmospheres have high optical depths and in order for a photon to escape it must be redistributed away from linecentre to an optically thin region of the spectrum. This redistribution can occur as a result of collisions or alternatively as a result of the Doppler effect. Redistribution by the Doppler effect is described by Mihalas (1970) and will not be considered here.

Weak field collisional redistribution theory applicable to the impact region has been developed by Omont *et al.* (1972,1973) and by Huber (1969). In a manner analogous to the case of spectral lineshapes, redistribution experiments conducted in the quasistatic wing should be capable of probing the interaction potentials in a more systematic way than experiments carried out in the impact region. Following the first quasistatic wing experiments of Carlsten *et al.* in 1977 the need was apparent for a generalization of redistribution theory to cover the entire line profile. Such generalizations have been put forward by Cooper (1979) and by Burnett *et al.* (1980a,b,c) in a comprehensive series of papers.

The theory of Burnett and Cooper is quite formal and has a very wide range of applicability. It depends on density matrix and projection operator techniques. Although it gives analytical results for the general redistribution problem, evaluation of the operators involved for particular cases is difficult.

Furthermore the generality of the formalism, while essential in certain cases, complicates matters when simpler limiting cases are treated.

For the systems of Sr and Ba perturbed by rare gasses, a simpler, less rigorous theory has been put forward by Lewis *et al.* (1983) to describe the depolarization of the collisionally redistributed radiation. In their model they describe the collision complex as a transient quasi-molecule and use geometrical arguments to calculate the resultant polarization. Attempts will be made to apply this model to the Hg-Kr system. In the following sections the discussion will however proceed in the context of a $^1P_1$—$^1S_0$ transition which is the relevant case for the alkali–Rare-Gas experiments reported in the literature. The complications that arise in the case of the Hg 2537 Å($^3P_1$—$^1S_0$) transition will be discussed in Chapter 3. It should be noted that the molecular model itself can be derived from rigorous quantum mechanical theory of collisions in the presence of radiation (eg. Mies & Julienne 1986)

2.3.2 The Molecular Model: General.

Grosser (1981) discusses in detail the conflict between the atomic and molecular pictures of ^1S_o–$^1P_1$ atom – atom collisions. The disagreement between the two pictures becomes apparent when one considers the angular momentum of the states involved. When the interaction between the collision partners is small the motion should resemble that of free atoms and the angular momentum vectors should remain fixed in space. However when the interaction between the pair is strong a molecular picture is appropriate and it is the projection of the angular momentum vectors onto the internuclear axis that should be conserved. This axis rotates by 180° in a collision. The two pictures are therefore in severe conflict.

Practical difficulties arise when we want to calculate observables that result from interactions which occur across the boundary between a region of small interatomic distances, in which the molecular picture holds and the angular momentum vector rotates, and a region of larger interatomic separation in which the angular momentum remains space fixed.

Grosser points out that when one chooses to approach the problem using molecular eigenfunctions (Σ and Π states for the $^1P_1$—$^1S_0$ transition he considers) a Σ–Π coupling term becomes important at large r and Λ is not conserved in this region. The coupling term can be regarded as being due to coriolis forces exerted on the electrons in the frame of the rotating axis. These coriolis forces will always be present, however at small r they will be negligible in comparison to the forces which couple the wavefunction to the molecular axis.

The strength of the coupling of the electronic angular momentum to the molecular axis at a given r is represented by the Σ,Π potential difference. The molecular picture becomes inappropriate when this coupling is comparable to the coriolis coupling between the Σ and Π states.

An utilitarian method of dealing with this problem in semiclassical calculations is to define a radius R_L within which the molecular picture holds rigorously and outside of which the atomic picture is used. In an experiment in which an excited atom undergoes collisions R_L is the "locking radius" ie. the interatomic separation at which the atoms are considered to lock together to form a rigid molecule which then rotates through the collision. In the experiments that we have performed excitation occurs directly to the molecular state *during* the collision and therefore $R_L \equiv R_{dc}$ is a radius at which the partners *decouple* to their asymptotic atomic states. The utility of this approach hinges on how abruptly in r the changeover occurs. This in turn depends on the evolution in r of the Σ–Π potential difference.

2.3.3. Choice of R_{dc}

The degree of depolarization experienced in a collisional redistribution experiment depends on the amount of reorientation of the angular momentum vectors that occurs during the collision. This in turn will obviously depend on the value of R_{dc}. For any model based on the idea of a decoupling radius to be useful, a sensible way of choosing R_{dc} must be found.

Grosser investigated the problem by writing down coupled equations for the probability amplitudes of assumed molecular eigenfunctions. He started with an eigenfunction of pure Σ character at large r and integrated his equations to

smaller r. His results are shown in fig 2.3. Initially as r decreases the state begins to take on a certain amount of Π character. In the region where the coriolis term becomes important the solutions for the probability amplitudes begin to oscillate about a mean value. In this region Λ is conserved. The onset of such oscillations is an indication that the transition zone between the atomic and molecular regions has been reached. Using the condition that the coriolis coupling be comparable to the Σ–Π potential difference he was able to find an analytical form for R_{dc} when $V_\Sigma - V_\Pi$ can be written as an inverse power law in r. His result is given by

$$R_{dc} = \left| \frac{\Delta C_n}{(n-1)\hbar\bar{v}} \right|^{1/n-1} \qquad (2.44a)$$

, for $V_\Sigma - V_\Pi = \Delta C_n / r^n$. Accepting the basis set of eigenfunctions of pure Σ and pure Π character at $r \to \infty$ to be a poor representation at small r Grosser sought approximate solutions that were well behaved in this region but were without physical significance at large r.

Lewis *et al.* choose to define R_{dc} through

$$\frac{1}{\hbar} |V_\Sigma(R_{dc}) - V_\Pi(R_{dc})| = \frac{1}{\tau_c} \qquad (2.44b)$$

on the grounds that $\hbar/\tau_c$ is the smallest energy separation that the collision can discern. It should be noted however, by inspection of the expressions

$$x^2 + b^2 = R_{dc}^2$$

and

$$\frac{x}{R_{dc}} = \sin\phi$$

(see fig 2.5)* that for a given impact parameter and a value of ϕ greater than $\sim 45°$ a large change in R_{dc} produces rather a small change in ϕ. In terms of the reorientation experienced during a collision the model is therefore less sensitive to a bad choice of R_{dc} than one might initially expect.

In an experiment to test the molecular model in which the potentials are well known R_{dc} acts as the only parameter which need be adjusted in order to fit the data. The model will be deemed a success if a good fit to the data can

* x is the side opposite to the angle θ_α in the triangle whose other two sides are b and R_α.

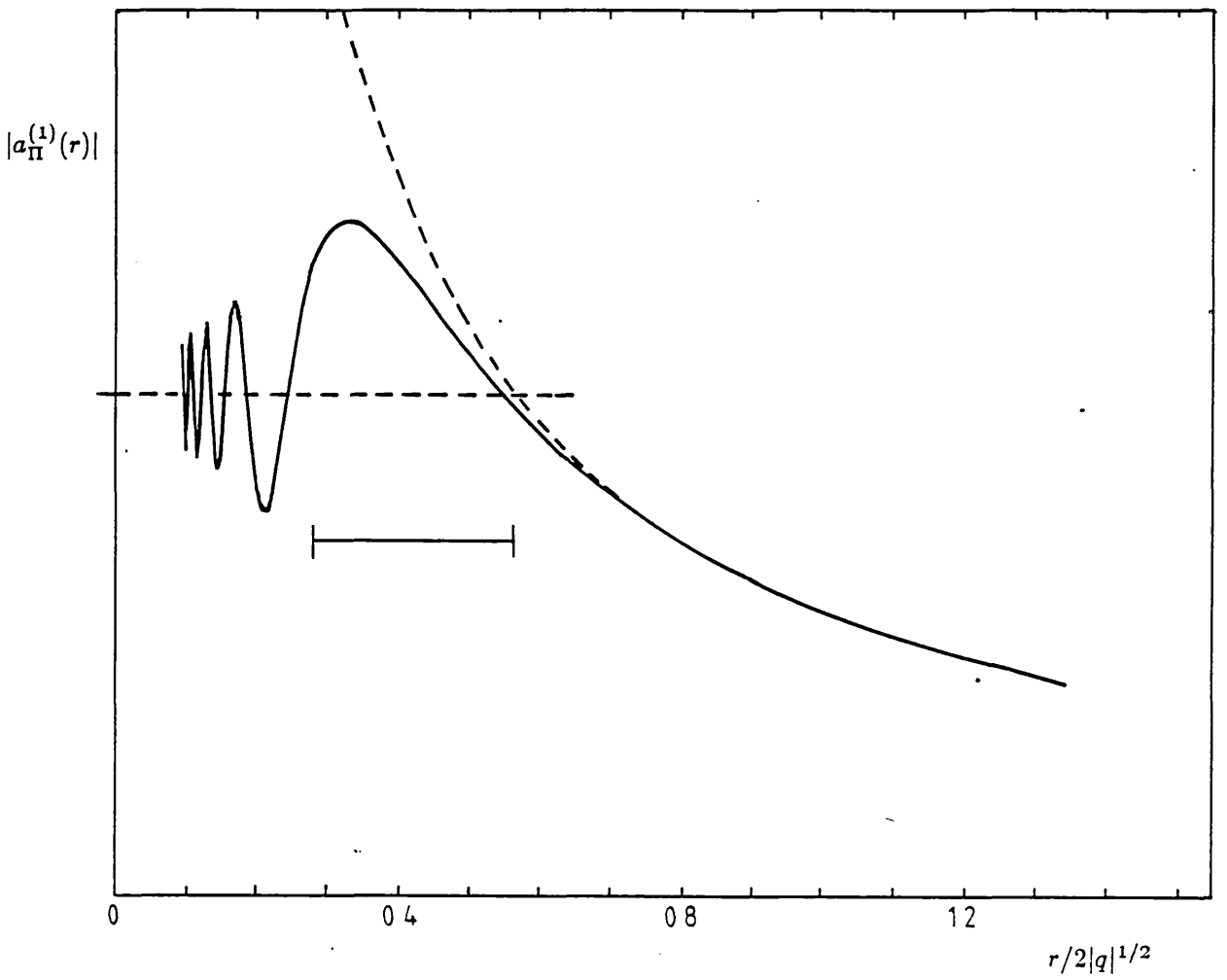


Figure 2.3 Transition between $|\Sigma\rangle$ and $|\Pi\rangle$ character during a collision. $|a_\Pi^{(1)}(r)|$ for the r^{-3} potential in the small impact parameter approximation. The development of a wavefunction corresponding to a pure $|\Sigma\rangle$ state at infinity is shown. As long as the function is close to b/r (broken curve), the wavefunction is space fixed. Where the function is constant (broken line) Λ conservation holds. (From Grosser (1981)).

be achieved with a single R_{dc} which is independent of impact parameter and velocity.

2.3.4. Formulation of the Molecular Reorientation Model

The fundamental ideas to understand in attacking the problem are illustrated in fig 2.4. We take it that the complex is excited by the incident radiation of frequency ω at a point in the collision where $\{V(R)-V(\infty)\}/\hbar \gg 1/t_c$ where t_c is the collisional duration at impact parameter b. In other words we assume we are in the region of validity of quasistatic theory and the ensuing results hold true only in the line wings.

The calculation follows the usual quasistatic proc-edure ie. to consider the effect of a particular collision and then to average over all collisions. As will be seen the average over collisions is complicated by the fact that the polarization and direction of the incident light define a laboratory axis. This average must therefore explicitly involve an average over all possible orientations of the complex with respect to the laser field.

Fig 2.5 shows the essential features of the model. The optically active atom, travelling in the $-x$ direction sweeps past a perturber situated at the origin. Excitation occurs at the Condon point. The atom has two chances to be excited ie at $+$ or $-\theta$. The atoms then couple together and move through the collision along a straight line trajectory until the point R_{dc}. The now free atom continues along its path until it fluoresces at a later time according to the natural lifetime of the state. We consider the case where fluorescence occurs before another collision has time to take place. This puts a fundamental limit on the perturber pressure at which experiments can be conducted. The effect of second collisions that occur within the natural lifetime of the state will be discussed in Chapter 5.

To understand the coupling and decoupling processes and their effects on the polarization of the fluorescence we turn to a picture of the collision in which the states are represented by p_x, p_y and p_z orbitals and look at the different ways in which these orbitals couple depending on their orientation with respect to the internuclear axis. Fig 2.6 shows the three cases of interest. In a) we see

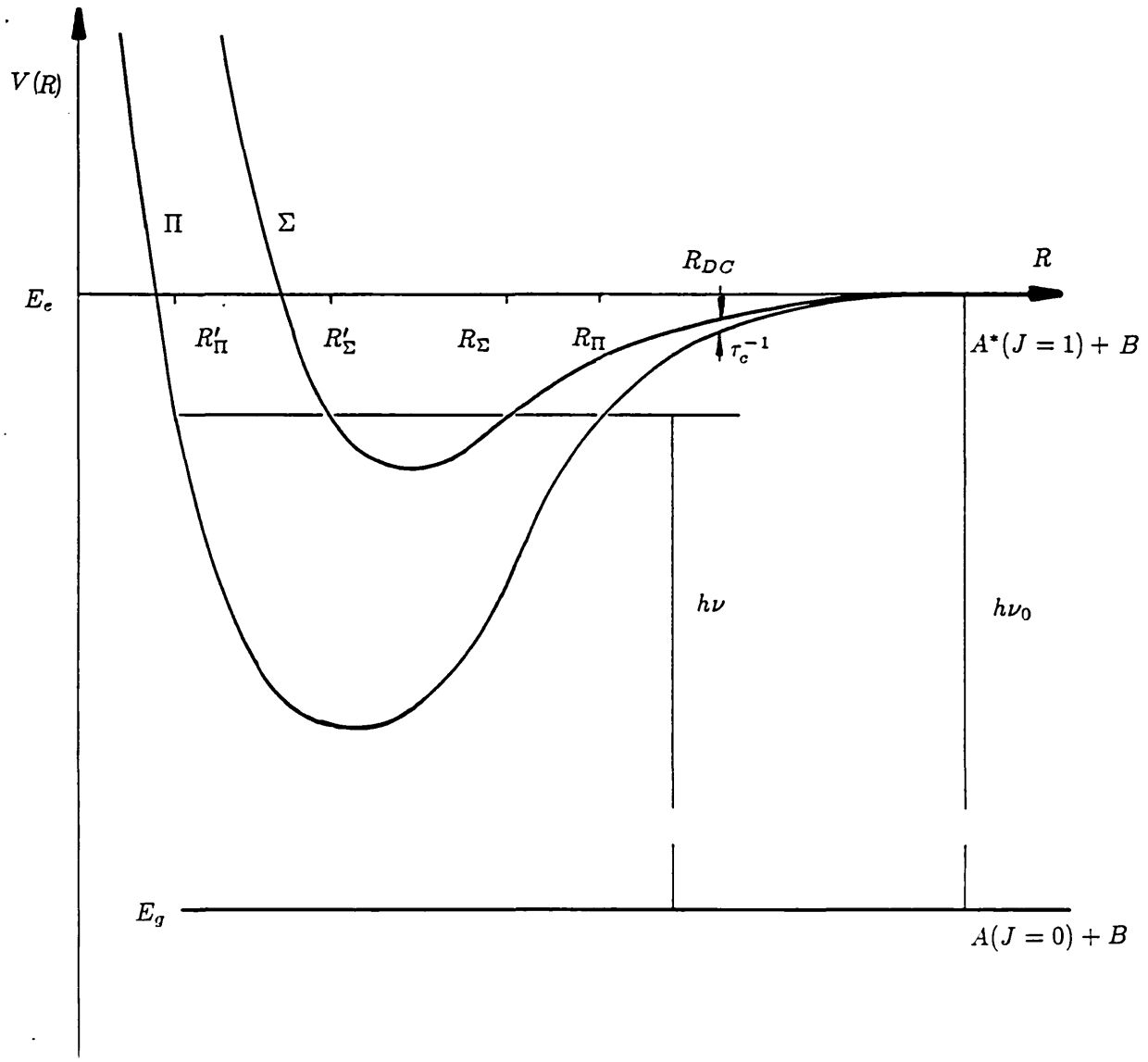


Figure 2.4 Schematic potentials for a $^1P_1$–$^1S_0$ transition.

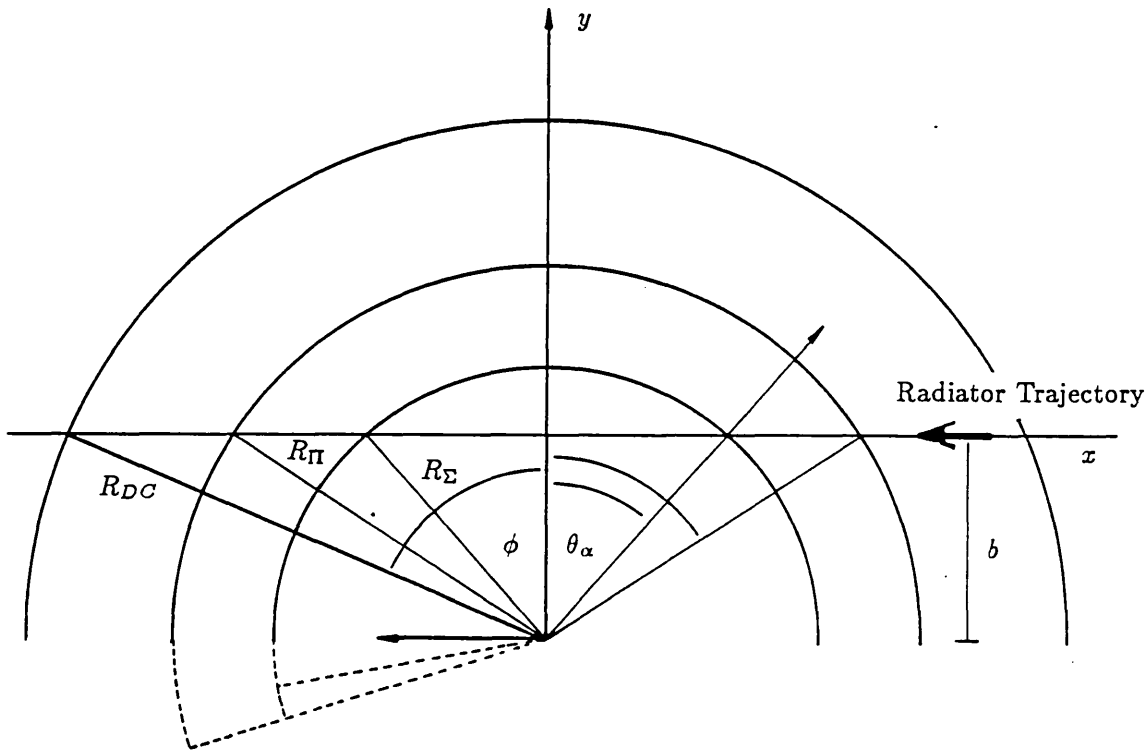


Figure 2.5 Geometry in the collision plane. Excitation occurs at R_Σ or R_Π, the Condon point. Note that there are two chances for excitation; entering and exiting the collision. Since the Condon point is defined as a *radial* position these two chances occur at the *same* Condon point. The molecular description holds for $R < R_{dc}$.

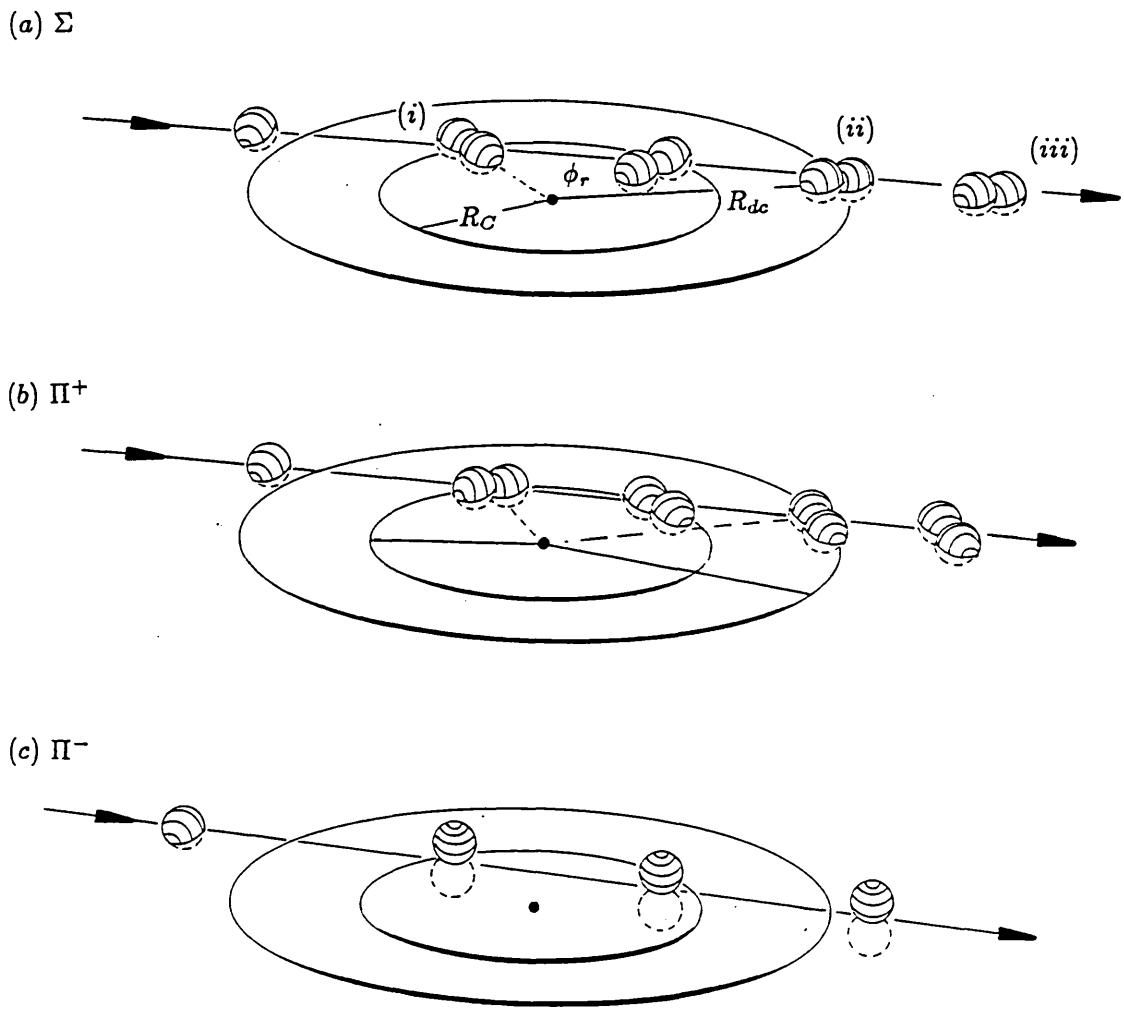


Figure 2.6 Orbital reorientation during a collision. The time evolution of the molecular orbitals is illustrated from (i) the point of absorption at R_C to (ii) the point of decoupling at R_{dc}, for the three cases of excitation to the (a) Σ state, (b) Π^+ state, and (c) Π^- state. Radiative decay occurs at point (iii). The reorientation angle ϕ_r is equal to $\phi + \theta_\alpha$.

Σ excitation. Here the orbital is excited at the Condon point and the orbital points along the internuclear axis. As the atom moves along its path the coupling ensures that the orbital remains pointing along the internuclear axis during the collision.

The rotation of the orbital described here manifests itself as depolarization of the incoming light when the averages over angles, impact parameter and energy have been performed. In b) we see the same sort of process for a Π^+ orbital where we note that R_c is now different from that in a). The + refers to reflection symmetry in the collision plane. In c) we see what happens in the case of Π^- excitation. This case is distinguished from the first two in that the orbital retains the same orientation throughout the collision. We should therefore not expect excitation to a Π^- orbital to contribute to depolarization.

Bearing this in mind and referring to fig 2.4 an essential feature of the model can now be noted. As the frequency of the incoming radiation is reduced the well in the Σ potential is approached. With a further decrease in the frequency of the incoming light the well is passed and a region is reached in which classically, excitation can only occur to the Π potential. The polarization and intensity of the radiation in the far red wing will therefore be determined by the Π potential alone. This will prove a very important tool in labelling the states.

2.3.5 Calculation of the Polarization of the Collisionally Redistributed Fluorescence.

The experimental geometry is defined in fig 2.7. The exciting light at frequency ω is incident along the $-x$ direction and is scattered by the atoms in the region of the origin. The collisionally redistributed light at linecentre is observed in the direction (Θ, Φ). The geometry of any particular collision is defined by the impact parameter b and the velocity v as shown in fig 2.5. In a thermal cell the collision frame can have any orientation with respect to the laboratory frame. The collision axes (x_c, y_c, z_c) are related to the laboratory axes (x_l, y_l, z_l) by the Euler angles $(\alpha\beta\gamma)$ (Brink & Satchler, 1962).

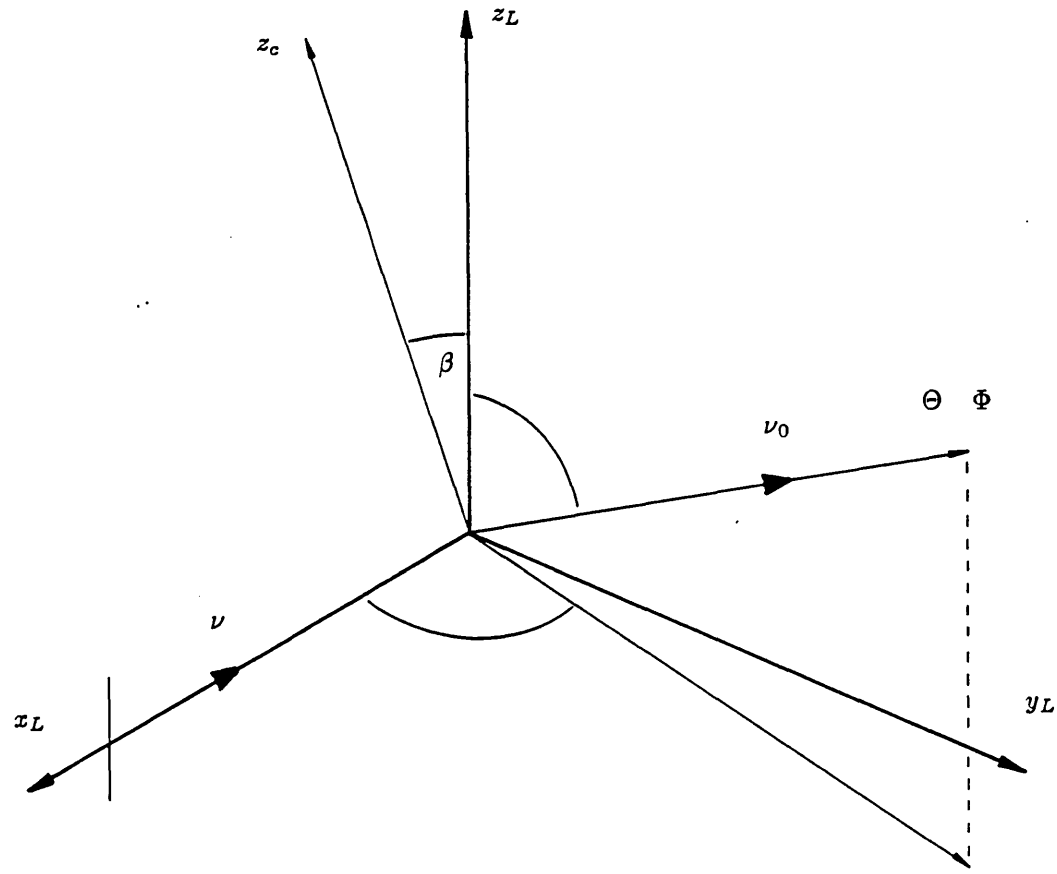


Figure 2.7 Experimental geometry. Exciting light impinges along $-x_L$. Redistributed fluorescence is detected in the direction (Θ, Φ). The collision frame is related to the laboratory frame via the Euler angles (α, β, γ). (From Alford *et al.* (1983)).

We express the electric field in the laboratory frame in terms of the spherical tensors $\mathbf{T}$.

$$E_L = \sum_q \epsilon_q \mathbf{T}^1_q \tag{2.45}$$

This is a convenient representation since spherical tensors are more closely related to the properties of angular momentum states in quantum mechanics than are vectors ie. states of definite angular momentum can be constructed as $|m = \pm 1\rangle = \mp(1/\sqrt{2})(p_x \pm ip_y)$ and $|m = 0\rangle = p_z$. Use of these tensors therefore simplifies the algebra and facilitates better understanding of the equations. Exactly the same results have been found by Andersen (1985) using a vector representation. Transforming to the collision frame we have

$$E_c = \sum_{qp} \epsilon_q \mathbf{D}^{1*}_{qp}(\alpha\beta\gamma)\mathbf{T}^1_p \tag{2.46}$$

Transforming again to the molecular frame (x_m, y_m, z_m) defined by z_m being along the internuclear axis, we have

$$E_m = \sum_{qpr} \epsilon_q \mathbf{D}^{1*}_{qp}(\alpha\beta\gamma)\mathbf{d}^1_{pr}(\pm\theta)\mathbf{T}^1_r \tag{2.47}$$

Where the *reduced* rotation matrix $\mathbf{d}^1_{pr}$ can be used since the rotation is about one axis only. The colliding atoms are then coupled into a Σ or Π state. Dipoles of magnitude μ_Σ and μ_Π are induced independently for the Σ and Π states giving

$$\mu_M(\Pi) = \mu_\Pi \sum_{\substack{pq \\ r=\pm 1}} \epsilon_q \mathbf{D}^{1*}_{qp}(\alpha\beta\gamma)\mathbf{d}^1_{pr}(\pm\theta)\mathbf{T}^1_r \tag{2.48a}$$

$$\mu_M(\Sigma) = \mu_\Sigma \sum_{pq} \epsilon_q \mathbf{D}^{1*}_{qp}(\alpha\beta\gamma)\mathbf{d}^1_{p0}(\pm\theta)\mathbf{T}^1_0 \tag{2.48b}$$

The molecular states are assumed to develop independently through the collision according to their particular molecular potential until R_{dc} is reached. This assumed independence of the molecular potentials should be treated with caution. The consequences of making this approximation for the Hg $(^3P_1 — ^1S_0)$–Kr system will be discussed in Chapter 6. Transforming back to the collision frame

the dipole moment will depend on whether the excitation was via the Σ or Π states and will be given by

$$\mu_C(\Sigma,\Pi) = \mu_{\Sigma,\Pi} \sum_{pqrs} \epsilon_q \mathbf{D}^{1*}_{qp}(\alpha\beta\gamma)\mathbf{d}^1_{pr}(\pm\theta)\mathbf{d}^1_{rs}(-\phi)\mathbf{T}^1_s \tag{2.49}$$

where $r = 0$ for Σ and $r = \pm 1$ for π states. Finally transforming back to the laboratory frame yields

$$\mu_L(\Sigma,\Pi) = \mu_{\Sigma,\Pi} \sum_{pqrst} \epsilon_q \mathbf{D}^{1*}_{qp}(\alpha\beta\gamma)\mathbf{D}^1_{st}(\alpha\beta\gamma)\mathbf{d}^1_{pr}(\pm\theta)\mathbf{d}^1_{rs}(-\phi)\mathbf{T}^1_t \tag{2.50}$$

Now each collision process is independent so the intensities from each excited atom must be calculated and integrated over Euler angles. The treatment so far has been classical in terms of components of tensors. The tensors are convenient in that they facilitate a more quantum mechanical interpretation of the equations. In eq.$^{2.50}$ we can take $\mathbf{T}^1_t$ to represent the $|J,m_j\rangle$ state $|1,t\rangle$ and the coefficient of $\mathbf{T}^1_t$ to represent the quantum mechanical amplitude C_{Jm} for being in that state. The population of the state is then given by $C^*_{Jm}C_{Jm}$. Since we expect all excited atoms to relax radiatively to their ground state this population will be fully depleted and represents a measure of the intensity of the light being radiated from this state. The parameter measured in an experiment is the polarization, defined by

$$P = \frac{I_z - I_x}{I_z + I_x} = \frac{3\alpha^{(2)}(\Delta\omega)}{2 + \alpha^{(2)}(\Delta\omega)} \tag{2.51}$$

where $\alpha^{(2)}(\Delta\omega)$ is called the longditudinal polarization and is given by

$$\alpha^{(2)}(\Delta\omega) = \frac{I_z - I_x}{I_z + 2I_x} \tag{2.52}$$

We want to calculate P for the case of excitation via linearly polarized light. To do this we must calculate I_z and I_x . Such calculations involve orthogonality and contraction properties of the rotation matrices (Blum 1981). The result for $\alpha^{(2)}(\Delta\omega)$ is quoted below

$$\alpha^{(2)}{}_{(\Delta\omega)} = \frac{\left[\frac{1}{6} + \frac{1}{10}(2\langle\cos(\phi-\theta_\Pi)\rangle + \langle\cos 2(\phi-\theta_\Pi)\rangle)\right] + g(\Delta\omega)(\frac{1}{30} + \frac{1}{10}\langle\cos 2(\phi-\theta_\Sigma)\rangle)}{(\frac{2}{3} + \frac{1}{3}g(\Delta\omega))} \tag{2.53}$$

In this expression $g(\Delta\omega)$ is the probability of exciting the Σ state relative to exciting a Π state and the average over angles is denoted $\langle \ldots \rangle$. Both of these effects come in as a result of the average over impact parameters.

2.3.6. The Average Over Collisions.

In a collision with initial relative velocity $v(\infty)$ and impact parameter b the probability of absorption at ω is given by the general quasistatic result *eq*.2.39. We now simplify the average over velocities (energies) by using an average velocity only. Furthermore for straight line trajectories $b = R\cos\theta$ and the equation becomes

$$I(\omega) = n_0 4\pi R^2 \frac{dR}{dv} \times \frac{1}{2}\int_{-\frac{\pi}{2}}^{\frac{\pi}{2}} \cos\theta_\alpha \, d\theta_\alpha \tag{2.54}$$

With $\alpha = \Sigma, \Pi$. Summing over collisions for which absorption can take place is accomplished by integrating over θ_α yielding

$$I(\omega) = \frac{n_0 4\pi R_c^2}{\left|\frac{dV}{dR}\right|_{R_c}} \tag{2.55}$$

which is the quasistatic result. The Boltzmann factor is missing as a result of neglecting the integration over the Maxwellian velocity distribution. The expression $g(\Delta\omega)$, which is given by the ratio of μ_Σ^2 to μ_Π^2, can be written down as $I(\omega)_\Sigma / I(\omega)_\Pi$ yielding

$$g(\Delta\omega) = R_\Sigma^2 \left(\frac{dV}{dR}|_{R_\Sigma}\right)^{-1} \left[R_\Pi^2 \left(\frac{dV}{dR}|_{R_\Pi}\right)^{-1}\right]^{-1} \tag{2.56}$$

2.3.7. Parameterization in Terms of R_α / R_{dc} .

The average over impact parameters is transformed into an average over θ_α as in eq.2.54. Explicitly we use

$$\langle \ldots \rangle = \frac{1}{2}\int_{-\pi/2}^{\pi/2} \cos\theta_\alpha \, d\theta_\alpha (\ldots) \tag{2.57}$$

Inspection of fig 2.5 gives the relations

$$\cos\phi = b/R_{dc}$$
$$\cos\theta_\alpha = b/R_\alpha \tag{2.57}$$

Using these relations it is possible to write the terms denoted $\langle \ldots \rangle$ in eq.2.53 in a form dependent on only R_α/R_{dc} and $\cos\theta_\alpha$. Once the average over θ_α has been accomplished these terms can be expressed as a function of R_α/R_{dc} alone. If we use equation 2.51 it is possible to write the polarization in terms of $X_\alpha \equiv R_\alpha/R_{dc}$

$$P = \frac{15 + 15X_\Pi + X_\Pi^2 + g(\Delta\omega)9X_\Sigma^2}{55 + 5X_\Pi + 3X_\Pi^2 + g(\Delta\omega)(25 + 3X_\Sigma^2)} \tag{2.58}$$

The polarization P_Π, measured when excitation is via the Π curve only , is obtained by letting $g(\Delta\omega) \rightarrow 0$. Conversely P_Σ is obtained by letting $g(\Delta\omega) \rightarrow \infty$. The functions P_Π and P_Σ are shown in figure 2.8 (see Andersen 1985).

It should be noted that there is hardly any overlap between the ranges

$$0\% < P_\Sigma < 32\%$$
$$27\% < P_\Pi < 62\%$$

If the excitation takes place to only one potential curve the polarization of the fluorescence will label it uniquely as a Σ or Π curve. When excitation can occur to both curves the dependence of the polarization of the fluorescence on the *shape* of the potentials enters the problem in two ways: Directly, through $R_\alpha(\Delta\omega)$ and indirectly through the expression $g(\Delta\omega)$ which weights the P_Σ and P_Π contributions.

Lewis *et al.* have calculated $P(\Delta\omega)$ curves for particular potential forms for the Sr—Ar case. Since Chapter 3 will deal with the subject of interatomic potentials we defer until Chapter 6 a discussion of such calculations.

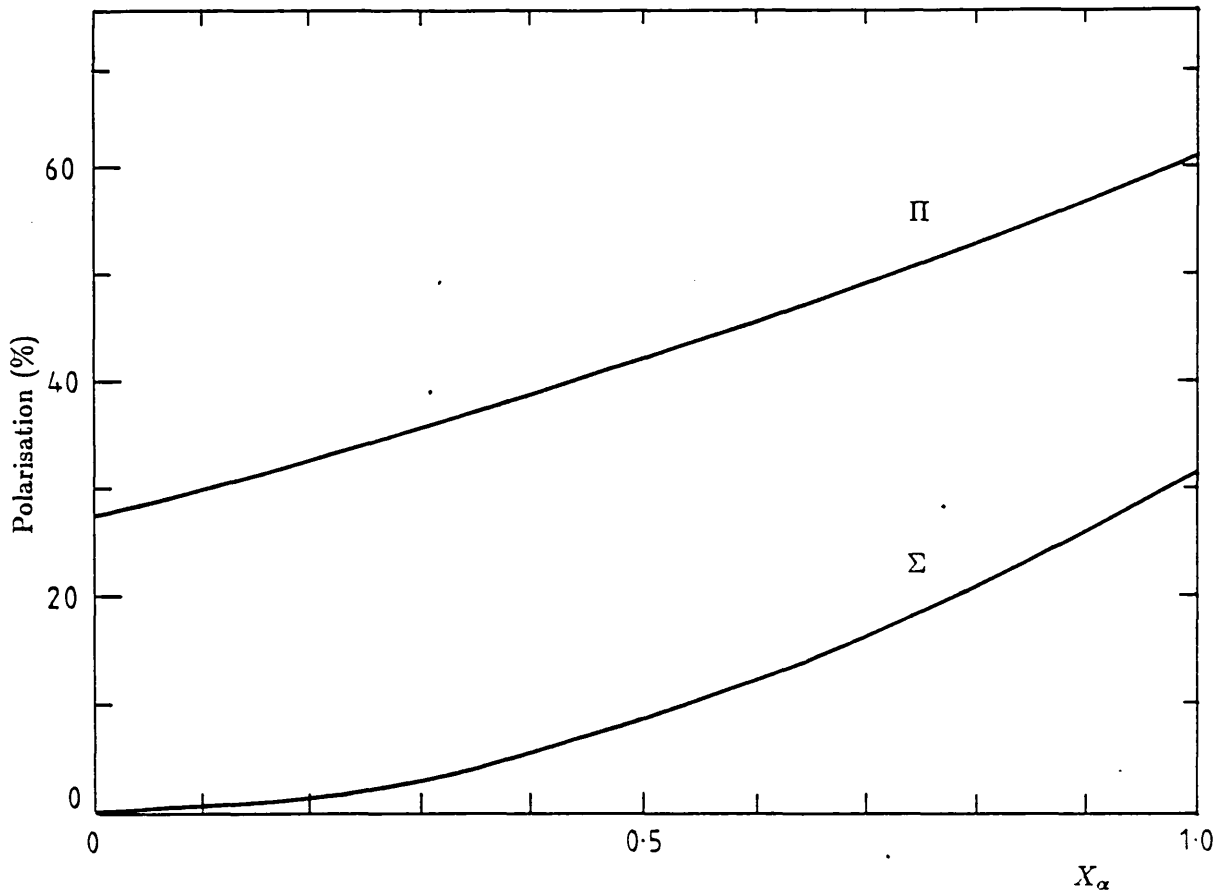


Figure 2.8 Variation of polarisation with X_α. Plot of polarisation versus $X_\alpha \equiv R_\alpha/R_{dc}$ for the two cases of pure Σ and pure Π excitation. Note the lack of overlap between the curves. The polarisation of the collisionally redistributed light allows us to label the interatomic potentials unambiguously.(From Andersen (1985)).

Chapter 3.

Interatomic Potentials

3.1. Introduction.

Previous experiments in Ba and Sr could not provide a quantitative test of the molecular model described in chapter 2 due to the lack of information on the relevant interatomic potentials. Hg($^3P_1$—$^1S_0$)–RG systems have received a great deal of attention recently as possible candidates for an excimer laser scheme, furthermore, experiments in mercury vapour are relatively easy to perform since mercury is a liquid at room temperature. Mercury was therefore chosen for the present study since the potentials for Hg($^3P_1$—$^1S_0$) perturbed by the rare gasses have been accurately determined experimentally by other authors.

Later in this chapter we will examine the interatomic potentials presently available for the Hg($^3P_1$—$^1S_0$)–Kr interaction. In order to do this it is first necessary to review some of the experimental and theoretical techniques used to elucidate interatomic potentials. This is the subject of § 3.2. Section 3.3. reviews the results of recent work specific to the Hg-Kr system and § 3.4. attempts to construct the best possible potentials from the information presented in § 3.3.

Some of the nomenclature used in this chapter is presented in figure 3.1 which shows a typical interatomic potential with a long range attractive component and a short range repulsive term, resulting in a potential minimum at intermediate separations.

It should be noted that throughout this chapter the validity of the Born-Oppenheimer (BO) separation, discussed in chapter 2, is assumed. The potentials discussed are therefore considered to be adiabatic. The results of a breakdown in the BO separation will become apparent later, during the data analysis.

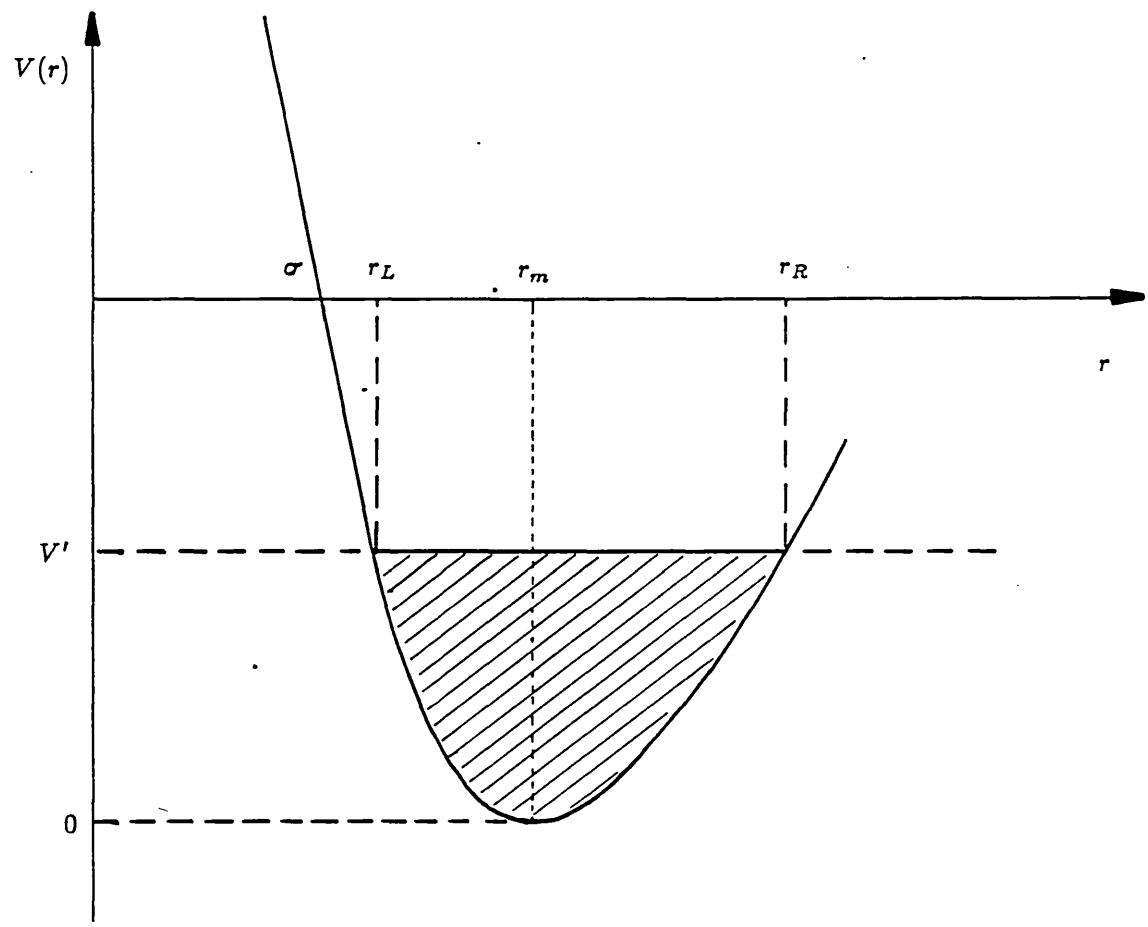


Figure 3.1 Typical interatomic potential: parameters used in Chapter 3.

3.2. Interatomic Potentials : General.

3.2.1. Dispersion Energy.

Atoms in their ground state possess zero time averaged dipole moments. At a given time the electron has a certain probability of being at a particular position within the atom. Classically one can imagine the electron moving randomly within the atom following the probability distribution given by the square of its wavefunction. This random motion leads to the existence of transient dipole moments within the atom. The existence of such a dipole in a mercury atom can induce a dipole in a perturber atom. The result is a net attraction between the atoms. The electric field E set up at the perturber atom by the dipole on the Hg atom is, to first order, proportional to $1/r^3$. The induced dipole moment on the perturber can be written as αE where α is the polarizability. The resulting interaction energy $V_{\rm dis}$ is $-\alpha E.E$ giving

$$V_{\rm dis} \propto -\frac{\alpha}{r^6} \qquad (3.1a)$$

$$= -\frac{C_6}{r^6} \qquad (3.1b)$$

which is the form quoted in chapter 2.

A better expression for E is given by a multipole expansion which includes terms of higher order in $1/r$. The field E may furthermore induce higher order multipoles in the perturber. A more accurate form of $V_{\rm dis}$ is therefore given by

$$V_{\rm dis} = \frac{C_6}{r^6} + \frac{C_8}{r^8} + \frac{C_{10}}{r^{10}} \cdots \qquad (3.2)$$

The higher order terms may be neglected at large r but at separations close to r_m these terms can contribute significantly.

London (1930a,b) showed that *eq*.3.2. could be derived quantum mechanically using perturbation theory and was able to write down expressions for the coefficients C_n in terms of summations over the term values and oscillator strengths of the interacting atoms. An understanding of the perturbation approach can be achieved by examining, as an example, the interaction between

two Hydrogen atoms in their ground states (see Bransden & Joachain 1983). The first atom is composed of a proton situated at A and an electron 1 and the second of a proton situated at B and an electron 2. (See figure 3.2).

The Hamiltonian for the system in the adiabatic approximation, in which the internuclear distance R is fixed is

$$H = H_A + H_B + V(1,2) \tag{3.3}$$

where *eg.* H_A is the Hamiltonian of the atom $(A + e_1^-)$ and $V(1,2)$ is the interaction energy between the two atoms. In atomic units we have

$$\begin{aligned} H_A &= -\frac{1}{2}\nabla^2_{r_{1A}} - \frac{1}{r_{1A}} \\ H_B &= -\frac{1}{2}\nabla^2_{r_{2B}} - \frac{1}{r_{2B}} \\ V(1,2) &= \left(\frac{1}{R} + \frac{1}{r_{12}} - \frac{1}{r_{1B}} - \frac{1}{r_{2A}}\right) \end{aligned} \tag{3.4}$$

The calculation is greatly simplified by making two observations. Firstly, since we are interested in large internuclear separations $V(1,2)$ is small and can be treated as a perturbation. Secondly, since exchange effects due the identity of the electrons occur at short range, we can ignore them.

If the Cartesian coordinates of electron 1 with respect to A as origin are x_{1A}, y_{1A} and z_{1A} and those of electron 2 with respect to B as origin are x_{2B}, y_{2B} and z_{2B} then we can write expressions for r_{12}, r_{1B} and r_{2A} in terms of single atom coordinates and R. *eg.*

$$r_{2A} = \left[x_{2B}^2 + y_{2B}^2 + (z_{2B} + R)^2\right]^{1/2} \tag{3.5}$$

Each of the terms in $V(1,2)$ can be expanded as a Taylor series in $1/R$ and upon substitution into equation 3.4 we get

$$V(1,2) = \frac{1}{R^3}(x_{1A}x_{2B} + y_{1A}y_{2B} - 2z_{1A}z_{2B}) \tag{3.6}$$

This long range interaction has the form of the interaction energy of two dipoles $\mathbf{D}_1 = -r_{1A}$ (in atomic units) and $\mathbf{D}_2 = -r_{2B}$. The energy of interaction is

$$V = \frac{1}{R^3}\left(\mathbf{D}_1.\mathbf{D}_2 - \frac{3(\mathbf{D}_1.\mathbf{R})(\mathbf{D}_2.\mathbf{R})}{R^2}\right) \tag{3.7}$$

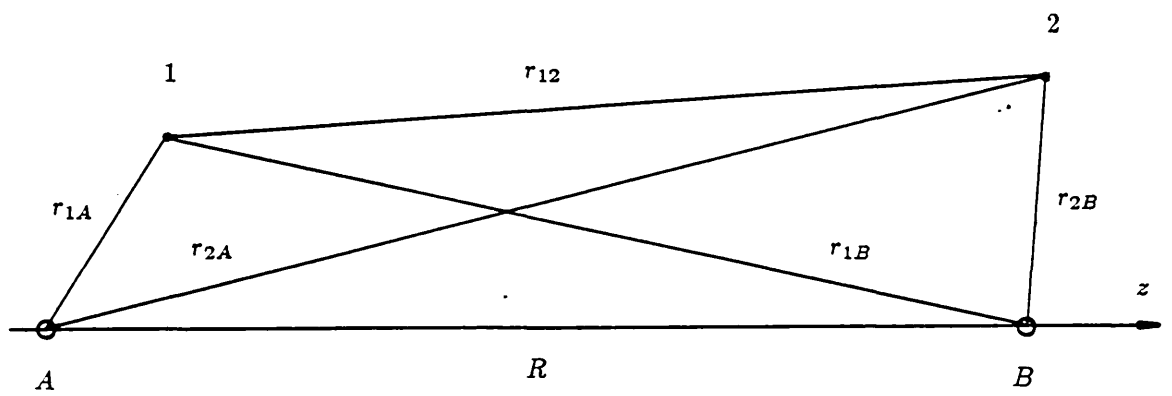


Figure 3.2 Geometry for calculating the van der Waals interaction between two H atoms in their ground states. From Bransden and Joachain (1983). The atoms are taken to be far enough apart that exchange effects due to overlap of the electronic charge clouds can be ignored.

which reduces to equation 3.6 for the geometry of figure 3.2.

The energy of the unperturbed system with both atoms in the ground state is $2E_{1s}$ and the unperturbed wavefunction is $\psi_{1s}(r_{1A})\psi_{1s}(r_{2B})$ which satisfies the equation

$$(H_A + H_B - 2E_{1s})\psi_{1s}(r_{1A})\psi_{1s}(r_{2B}) = 0 \tag{3.8}$$

Allowing for the perturbation $V(1,2)$, the total energy can be written as

$$E = 2E_{1s} + E^{(1)} + E^{(2)} \ldots \tag{3.9}$$

where $E^{(n)}$ is calculated from nth order perturbation theory.

The first order correction ,

$$E^{(1)} = \int d\mathbf{r}_{1A} \int d\mathbf{r}_{2B}\, \psi^*_{1s}(r_{1A})\psi^*_{1s}(r_{2B})\, V(1,2)\, \psi_{1s}(r_{1A})\psi_{1s}(r_{2B}) \tag{3.10}$$

vanishes because the matrix elements of the terms such as x_{1A} etc. are zero when taken between spherically symmetric wavefunctions such as $\psi_{1s}(r_{1A})$. The second order perturbation correction $E^{(2)}$, given by

$$E^{(2)} = \sum_{j \neq 0} \frac{\langle \psi_0 | V | \psi_j \rangle \langle \psi_j | V \psi_0 \rangle}{E_0 - E_j} \tag{3.11}$$

where $\psi_0 = \psi_{1s}(r_{1A})\psi_{1s}(r_{2B})$, need not vanish since the wave functions of the intermediate states ψ_j may be non spherically symmetric. For Hydrogen the ψ_j are of the form $\psi_{nlm}(r_{1A})\psi_{n'l'm'}(r_{2B})$ with n and $n' \neq 1$. The energy denominator is given in atomic units by $(-1 + 1/2n^2 + 1/2n'^2)$, with both n and n' greater than 1, so that $(E_0 - E_j)$ is always negative. The numerator is positive and behaves like $1/R^6$, so that the long range interaction between two hydrogen atoms is

$$E^{(2)}(R) = -\frac{C_6}{R^6} \tag{3.12}$$

where C_6 is a positive constant known as the van der Waals constant. This is identical to equation 3.1. The same proc-edure can be followed for more complicated systems and the applicability of equation 3.12 can be shown to extend to all neutral, non–resonant, atom–atom collisions.

Using London's equations and making certain approximations Ben Lakhdar *et.al.* (1978) have calculated C_6 coefficients for the $^3P_1$ excited state and $^1S_0$ ground state of Hg interacting with Krypton in its ground state. Grycuk & Czerwosz (1981) used these coefficients as input data in attempting to elucidate the ground state potential (see § 3.3.3).

3.2.2. Short Range Repulsion; Methods for Calculation of the Potential.

The short range repulsion mentioned in the introduction sets in when the charge clouds of the atom and perturber begin to overlap. In this region the multipole expansion of *eq.*2.2. loses its physical justification and is no longer a good representation of the interaction. The physics in the region of the potential minimum is complicated with terms in the interaction energy arising from effects such as coulomb repulsion and Pauli pressure.

The most direct method of calculating interatomic potentials in this region is to perform a configuration interaction calculation. The most complex system for which such calculations have been performed with ~ 1 cm^{-1} accuracy is Na-Ar. (Saxon *et.al.* 1977). The Hg-Kr system, with its 116 electrons, is at present inaccessible to such *ab initio* calculations. There exist semi-empirical methods for calculating the interatomic potential at short range known as pseudopotential and model potential methods. In both approaches the potentials are built up by comparing predicted values of a limited set of observables (eg. spectra, polarizabilities) for the *individual* free atoms with experimental data. Parameters in the wavefunctions or potentials are adjusted to give good agreement with the data.

Neither of these semi-empirical methods have been applied to Hg- Rare gas systems due to their complexity. Potentials have therefore been deduced from experimental data by more direct inversion methods.

3.2.3. Useful Analytic Forms.

The short range repulsive part of the potential has often been approximated by the addition of a positive term in $1/r^{12}$ to the van der Waals term yielding the well known Lennard-Jones potential

$$V(R) = 4\epsilon\left[\left(\frac{\sigma}{r}\right)^{12} - \left(\frac{\sigma}{r}\right)^{6}\right] \tag{3.13}$$

The choice of 12 as the exponent in the repulsive term is empirical unlike the attractive term for which the physical justification is given above. The L-J potential has only two adjustable parameters, the well depth ϵ and the collision diameter σ. Furthermore these parameters are only scaling factors and do not affect the *shape* of the potential. It is therefore rather inflexible and cannot be expected to give a good account of the actual potential for real systems.

A more flexible analytical form is the Maitland-Smith potential given by

$$V(r) = \epsilon\left[\frac{6}{n-6}\left(\frac{r_m}{r}\right)^{n} - \frac{n}{n-6}\left(\frac{r_m}{r}\right)^{6}\right] \tag{3.14}$$

where $n = \alpha + \beta(r/r_m - 1)$ and α is usually taken to be 13. This function has proved capable of giving quite accurate descriptions of interatomic potentials despite having only three adjustable parameters. It should be noted however that n is a function of r and hence C_6 calculated from such a potential is a function of r. There exists a wealth of other potential forms (see Maitland,Rigby,Smith and Wakeham. 1981 [Henceforth referred to as MRSW]) most of which include more than three adjustable parameters.

One functional form that stands out from the rest is the Morse potential;

$$V(r) = \epsilon[(1 - e^{-\beta(r-r_m)})^2 - 1] \tag{3.15}$$

Its advantage lies not so much in its ability to mimic actual potentials but in that the Schrõedinger equation is analytically soluble for this potential (see MRSW), with vibrational energy levels given by

$$G(v) = \omega_e(v + 1/2) - \omega_e x_e(v + 1/2)^2 \tag{3.16}$$

in which $\omega_e = (h\beta/\pi)(\epsilon/2\mu)^{1/2}$ is the fundamental frequency and $x_e = \omega_e/4\epsilon$ is the anharmonicity constant. Details of the way in which information on the vibrational levels can be related to the interatomic potential are given in § 3.2.5. and § 3.2.6. The following section discusses the relevant experimental techniques.

3.2.4. Interatomic Potentials from the Spectroscopy of van der Waals Molecules

Study of the spectra of van der Waals molecules has acted as a useful tool in the elucidation of interatomic potentials for a number of years. In the past however, experiments recording such spectra were difficult to perform due to the extremely low proportion of such dimers to be found in a gas at easily accessible temperatures. The recent advent of supersonic nozzle sources has revolutionized the procedure. In such a source a gas is allowed to expand freely through a pinhole from a region of high pressure ($\sim$ 3 atm.) into a vacuum ($\sim 10^{-7}$ atm). The use of skimmers some distance from the pinhole allows the choice of a highly directional beam of atoms with very low transverse velocity components. Separating out the centre of mass velocity from such a beam yields effective temperatures of $\sim$ 1K. At such temperatures dimers formed during three body interactions near the nozzle are very slow to dissociate through thermal collisions.

Nozzle sources therefore allow the efficient production of van der Waals dimers with lifetimes long enough to perform sensitive experiments. The coupling of this technology to the use of tunable dye lasers in crossed beam experiments has greatly advanced our understanding of molecular interactions.

3.2.5 Estimation of the Well Depth Under the Assumption of a Morse Potential.

The spacing between successive levels v and $v+1$ is given by

$$\Delta G_{v+1/2} = \omega_e - 2\omega_e x_e(v+1) \qquad (3.17)$$

A plot of $\Delta G_{v+1/2}$ against v therefore gives a straight line allowing values of ω_e and x_e to be found. Such a graph is known as a Birge-Sponer plot.

The well depth ϵ can be extracted from the data by extrapolating the graph to the v axis. The v intercept, $v_{\max}$ is in general non integer but can be substituted into equation 3.16 to calculate $G(v)_{\max} = D_0 =$ the dissociation energy, whence $D_0 + \omega_e/2 = \epsilon$ gives the well depth. This extrapolation procedure has been used extensively however it should be borne in mind that the Morse function is not in general a good representation for regions of the potential far from the minimum.* In particular, at long range the Morse potential approaches zero faster than the theoretical $1/r^6$ dependence for a van der Waals interaction.

LeRoy and Bernstein (1970) proposed an improved method for determining the dissociation energy which takes into account the asymptotic van der Waals dependence. Their approach started from the first order WKB quantum condition for the eigenvalues of a potential. For the potential they took $V(r) = C_6/r^6$. Furthermore they noted that the largest contribution to the integral in the WKB quantization condition comes from the region near r_R. This enabled them to let $r_L = 0$ and allowed an analytical solution to be found. The resulting expressions are;

$$G(v) = D_0 - [(v_D - v)H_n]^{2n/(n-2)} \tag{3.18}$$

where D_0 is the dissociation limit and v_D is the vibrational index at D_0, and

$$(\Delta G_{v+1/2})^{1/2} = [3(H_6)^3]^{1/2}(v_D - v - 1/2) \tag{3.19}$$

where $H_n = \overline{H}_n/\mu^{1/2}C_n^{1/6}$ and $\overline{H}_6 = 19.94336$ in $cm^{-1}, \mathring{A}, a.m.u.$ units. According to these equations a plot of $(\Delta G_{v+1/2})^{1/2}$ vs. v produces a straight line for the highest levels in the well in contrast to the situation for the lower levels where $\Delta G_{v+1/2}$ should be linear in v.

LeRoy (1972) applied the method to the vibrational states of Ar_2 given by the experimental data of Tanaka and Yoshino (1970) and obtained a considerably improved estimate of the well depth. It should be noted that the above formulae are only valid in the asymptotic region of the potential and can only be applied to the uppermost levels which lie within $\sim 10\%$ of the dissociation limit.

* In regions where the Morse potential gives a poor account of the actual potential the Birge-Sponer plot deviates from straight line behaviour.

Tanaka and Yoshino only resolved the lowest four bound vibrational states and of these only the uppermost one lies in the asymptotic region. It was therefore not possible to fit the four data points to *eq*.3.9. Instead they took the known value of C_6 and calculated H_6. The theoretical slope $[3(H_6)^3]^{1/2}$ was then used and the line constrained to pass through the uppermost experimentally resolved data point.

LeRoy showed that the traditional Birge-Sponer extrapolation procedure predicted 50 % fewer bound states for Ar_2 than the improved method.

3.2.6. The Rydberg-Klein-Rees (RKR) Inversion Method.

Classically one would expect to be able to relate the vibrational energy of a van der Waals dimer to the amplitude of the motion (given by the distance between the turning points) and hence to the well width, whilst one would expect the rotational spectrum to depend on the moment of inertia of the diatomic system and hence on the absolute mean separation of the atoms.

Frequently the rotational structure cannot be experimentally resolved and information on the potential is restricted to a characterization of the well *width* as a function of depth. In this case analysis of the spectrum acts as a useful constraint on the potential but does not determine its *shape* uniquely.

The method used to invert vibrational spectra is a restricted form of RKR analysis. Full RKR analysis includes the rotational spectrum and yields the potential uniquely. The starting point of the RKR method is to write the shaded area in figure 3.1 as;

$$S = \int_{r_L}^{r_R} (V' - V)\, dr \tag{3.20}$$

where the zero of energy is taken as the well depth in this section. Differentiating *eq*.3.10 with respect to V' gives;

$$\left(\frac{\partial S}{\partial V'}\right) = \int_{r_L}^{r_R} dr = r_R - r_L \tag{3.21}$$

Now according to the first order WKB approximation I, the vibrational phase integral $\oint p\,dq$, is quantized according to

$$\oint p\,dq = I = h(v + 1/2) \tag{3.22}$$

Writing the momentum as $p = [2\mu(E - V)]^{1/2}$ gives

$$I = h(v + 1/2) = 2\mu^{1/2} \oint (E - V)^{1/2}\,dr \tag{3.23}$$

Differentiating this with respect to E gives

$$\frac{dI}{dE} = \left(\frac{\mu}{2}\right)^{1/2} \oint \frac{dr}{(E - V)^{1/2}} \tag{3.24}$$

The area S can be related to the phase integral I through the use of a standard integral (see MRSW for a more complete description of the RKR analysis) and solving for $(\partial S/\partial V')$ gives

$$r_R - r_L = \left(\frac{1}{2\pi^2\mu}\right)^{1/2} \int_0^{I'} \frac{dI}{[V' - E]^{1/2}} \tag{3.25}$$

Which can be written as

$$r_R - r_L = \left(\frac{h}{2\pi^2\mu c}\right)^{1/2} \int_0^{n} \frac{dx}{(V_n - V_x)^{1/2}} \tag{3.26}$$

where $x = v + 1/2$ and V_x is in cm^{-1}. The above integral can be performed numerically yielding $r_R - r_L$ as a function of well depth.

3.2.7. Combining Rules for the Determination of ϵ and r_m.

When rotational features cannot be resolved in the spectra of van der Waals dimers another method of determining the absolute value of r_m must be sought. When r_m is known for the dimers of the individual species involved, in this case for Hg_2 and Kr_2, the empirical formula

$$r_{m_{12}} = \frac{(r_{m_{11}} + r_{m_{22}})}{2} \tag{3.27}$$

can be used, where the suffix 12 refers to the unlike interaction. For He-Heavy rare gas interactions this simple formula has been shown to give results that are accurate to within 10%. Other, more complicated rules for both r_m and ϵ have been suggested, which give more accurate predictions. Smith *et.al.* (1977) discuss the merits of various combination rules and conclude that the rule of Kong & Chakrabarty (1973) gives the most accurate results for Rare-Gas–Other Rare-Gas interactions.

3.2.8. Determination of the Potential From Other Sources of Data

We have already seen how the spectra of van der Waals molecules can be inverted to give information on the interatomic potentials. In the previous chapter an inversion method based on the quasistatic theory of line broadening was discussed. As will become apparent later in this chapter, these are the two main methods that have been used to deduce the potentials for Hg-Kr. There exist other methods which have been used extensively elsewhere.

One such method is the scattering of atomic beams. In an atomic beam the kinetic energy of the colliding atoms is restricted to a well defined value. Details of the scattering event and variation of the total cross section with energy depend critically on the pair potential. Scattering data can either be directly inverted to give the potential or, as is more often the case, can be used to determine the parameters of one of the analytical forms mentioned in the previous sections. The relatively large translational energy of the atoms in such a beam means that it is the repulsive wall of the potential that is primarily probed. Since the effect that we wish to investigate depend more on the long range attractive part of the potential, a beam experiment for Hg–Kr would be of limited benefit.

Less direct sources of information on the potential are deviations of the behaviour of real gasses from the perfect gas law and transport properties of gasses. In these cases the information is less direct since an effective average over thermal energies is inherent.

3.3 Interatomic Potentials for Hg-Kr.

3.3.1 General Remarks

The theory presented in chapter 2 confined itself to the case of a $^1P_1 - ^1S_0$ transition and the corresponding p_x, p_y and p_z orbitals of the molecular picture. In this section we turn to the complications that arise in the case of the Hg 2537 Å intercombination line ($^3P_1 - ^1S_0$).

The fact that this line is one of the strongest lines in the spectrum of mercury is attributable to the breakdown of L-S coupling for such a heavy, high Z atom. With the breakdown of L-S coupling the only good quantum number for the atomic angular momentum is J. Similarly, in the molecular picture, Λ (projection of orbital angular momentum on the internuclear axis) is no longer a good quantum number and only $\Omega = \Lambda + S$ is conserved.

In the atomic case, transforming from the $|S, M_s\rangle |L, M_L\rangle$ basis to the $|J, M\rangle$ basis is achieved through

$$|J,M\rangle = \sum_{M_S, M_L} \begin{pmatrix} J & L & S \\ M & M_L & M_S \end{pmatrix} |S, M_S\rangle |L, M_L\rangle \tag{3.28}$$

For the case of J=1, M=0 (with $L = 1$ and $S = 1$) we obtain

$$\begin{aligned} |1,0\rangle = & \sum_{M_S, M_L} \begin{pmatrix} 1 & 1 & 1 \\ 0 & M_S & M_L \end{pmatrix} |S = 1, M_S\rangle |L = 1, M_L\rangle \\ = & \begin{pmatrix} 1 & 1 & 1 \\ 0 & 0 & 0 \end{pmatrix} |0\rangle |0\rangle \\ & + \begin{pmatrix} 1 & 1 & 1 \\ 0 & 1 & -1 \end{pmatrix} |1\rangle |-1\rangle \\ & + \begin{pmatrix} 1 & 1 & 1 \\ 0 & -1 & 1 \end{pmatrix} |-1\rangle |1\rangle \end{aligned} \tag{3.29}$$

and since the first of the three Wigner 3-j symbols in eq 3.29. is zero the expansion is in terms of $M_L = 1, -1$ states alone. Now for the case of J=1,M=1

we have

$$
\begin{aligned}
|1,1\rangle &= \sum_{M_S,M_L} \begin{pmatrix} 1 & 1 & 1 \\ 1 & M_S & M_L \end{pmatrix} |M_S\rangle\,|M_L\rangle \\
&= \begin{pmatrix} 1 & 1 & 1 \\ 1 & 0 & 1 \end{pmatrix} |0\rangle\,|1\rangle \\
&+ \begin{pmatrix} 1 & 1 & 1 \\ 1 & 1 & 0 \end{pmatrix} |1\rangle\,|0\rangle
\end{aligned} \tag{3.30}
$$

giving an expansion in $M_L = \dot{1}$ and $M_L = 0$ states. The atomic states with $M_L = 1, -1$ transform to the molecular basis as Π orbitals whilst the state with $M_L = 0$ transforms to a Σ orbital. It can therefore be seen that the state $|J = 1, M = 0\rangle$ is expressed as a sum over Π states alone whilst the state $|J = 1, M = 1\rangle$ contains a mixture of Σ and Π states.

The labels of the molecular states for Hg-Kr can be assigned as $X^1 0^+ (\Omega = 0)$ for the ground state and $A^3 0^+$ and $B^3 1(\Omega = \pm 1)$ for the excited states. The situation described here for Hg 2537 Å is known as Hund's coupling case C.

We are now in a position to make some qualitative remarks about the interatomic potentials for Hg-RG systems when the rare gas atom is in its $^1S_0$ ground state. Firstly, both the ground and excited states are dominated at long range by an attractive van der Waals term and at short range by a valence repulsion term. In all cases we should therefore expect to see potential wells. We can also make some remarks about the relative depths and positions of the wells for the X,A and B states. The B state has two degenerate components with $\Omega = \pm 1$. These states contain an admixture of Σ component and since it is L that governs the electrostatic interactions these states will become repulsive at larger r than the A state. Furthermore, in the region where the r^{-6} term dominates the B state is more attractive than the A state. The result is that there is a shallower potential well for the B state than for the A state and a resulting curve crossing as shown in figures 3.5 and 3.8.

The ground state is made up entirely of Σ component and would be expected to have a fairly shallow well, however, in the ground state the electrons are closely bound and valence repulsion sets in at smaller r than for the excited states. The ground state well is therefore deeper than the well in the B state

and occurs at smaller R. From these general remarks we should expect the red wing of the absorption line to be dominated by a single satellite associated with the minimum in the B state difference potential.

3.3.2 Potentials Proposed by Fuke *et.al.* (1984)

In this section we discuss a set of interatomic potentials for Hg-Kr deduced by Fuke *et.al.* (1984). They arrive at the potential curves through an analysis of their experimentally obtained vibrational spectrum of Hg- Kr van der Waals molecules. The complexes were produced using a supersonic nozzle source. The fluorescence excitation spectrum was measured by exciting molecules from the lowest vibrational level in the ground state using a frequency doubled tunable dye laser, up to the manifold of vibrational levels in the excited state.

The total fluorescence was monitored and the resolution of the experiment was set by the $\pm 1 cm^{-1}$ bandwidth of the laser. They also carried out experiments on Hg-Ar and Hg-Ne whilst a later paper (Fuke *et.al.* (1986)) describes experiments in Hg-Xe. In the case of Hg-Ar and Hg-Xe, dispersed fluorescence experiments were carried out, in which the laser was tuned to a particular vibrational transition and the relaxation down to the entire ground state manifold measured by scanning a monochromator across the manifold. Unfortunately they do not report dispersed fluorescence spectra for Hg-Kr and their determination of the ground state depends on the analysis of so called "hot bands "ie.fluorescence excitation in the small number of molecules present in the beam, occupying the $v = 1$ vibrational level of the ground state potential.

Their fluorescence excitation results show two manifolds of vibrational bands (see figure 3.3); one to the red and one to the blue of the Hg 2537 Å atomic transition. They were unable to resolve the rotational structure. In analysing their data they adopted the following procedure. First they were able to assign vibrational quantum numbers to the observed bands with the help of limited information from the literature. Next they constructed the Birge-Sponer plot for their data. From the plot they extracted the ω_e and x_e parameters of the Morse potential. The remainder of their analysis consists of various checks

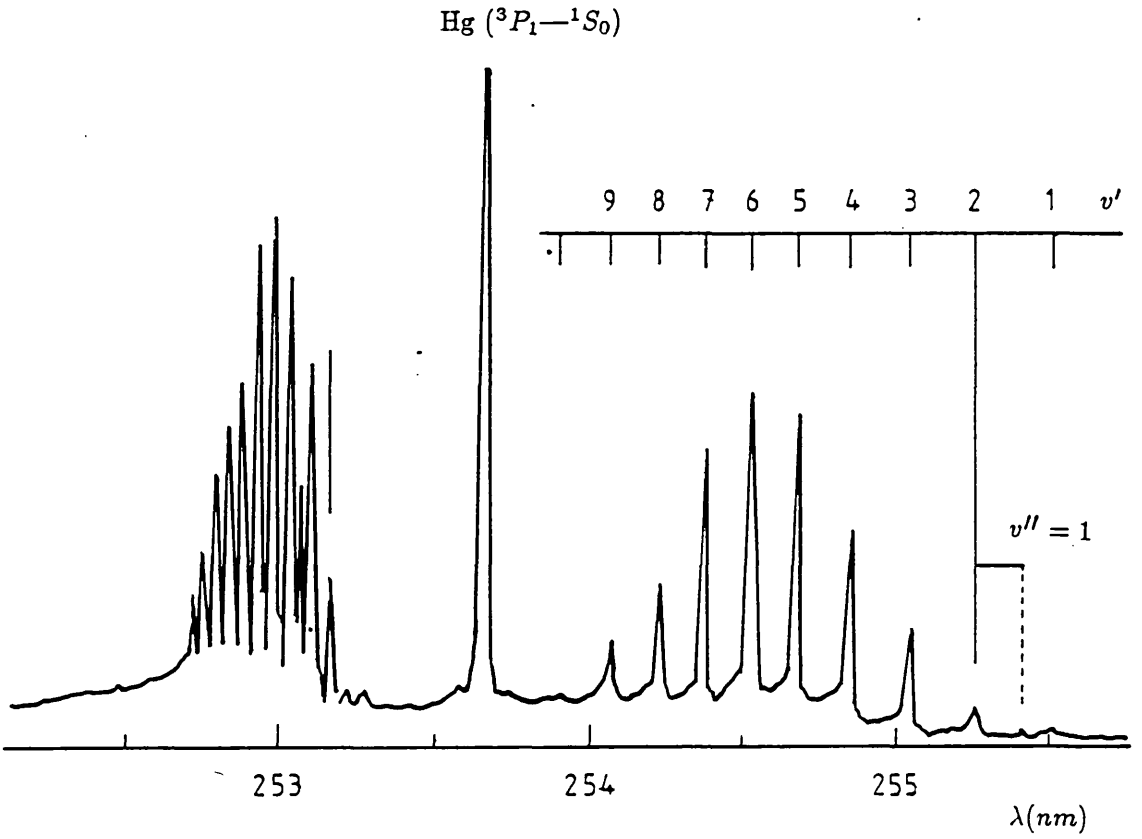


Figure 3.3 Fluorescence excitation spectrum of Hg–Kr in a supersonic free jet in the vicinity of the Hg $^3P_1$—$^1S_0$ line. The groups of bands to the longer and shorter wavelength sides of the Hg line correspond to A–X and B–X transitions respectively. (From Fuke *et al.* (1984))

as to the validity of their proposed Morse functions and a determination of the positions of the well minima.

Since the Birge-Sponer plot for a Morse potential gives a straight line the simplest validity test is to see if there is substantial deviation in the plots from straight line behaviour. They find that the $B^3 1$ state data points fall on a straight line within their experimental errors, right up to the highest observed vibrational level. For the $A^3 0^+$ state they noted considerable deviation, in the form of positive curvature, from a straight line fitted to the lowest six levels (see figure 3.4). This gave a first indication that the Morse function works well for the $B^3 1$ state but fails to give a good account of the $A^3 0^+$ state.

In a further check they performed a restricted RKR analysis and compared the well widths as a function of energy thus calculated with those predicted by their Morse potentials. Again they found good agreement for the $B^3 1$ state and for the lower levels of the $A^3 0^+$ state but noticeable disagreement for the highest four levels of the latter. The ground state potential was not very accurately determined but was found to agree, within the estimated experimental error, with the ground state proposed by Grycuk and Czerwosz (1981).

They determined the positions of the well minima in the following way. Kong's rule was applied to data from the literature on Hg-Hg and Kr-Kr collisions to find the position of r_m for the ground state. They then ran a simulated Franck- Condon factor program to calculate the relative intensities of their vibrational bands. They allowed r_m for the excited states to vary as a parameter and chose the r_m value that gave the best fit to the observed intensities. The parameters for their potentials are summarized in table 3.1 while their potentials are shown in figure 3.5.

Finally it is worth noting that Yamanouchi *et al.* (1988), working at the same laboratory as Fuke *et al.* , have extended the work described here by performing similar experiments in which the rotational structure has been resolved. Unfortunately they only report results for Hg-He, Ne and Ar

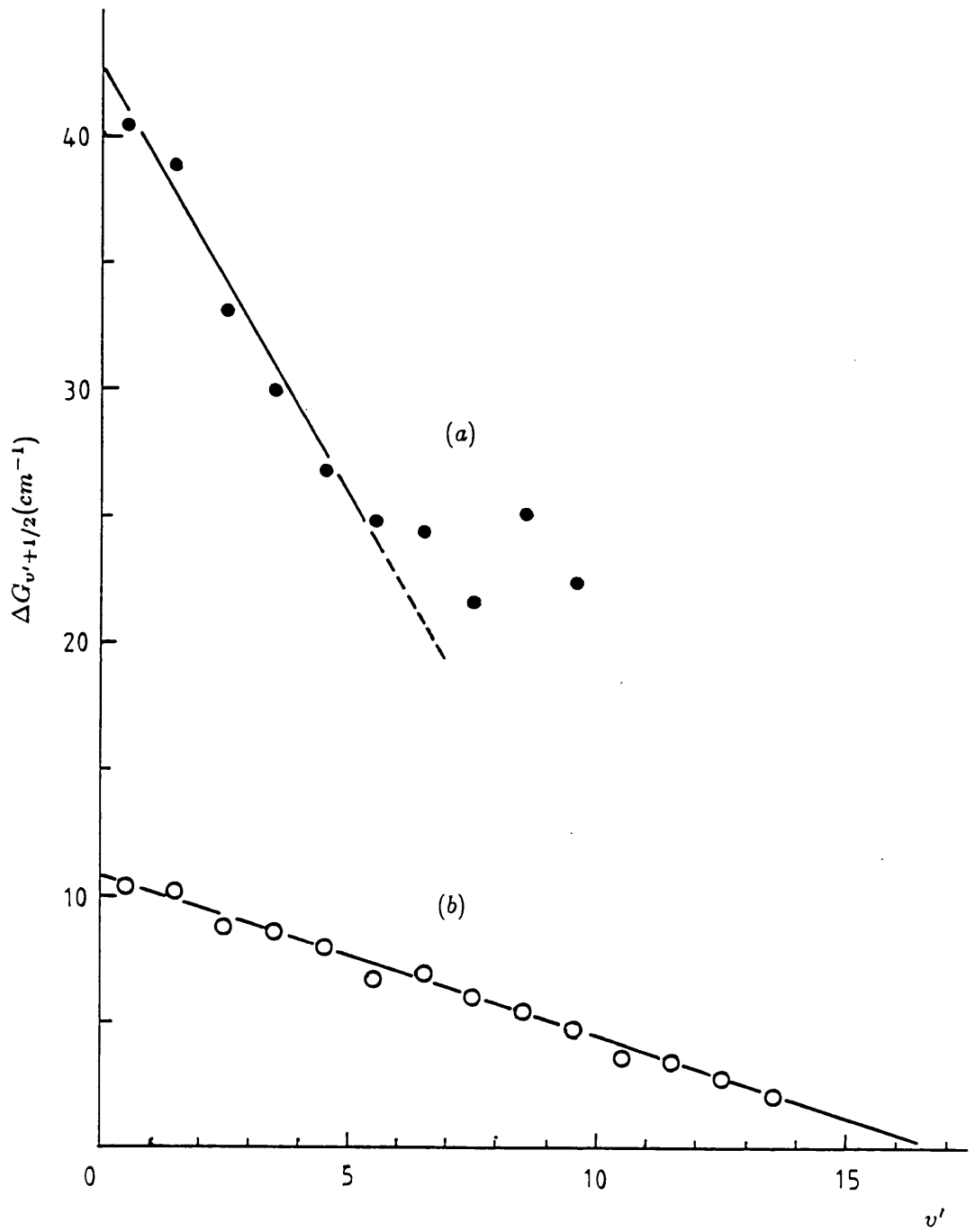


Figure 3.4 Plots of $\Delta G_{v'+1/2}$ vs. v' for (a) A and (b) B states of Hg($^3P_1$—$^1S_0$)– Kr. (From Fuke *et al.* (1984)).

(a) Plot for A state vibrational levels. Note the deviation from straight line behaviour at higher v' indicating the inadequacy of the Morse potential for this state. (b) B state vibrational levels. Good fit to straight line at all v' indicating a successful Morse potential.

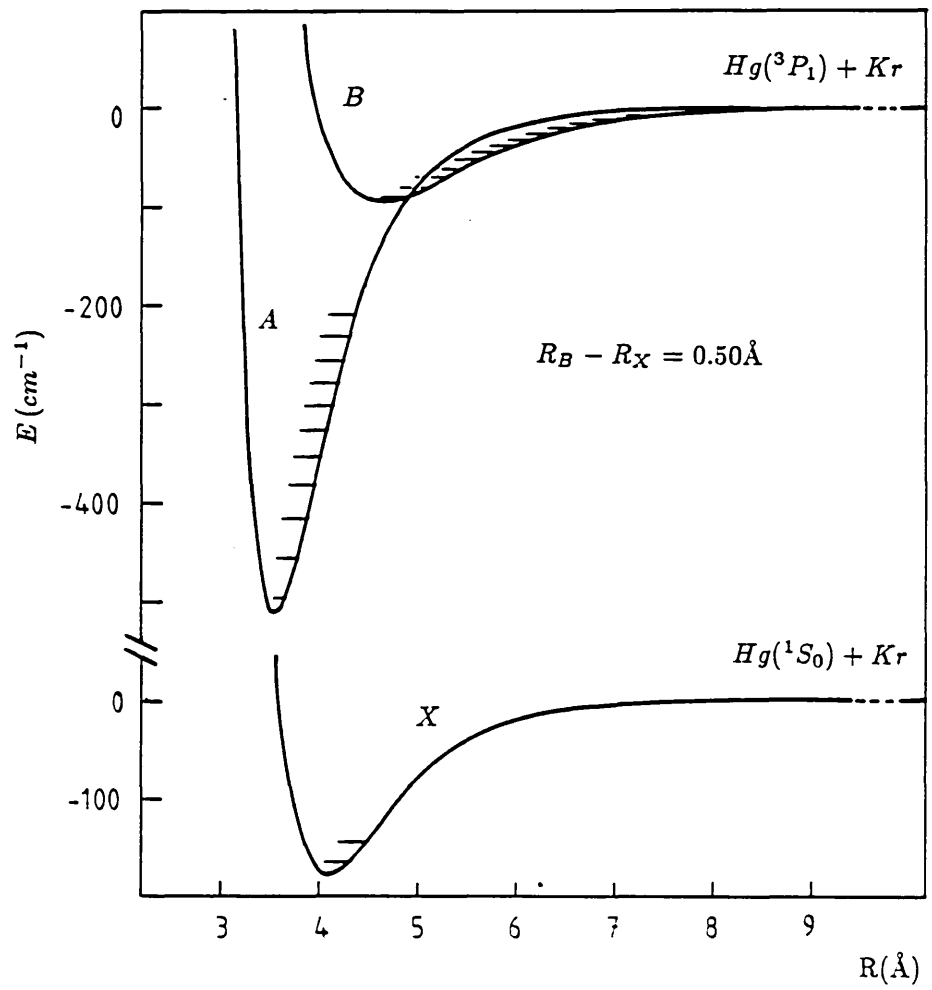


Figure 3.5 X,A and B state potentials after Fuke *et al.* (1984). Morse potentials calculated using the vibrational constants obtained by Fuke *et al.*

Table 3.1.

State.	$\epsilon(cm^{-1})$	$\omega_e(cm^{-1})$	$\omega_e x_e(cm^{-1})$	r_m(Å)
$X^1 0^+$	178	20	.54	4.07
$A^3 0^+$	517	43.3	1.5	3.52
$B^3 1$	96	11.3	0.32	4.57

Summary of potentials proposed by Fuke *et al.* 1984.

3.3.3 Potentials Proposed by Grycuk and Czerwosz (1981)

3.3.3a. Experimental and Theoretical Approach

The above authors approached the problem in quite a different way by performing absorption experiments in high temperature mixtures of Hg-Kr. They then applied the data inversion technique outlined at the end of § 2.2.4. They also collated information available in the literature and by combining this with their own data they were able to elucidate the forms of the potentials.

Use of this data inversion method requires that, for a given detuning, excitation can only occur to a single excited state potential at a single Condon point. ie. that $r(\Delta\nu)$ be a single valued function. As will be seen this condition limits the region over which the method can be applied. For the case of a single Condon point and with the substitution of *eq.*2.33 into *eq.*2.43*a* we can write the temperature and detuning dependent absorption coefficient as

$$k_n(\Delta\nu, T) = C4\pi r^2 \frac{dr}{d(\Delta\nu)} exp(-V_g(r(\Delta\nu))/kT) \qquad (3.31)$$

where C is a constant and the $\Delta\nu$ dependence of r is stressed. Separating out the temperature dependent factor gives

$$k_n(\Delta\nu, T) = k_n(\Delta\nu) exp(-V_g(r(\Delta\nu))/kT) \qquad (3.32)$$

The procedure is then to plot $ln(k_n(\Delta\nu,T))$ against $1/kT$ for a fixed $\Delta\nu$. The slope of the resulting straight line gives $V_g(\Delta\nu)$ and the extrapolation to infinite temperature gives $k_n(\Delta\nu)$.

Note from *eq*.3.17 that the point at which $V_g = 0$ gives a horizontal line on such a plot whilst at a detuning where V_g is positive the slope is negative and where V_g is negative the slope is positive. Integrating $k_n(\Delta\nu)$ gives

$$\int_{\Delta\nu_0}^{\Delta\nu} k_n(\Delta\nu, T \to \infty)\, d(\Delta\nu) = \frac{4}{3}\pi C(r^3(\Delta\nu) - r_0^3(\Delta\nu)) \tag{3.33}$$

which gives $r(\Delta\nu)$. This can then be inverted to yield $\Delta\nu(r)$ and hence, through *eq*.2.33 , $\Delta V(r)$.

Grycuk & Czerwosz measured the absorption spectrum of Hg perturbed by Kr over the range $+250$ — $-1000cm^{-1}$. An attempt was made to perform the experiment in such a way that the effects of Hg-Hg collisions were automatically removed however their experimental set up only allowed this to be achieved at moderate temperatures (up to$\sim 500K$). For higher temperatures (up to 1300 K) the effects of Hg-Hg interactions were determined by independent measurements and subtracted during the data analysis. Their resulting profiles are shown in figure 3.6. Fig 3.7 shows profiles for the same system reported by Ben Lakhdar *et.al.* (1976). The essential features of the profiles are the same, however those of Grycuk & Czerwosz are of higher resolution and extend out to greater detunings in the red wing.

The red wing consists of two linear portions with slope 3/2, separated by a single satellite. The satellite results from an extremum in the ΔV_1 potential. The blue wing comprises three satellites the origins of which are uncertain however Grycuk & Czerwosz propose tentative explanations for these features.

3.3.3b Ground State Potential

There are two regions of the spectrum for which $r(\Delta\nu)$ is single valued. ie. The far red wing, where excitation is via the monotonically decreasing ΔV for the $X^1 0+ - A^3 0+$ transition and in the far blue wing, beyond satellite A. Grycuk

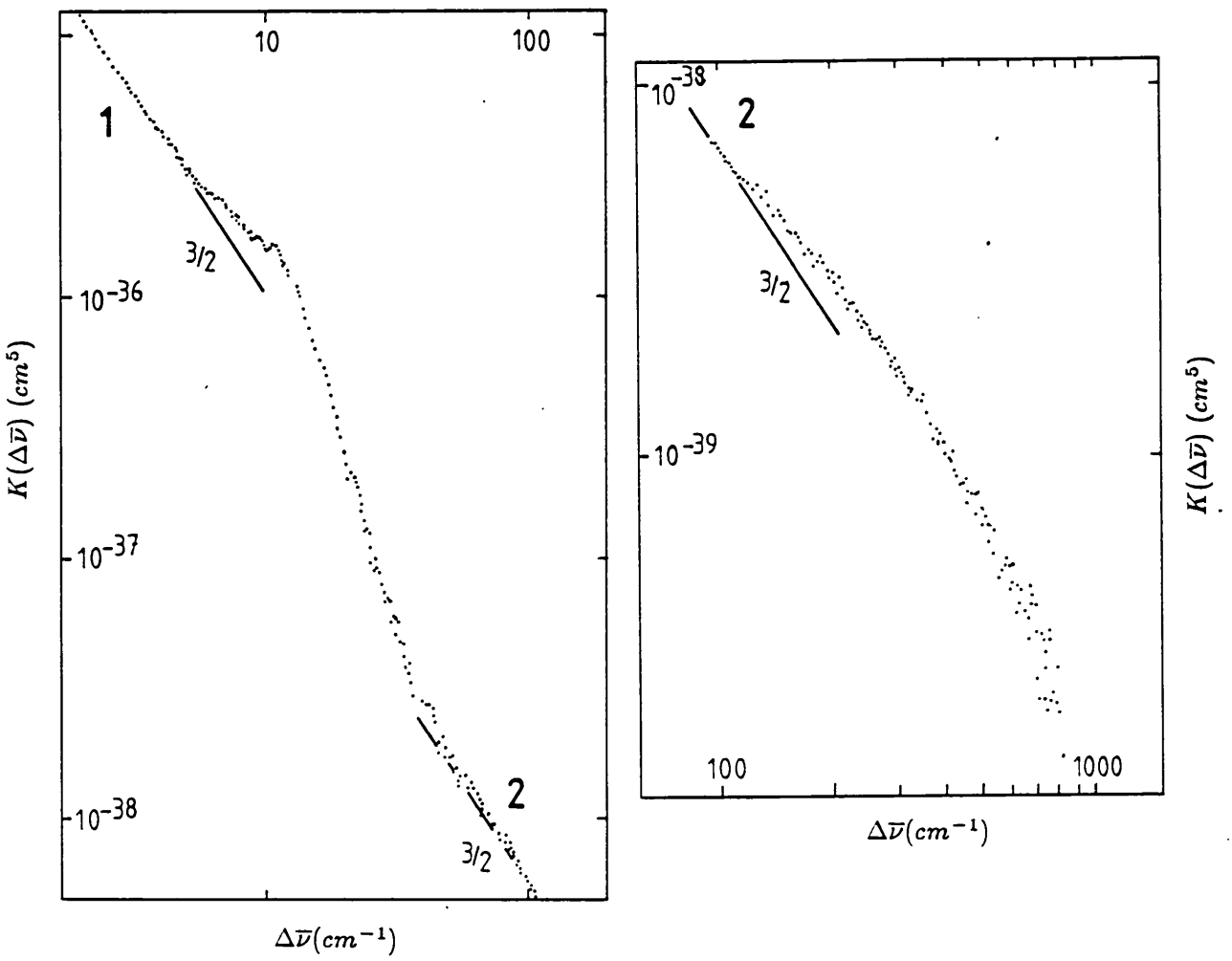


Figure 3.6 Reduced absorption coefficient for the red wing of the Hg 2537 Å line in the presence of 1.9 $\times 10^{19} at/cm^3$ of Kr. (From Grycuk & Czerwosz (1981))

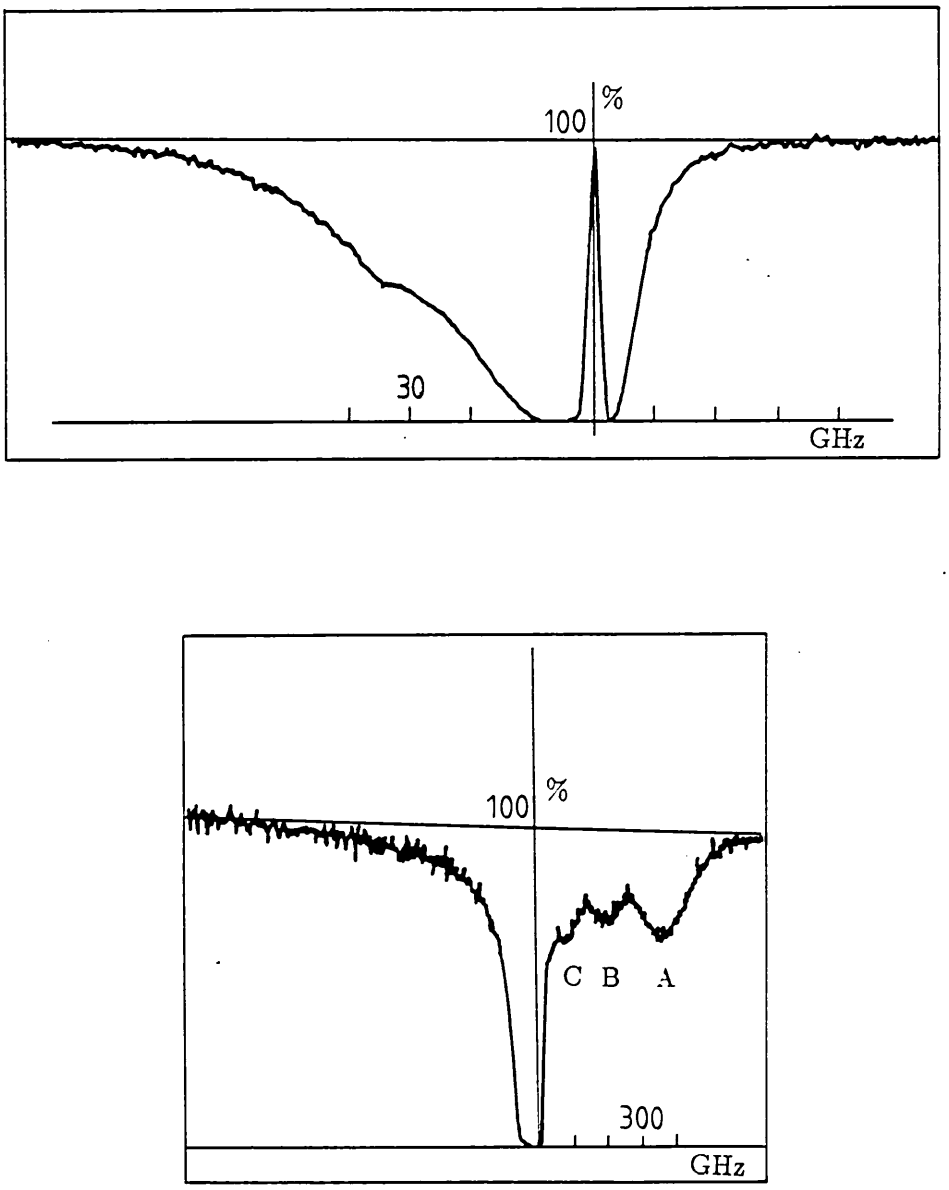


Figure 3.7 **Transmission of a cell containing a mixture of Hg and Kr.** (a) $N_{Kr} = 1.31 \times 10^{19} at/cm^3$, $N_{Hg} = 1.62 \times 10^{15} at/cm^3$ (b) $N_{Kr} = 6.58 \times 10^{18} at/cm^3$, $N_{Hg} = 3.49 \times 10^{16} at/cm^3$. (From Ben Lakhdar *et al.* (1976))

& Czerwosz were unable to perform a temperature dependent experiment of sufficient accuracy in the red wing due to the deformation of the lineshape arising from Hg-Hg interactions. In the blue wing however the profile could be attributed to pure Hg- RG interactions and a temperature dependent experiment was carried out. The experiment allowed a section of the ground state potential, around the point where $V_g = 0$ to be elucidated. They were able to make an estimate of the ground state well depth through this method.

They arrived at their reported ground state potential by fitting their data and some data available from the literature to a modified form of the Maitland-Smith potential. The literature input included atomic beam scattering data from Powers and Cross (1972) and a theoretical C_6 coefficient calculated by Ben Lakhdar *et.al.* (1978). The Powers and Cross data came from measurements of the integral cross section and covered the region of R between 3.6Å and 3.0Å.

Fuke *et al.* arrived at a value for r_m through the application of Kong's rule to literature data on Hg-Hg and Kr-Kr interactions. They allowed the α parameter of the Maitland-Smith potential to vary as well as the β parameter and found the best fit to all the input data for $\alpha = 11$ and $\beta = 18$. The resulting potential curve is shown in figure 3.8 along with their excited state curves which are the subject of the following section.

3.3.3c Excited State Potentials.

ΔV_0 was found by integrating $k_n(\Delta\nu, T \rightarrow \infty)$ as described in § 3.3.3a. Strictly this could only be done for interatomic separations between 2.9 and 4.2 Å where $r(\Delta\nu)$ is single valued. At larger r the red wing is formed by the $X^1 0^+ - B^3 1$ transition as well as the $X^1 0^+ - A^3 0^+$ transition. They attempted to push the procedure to larger r by extrapolating the straight line portion of the profile apparent between 70 and $120 cm^{-1}$ (see figure 3.6) down to smaller $\Delta\nu$. They assumed that the extrapolated line represented the contribution of the $X^1 0^+ - A^3 0^+$ transition alone.

Normally one would interpret a slope of 3/2 on a lineshape plot as the hallmark of a van der Waals interaction and calculate a C_6 coefficient accordingly. Grycuk & Czerwosz point out that, whilst this seems to be a valid procedure for

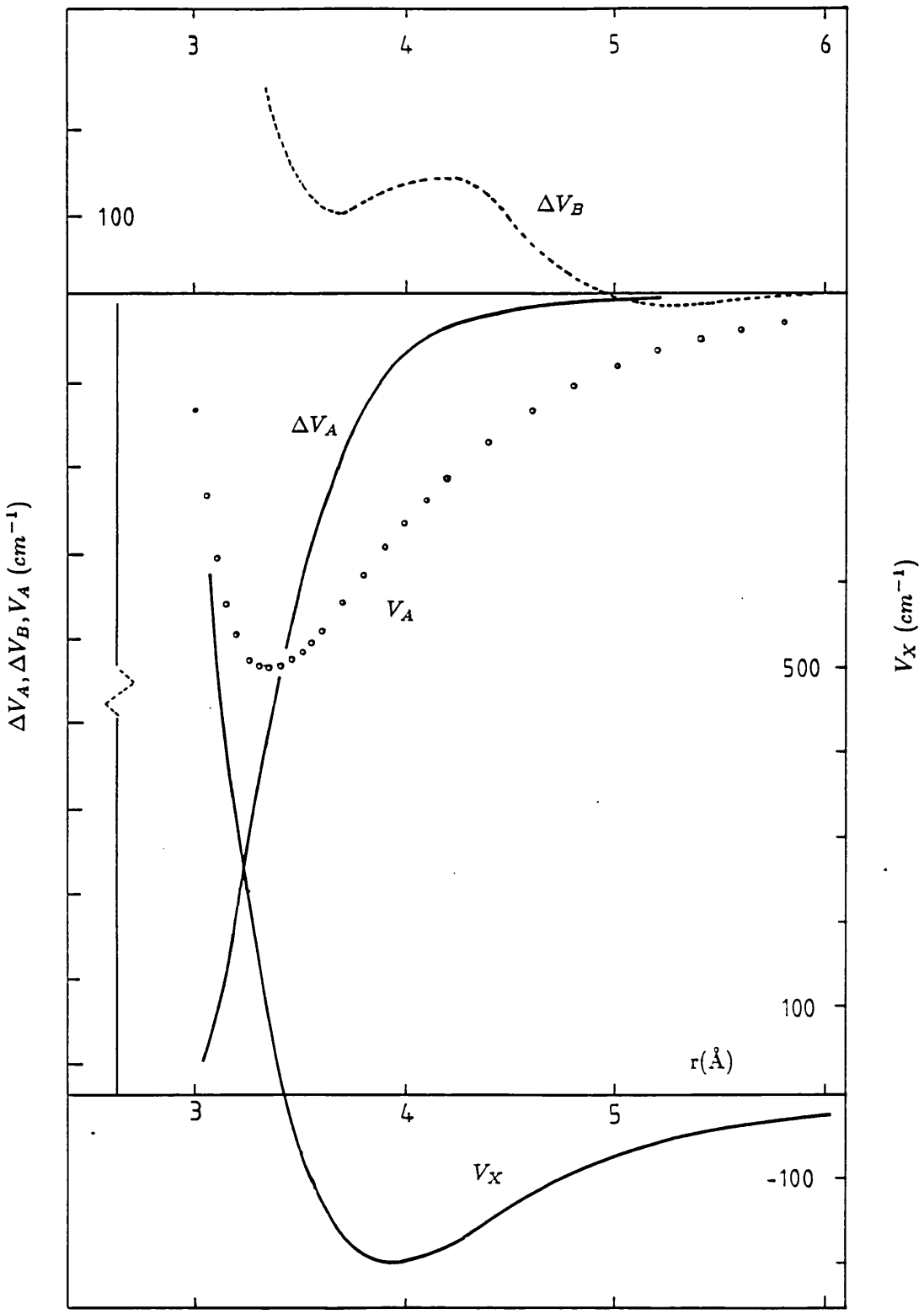


Figure 3.8 $Hg(^3P_1—^1S_0)$–Kr ground and excited state potentials after Grycuk & Czerwosz (1981).

the linear region marked 1 on figure 3.6 it is not valid for the region marked 2. They suggest that the 3/2 slope in region 2 does not reflect a r^{-6} dependence of $\Delta V(r)$ but that it arises from an incidental combination of competing influences ie. the Boltzmann factor and the higher order attractive terms in the difference potential. Their final potential for the $A^3 0^+$ state is shown in figure 3.8.

Only a small section of the $B^3 1$ potential, in the region of $V_g = 0$ was accessible to the direct data inversion method. The long range part of the potential was characterized by assuming a van der Waals interaction and finding a C_6 coefficient from the linear portion 1 (see figure 3.6). For convenience they assumed a Lennard-Jones form for the difference potential and the well depth was estimated by adjusting the position of the satellite predicted by the unified Franck-Condon lineshape to the one observed in the red wing spectrum. The well depth was found to be to be $12cm^{-1}$.

They then connected the two characterized portions (represented by full lines on figure 3.8) with a proposed interpolation (dashed line) which could account for the blue satellites. According to their proposals the maximum and the minimum would be responsible for the satellites A and B respectively. They point out that in this region contributions resulting from bound-free transitions should be small since such transitions would have to originate from the lowest levels of the ground state potential. The population of these states should be negligible in the temperature range covered. On the other hand bound-free transitions from the highest bound and quasi-bound states of V_g could play a significant role. They suggest that satellite C results from such bound-free transitions.

3.4 Summary ; Proposed Potentials for Hg-Kr.

3.4.1 Ground State.

Fuke *et.al.* were only able to make a limited estimate of the ground state potential curve since, having been unable to perform a dispersed fluorescence experiment in Hg-Kr, their quoted Morse potential is based on the analysis of only two hot bands.

Grycuk & Czerwosz were able to elucidate a small portion of the ground state potential, which fortuitously included the region of the potential minimum, by a direct data inversion method. They fitted their data at intermediate r as well as literature data at short and long range to a Maitland-Smith potential and are confident that their proposed potential is correct to within 10% over the entire range of r of interest.

Fuke *et.al.* comment that their results for the ground state agree within experimental error with the conclusions of Grycuk & Czerwosz implying that they consider their determination of the ground state to be inferior to the latter. We therefore propose to accept the results of Fuke *et.al.* as a corroboration of the Grycuk & Czerwosz potential and use the latter forthwith.

3.4.2. Excited State $A^3 0^+$.

Grycuk & Czerwosz were able to elucidate the potential for the A state by application of the direct data inversion technique between $r = 2.9$Å and $4,2$Å . They extended their curve to larger r by making the assumption that they could separate out from the lineshape the portion due to this curve alone, in a region where excitation could occur to both the A and B states. They do not give an analytical form for their A state potential, which is at present only available in graphical form.

Fuke *et.al.* were able to observe very clear spectra for the transitions to the A state occurring at roughly similar regions of r (ie up to $\sim$ 4.2 Å . Unfortunately their data show significant deviations from their suggested Morse potential for the higher lying vibrational transitions. Furthermore, as a result of poor Franck-Condon overlap, no spectral features were discernible from transitions to vibrational levels near the dissociation limit for this potential. A Birge-Sponer plot fitted to the six lowest lying vibrational levels of the well that form a straight line cannot be expected to provide a good estimate of the well depth.

We therefore propose to accept the Grycuk & Czerwosz potential despite the approximation involved in the extension to r values larger than 4.2 Å.

3.4.3. Excited State $B^3 1$.

Grycuk & Czerwosz were unable to map this state directly except for a small portion in a region of only secondary importance to the present studies. In the region of the minimum in the difference potential for this state they fitted the unrealistic Lennard-Jones potential to the shape of the satellite predicted by the unified Franck-Condon lineshape formula.

On the other hand Fuke *et.al.* were able to make an excellent characterization of this potential. The Franck-Condon factors were such that vibrational levels very near to the dissociation limit were discernible. Furthermore the agreement between their proposed Morse potential and their RKR analysis suggests that the Morse function gives a good account of the interaction. With levels near to the dissociation limit resolved the Birge-Sponer plot can be expected to give a reasonable estimate of the well depth.

It is proposed therefore to accept the Morse potential suggested by Fuke *et.al.* for the B state. It may be noted here however that they did not perform the improved extrapolation procedure put forward by LeRoy. Their estimate of the well depth may therefore be slightly shallower than the true value.

3.4.4. Resulting Potentials.

We have proposed to use potentials from two different sources. We are however primarily interested (from the point of view of the calculations based on the molecular model) in the *difference* potentials . Care must be taken therefore to check that the difference between the Grycuk & Czerwosz ground state potential and the Fuke *et al.* excited B state potential is sensible. Taking the potentials as they stand gives a B state difference potential with a well depth of only $\sim 2cm^{-1}$. This is obviously not commensurate with the appearance of the red wing satellite at $\sim 12cm^{-1}$.

The answer lies in the way in which Fuke *et al.* calculated r_m for their B state. They did this by using a simulated FCF programme to calculate the *difference* between r_m for the ground and excited states. However, since their application of Kong's rule was based on their own ground state well depth and

not that of Grycuk & Czerwosz, they also find r_m for the ground state to differ from the value given by Grycuk & Czerwosz. Since it was $r_{m_B} - r_{m_X} = 0.5$Å that Fuke *et al.* calculated and since we propose to use the Grycuk & Czerwosz ground state we must take $r_{m_B} = 3.95 + 0.5 = 4.45$Å. With this change made, the B state difference potential displays a well with a depth of $11.5cm^{-1}$ in good agreement with the position of the satellite. An even better solution would be to re–run the Fuke *et al.* FCF code using the Grycuk & Czerwosz ground state potential.

The potentials to be used are summarized in table 3.2 and are shown in figures 3.9 and 3.10. It should be borne in mind that the entire ground state and the portion of the A state extending from 4.2 Å to higher r are the areas where the potentials are least well characterized.

Table 3.2.

State.	$\epsilon(cm^{-1})$	$\omega_e(cm^{-1})$	$\omega_e x_e(cm^{-1})$	r_m(Å)	α	β	Form.
$X^1 0^+$	200			3.95	11	18	M.S.
$A^3 0^+$	438.1			3.35	7.84	4.11	M.S.
$B^3 1$	96	11.3	0.32	4.45			Morse.

Summary of potentials to be used in chapter 6. Note : The data of Grycuk & Czerwosz were taken for the $A^3 0^+$ state. For convenience of manipulation during the calculations performed in chapter 6 a Maitland–Smith function was fitted to this data (see §6.3.3).

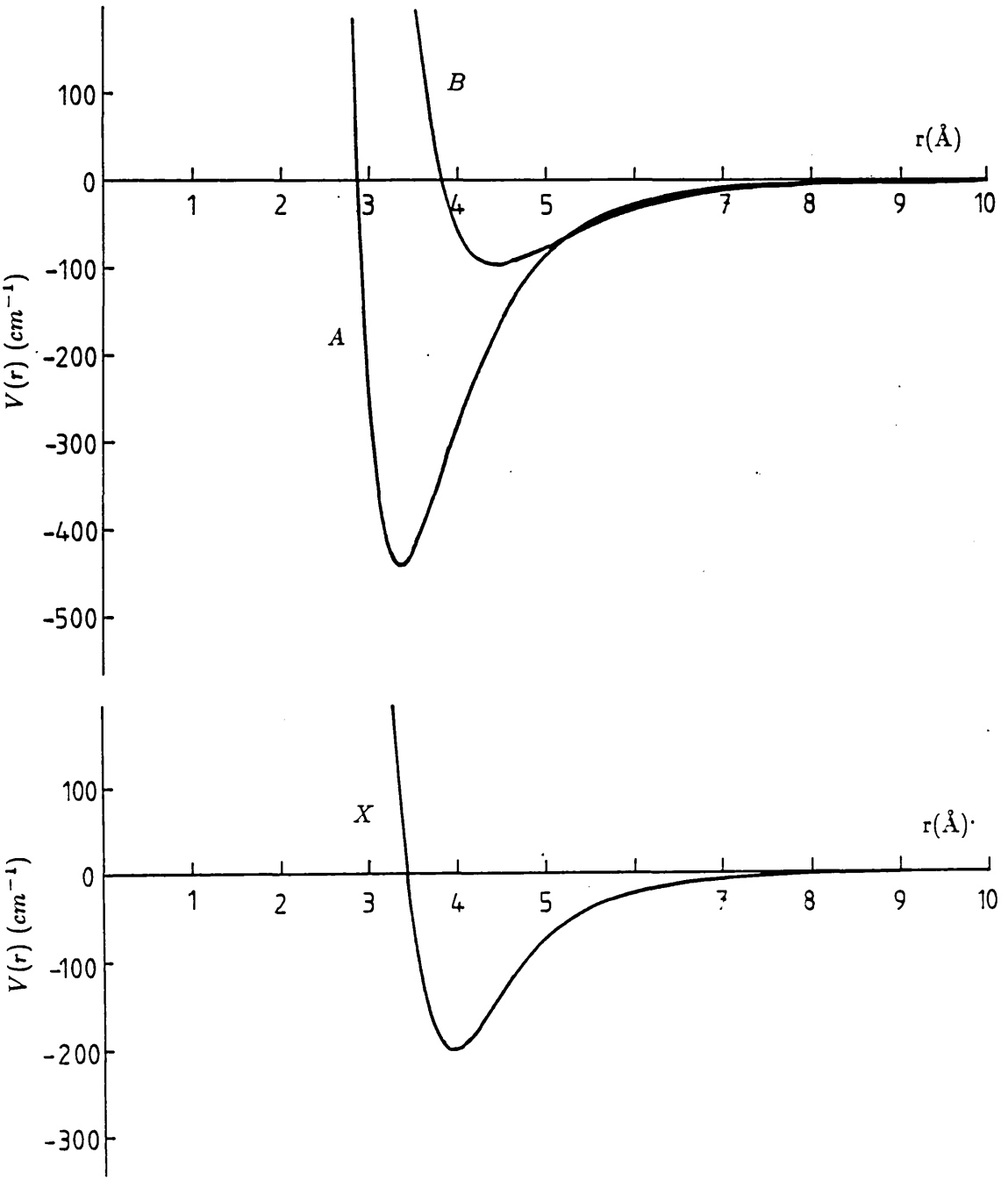


Figure 3.9 Potentials to be used in molecular model calculations. Composite potentials based on the data of Fuke *et al.* (1984) and Grycuk & Czerwosz (1981).

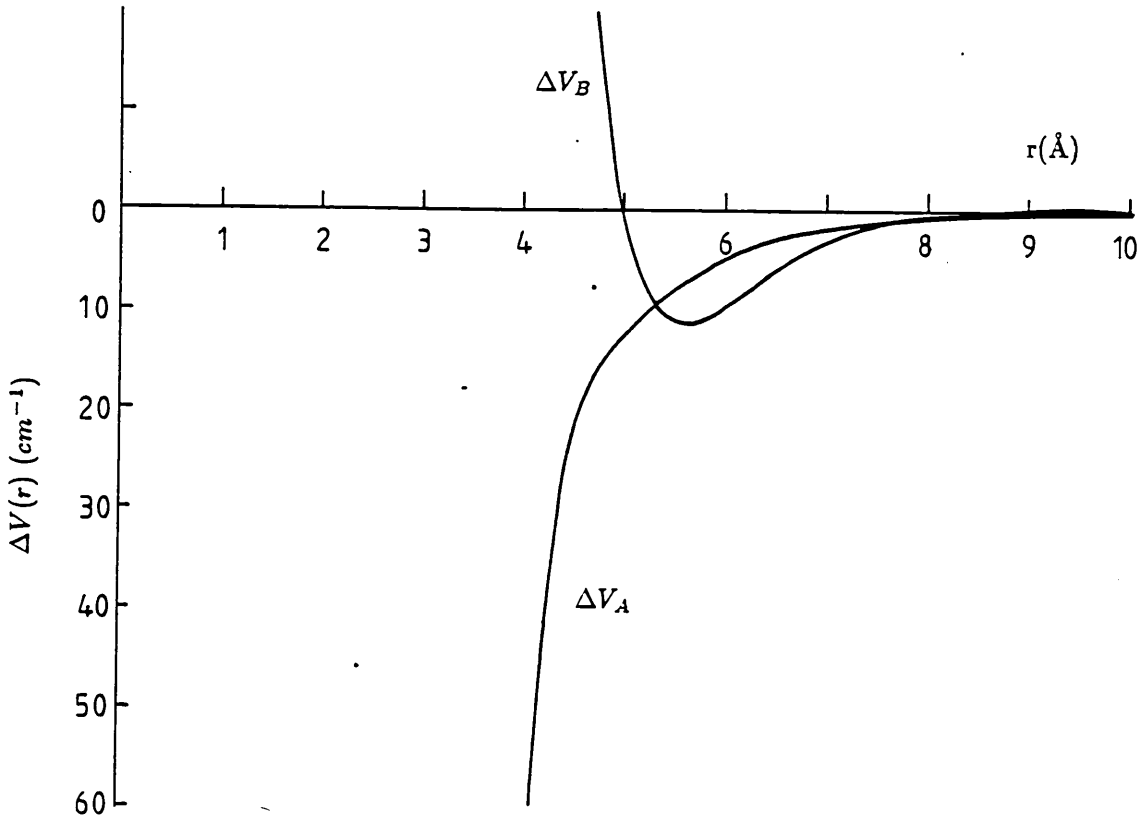


Figure 3.10 Difference potentials based on the potentials of figure 3.9.

Chapter 4.

Experimental Apparatus and Method.

4.1 Introduction

The chapter starts with an outline of the experimental setup (§4.2). The detailed discussion of the apparatus is then split up into three sections covering the lasers and optics (§4.3), experimental cells (§4.4) and data acquisition and control (§4.5) respectively. The chapter concludes with a comparison between the expected experimental signal level and that actually observed (§4.6). In reading this chapter the experiment which we were intent on performing should be borne in mind *ie.* to measure the polarization of the collisionally redistributed light as a function of detuning from line–centre.

4.2 Overview of the Apparatus

The experimental apparatus is shown in figure 4.1. Tunable ultra–violet light at wavelengths close to the Hg 2537Å line was generated by frequency doubling in a lithium formate monohydride (LFM) crystal the output of a home made pulsed dye laser system operating with coumarin 500. The dye laser was pumped with the third harmonic of a commercial pulsed YAG laser with a repetition rate of 10 Hz. The ultra–violet light was focused to a tight spot in the experimental cell using lenses L1 (f=68.5cm) and L2 (f=18cm). Before entering the cell the polarized light was passed through a $\lambda/2$ plate used as a polarization rotator, and then through a heated cell containing Hg vapour. This cell acted as a filter against extraneous line centre light present in the laser wing and will be discussed in more detail later. The main cell was operated at room temperature and could be pumped down to $4 \times 10^{-4} mBar$. The cell was connected to a gas handling system for the admission of Hg vapour and rare gas.

The polarization of the input light was alternated between horizontal and vertical every fifty laser shots by rotation of the $\lambda/2$ plate. The collisionally redistributed fluorescence was detected at 90° to the input beam and was analysed by a vertical, fixed, Glan–air polarizer. The light then passed through

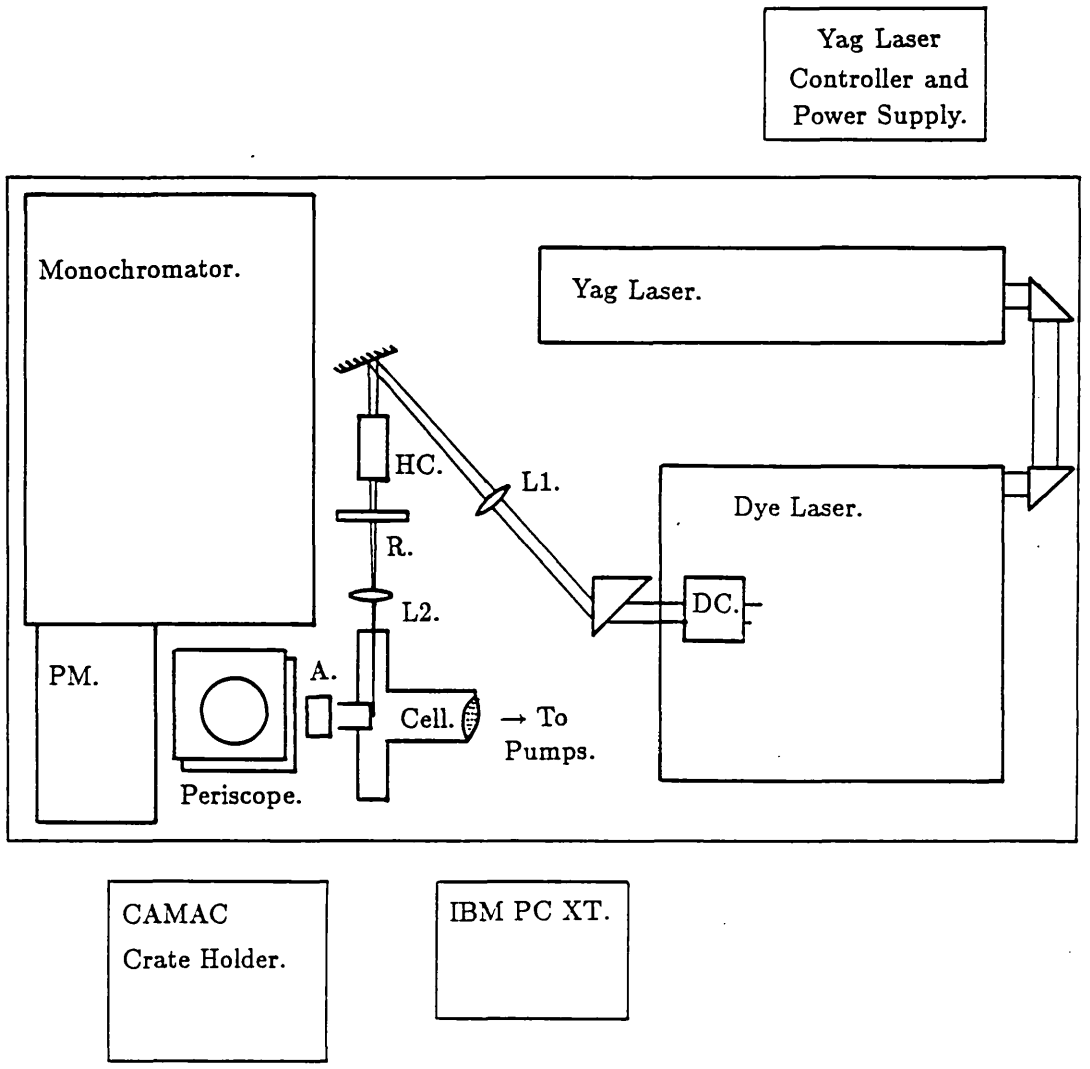


Figure 4.1 Experimental layout.

HC.	Hot cell
R	Polarisation Rotator
DC.	Doubling Crystal
A	Analyser
PM	Photomultiplier.

a periscope equipped with a lens (f=13.5cm) to reach the entrance slit of the monochromator. The monochromator was tuned to 2537Å and acted as a filter against the main source of background ie. scattered, non-resonant laser light.

A photomultiplier (PM) was positioned at the exit slit of the monochromator. When the signal was lower than one photon per laser shot the output of the PM was fed to a photomultiplier amplifier linked to a discriminating amplifier and a scaler. When signals were higher than this the output of the PM was fed directly to an analogue to digital converter (ADC) acting as a charge integrator. The scaler and ADC were gated using a pulse delay generator (PDG) which was also used to fire the laser.

The PM high voltage power supply, ADC, PDG and scaler were housed in a CAMAC crate while the PM amplifier and the discriminator were housed in a NIM rack. The experiment was controlled and the data collected by an IBM PC XT via a Transiac CAMAC crate controller.

4.3 Lasers and Optics

4.3.1 Pump Laser.

The pump laser was a JK Hyperyag 750, oscillator–amplifier setup producing 800mJ per pulse at 1064nm. The oscillator is Q–Switched to produce high intensity 8ns (FWHM) pulses. This output is frequency doubled to 532nm in a CD^*A Type I crystal with an efficiency of 44% . The 532nm light is sum–frequency mixed with the remaining fundamental beam in a KD^*P type II crystal to produce 180mJ of 355nm light. Ancillary to the laser are its power supply and control unit.

Q–Switching is via a Pöckels cell crossed with a pile of plates polarizer. The Pöckels cell can be triggered either internally or externally. For synchronization purposes the control unit gives out a 150μs rectangular pulse (sync.) at the time that the flashlamps fire.

A delay between the firing of the flashlamps and the triggering of the Pöckels cell allows the population inversion to build up to a large value before the initiation of laser action. This delay has an optimum value at which the

energy of the Q–Switched pulse is maximized. If the delay is too *long* however, laser action can be initiated before the Pöckels cell is triggered. This process is known as prelasing.

A delay of 40μs between the falling edge of the sync. pulse and the firing of the Pöckels cell was found to be optimal. The internal timing circuit was rather crude giving a jitter of more than 1μs on this delay time. Since data collection gates of 250ns were to be used it was decided to trigger the Pöckels cell externally. To this end the sync. pulse was fed into the PDG (see § 4.5.3) which provided a trigger pulse with the correct 40μs delay and sub–nanosecond jitter. The data collection gate could then be set accurately with respect to the initiation of the laser pulse.

The failure of two inexpensive but essential (and elusive) electronic components in the laser control unit and the power supply (a high voltage diode and a high voltage capacitor) marred the otherwise good performance of the laser. After prolonged use the doubling and mixing crystals showed signs of optical damage and the output fell below the specifications. Towards the end of the experiment only $\sim$ 135mJ of 355nm pump light was available.

4.3.2 Dye Laser: General.

A high power oscillator–amplifier pulsed dye laser system was constructed around an existing oscillator, based on a design put forward by Shoshan *et al.* (1977) and by Littman and Metcalf (1978). The oscillator had been used in previous experiments in the Blackett Laboratory and is described in detail by Kent (1985). Particulars of the dye laser system, shown schematically in figure 4.2, will be discussed in the following sections.

4.3.3 Oscillator.

The oscillator is pumped with 2mJ of 355nm light split off from the main beam using a quartz flat. The design is very simple, comprising only four elements: two 100% reflecting mirrors, a dye cell and a 1200 line/mm holographic grating. The more usual Hänsch design (Hänsch 1972) requires an intracavity beam

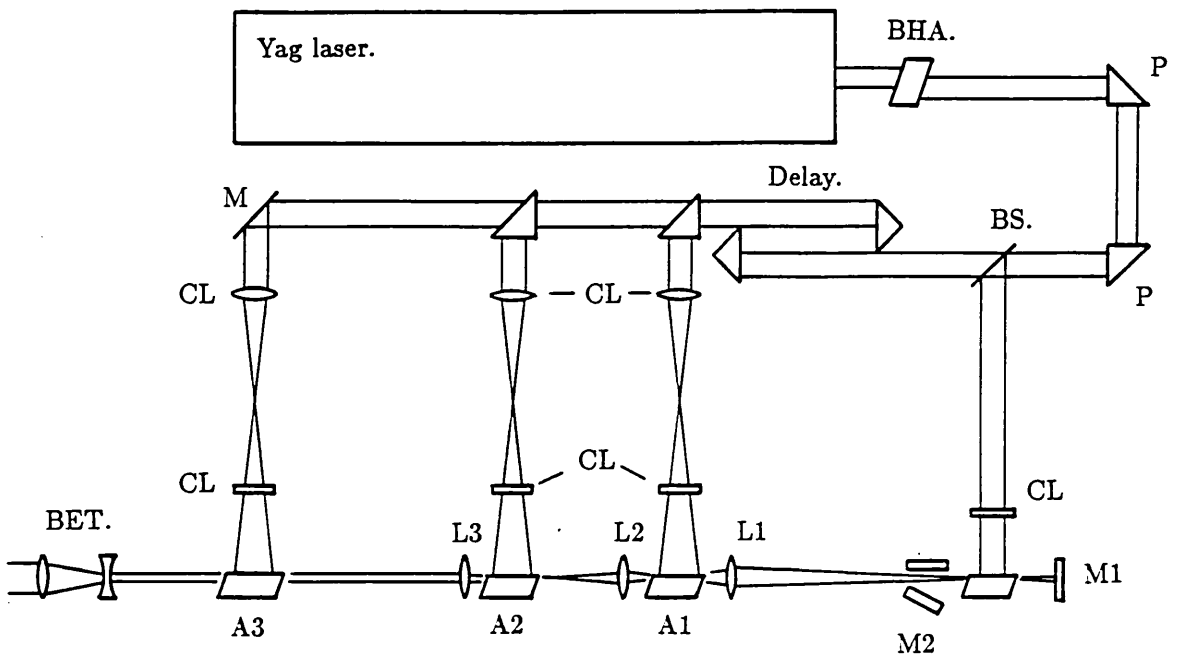


Figure 4.2 Laser System.

BHA	Beam Height Adjuster
P	Prism
BET	Beam Expanding Telescope
CL	Cylindrical Lens
M	Mirror
BS	Beam Splitter.

expanding telescope to ensure that as many lines of the Littrow mounted grating are used as possible. In the Littman design the grating is used at grazing incidence allowing the full width to be illuminated. The low efficiency of the grating ($\sim$ 5%) makes this design dependent on a high gain laser medium. 95% of the light is specularly reflected at the grating and is taken as the output.

The oscillator had previously been used at a low repetition rate (2 pulses per minute) and it had not been necessary to flow the dye. The dye cell was therefore replaced with a flow–through type (see § 4.3.4) for our experiment.

The oscillator operates in 10-15 longditudinal modes which, with a mode separation of 1.25GHz gives a bandwidth of approximately 10Ghz FWHM. The Littman design can be made to operate in as few as 2–3 modes however mode competition can lead to amplitude instability in this configuration. Since narrow bandwidth was not an overriding concern in our experiments the larger number of modes was preferable. The shot to shot fluctuations in energy were measured to be less than 15% .

The oscillator is tuned by rotation of the mirror M2. The variation of λ with tuning angle ϕ is given by

$$\lambda_{Laser} = (x/m)(\sin\theta_0 + \sin\phi) \tag{4.1}$$

Where

x = Groove spacing = $8.33 \times 10^{-4} mm$

θ_0 = (Angle between grating and laser axis)

= 89°

m = diffraction order

ϕ = angle between grating and mirror.

The mirror M2 is pivoted at one end and is rotated by adjustment of a micrometer which bears on the other end of its mount. This arrangement gives $\sin\phi = y/b$ where y is the distance moved by the micrometer and b is the distance between the pivot and the micrometer. Wavelength is therefore linear with micrometer setting. The dye laser was calibrated using an Edinburgh Instruments pulsed wave meter (see figure 4.3).

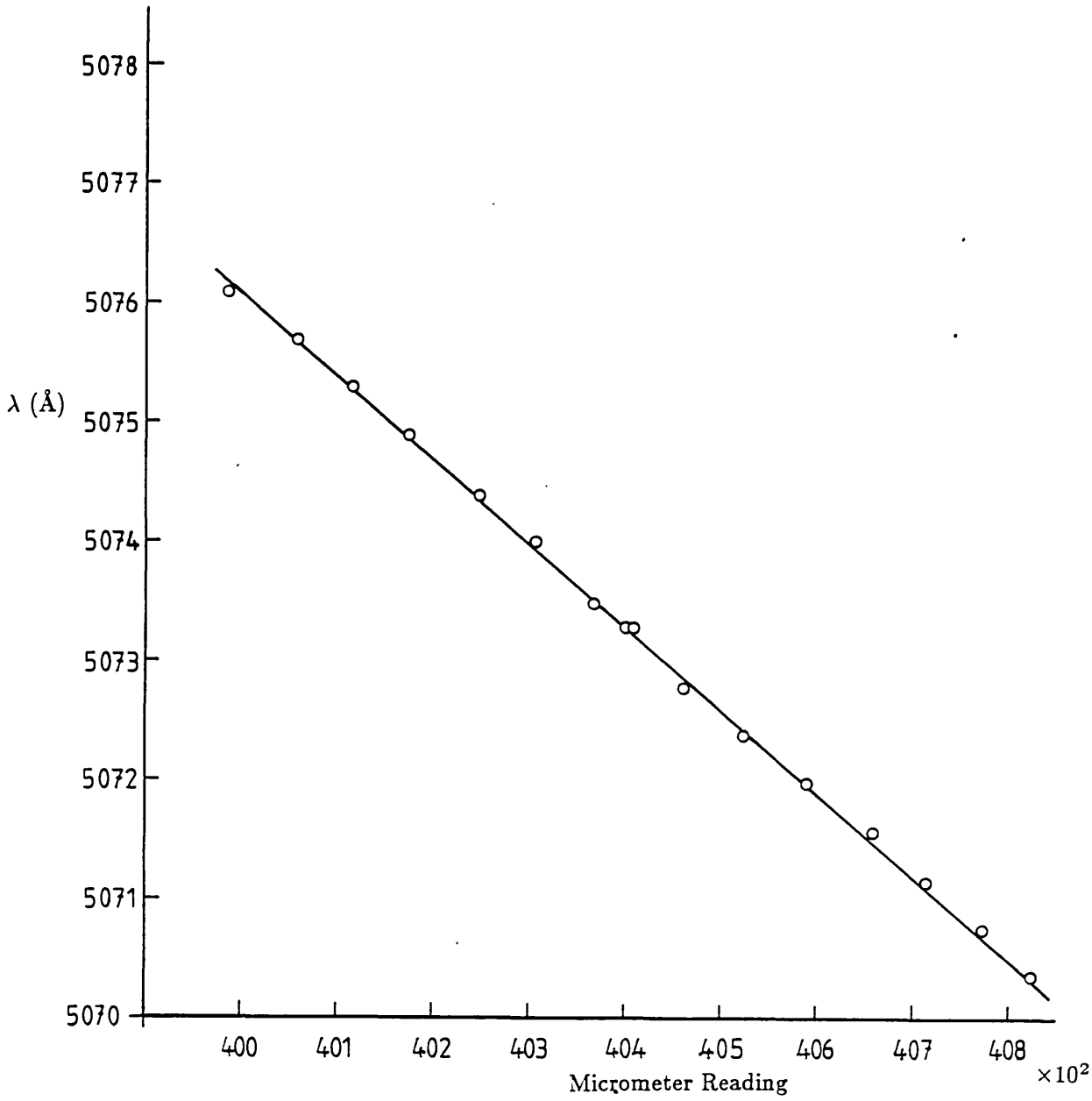


Figure 4.3 Dye laser calibration curve. The linearity of the dye laser tuning was checked using an Edinburgh Instruments pulsed wave meter. The accuracy of the wave meter is ±0.1 Å . The radius of the circles reflects this accuracy. The dye laser was tuned by actuating a Micrometer to pivot mirror M2 of figure 4.2.

4.3.4 Amplifier Chain

The oscillator output is amplified in a three stage transversely pumped amplifier chain similar to that reported by Wallenstein and Zacharias (1980). A delay of 3ns is allowed between the pumping of the oscillator and that of the amplifier chain, ensuring that dye laser output is present in the amplifiers by the time they are pumped. This inhibits the production of amplified spontaneous emission (ASE) at the amplifier stage.

The remaining pump beam is devided up amongst the amplifiers with 5% going to A1, 20% going to A2 and the remainder to A3. Beam splitting to the first two stages is achieved by vertically positioning a Brewster angled prism to select the required amount from the bottom of the beam. The final stage is equipped with a 100% reflecting, dielectrically coated mirror.

Standard flow through spectrophotometer cuvettes, often used as dye laser amplifiers, were found to give poor beam quality and output power when pumped at a repetition rate of 10Hz. Consequently, home made cells capable of giving fast flow through the active region were used. These cells consist of stainless steel bodies with fused silica front and side windows glued on. The gap between the front window and the stainless steel body is 1mm for A3 and .5mm for A1, A2 and the oscillator cell. The side windows are tilted at 10° to prevent optical feedback.

The oscillator output is focused *through* the first amplifier to a spot just beyond it, using lens L1 (figure 4.2 f=7.5cm). The amplified light is focused into A2 using lens L2 (f=4cm). After A2 the beam is collimated using lens L3 (f=4cm). The spot reaching the final amplifier is about 0.7mm in diameter. After the final amplifier the light enters a $\times 10$ magnification beam expanding telescope before entering the frequency doubling crystal.

The entire system is laid out on an optical table using Oriel rail. Dye circulation units consisting of a Micropump gear pump, a reservoir and a Millipore filter are positioned beneath the table. The dye solvent is methanol and the concentration is different in the various cells. The concentration in the oscillator dye cell is 1g/l. Amplifiers A1 and A2 share a circulation system flowing

a 0.5g/l solution. The final amplifier has a solution of 0.25g/l. The dye concentration decreases along the amplifier chain to allow deeper penetration of the pump light into the dye. The larger pumped volume coincides with the expanding beam size along the chain.

4.3.5. Dye Laser Performance.

The dye laser output power was measured to be 9.7mJ using a Scientech Joule meter. The total pump power available was 180 mJ, however losses in the beam height adjuster (BHA) and in the beam steering prisms were such that only 130mJ remained at the oscillator beam splitter. The prisms, cylindrical lenses and dye cell windows were not antireflection coated leading to considerable losses of pump power. Wallenstein and Zacharias (1980) claim an output of 16mJ for a pump energy of 120mJ using coumarin 485 at λ=500nm. In the light of this and considering the losses inherent in the present system 9.7mJ is a reasonable output.

The final output beam is elliptical in shape measuring approximately 0.7mm $\times$ 0.4mm. Diffraction causes weak subsidiary maxima to be present to one side of the main beam. The beam profile is very smooth with little shot to shot variation allowing efficient, stable second harmonic generation (SHG).

4.3.6 Frequency Doubler.

The output of the dye laser system was frequency doubled in a Lithium Formate Monohydride (LFM) type I crystal supplied by Quantum Technology through JK Lasers. The $10mm \times 8mm \times 8mm$ crystal is mounted in a metal cell filled with index matching fluid. The end windows of the cell are antireflection coated at the wavelengths of interest. Type 1 refers to the phase matching scheme employed in which two beams of the same polarization interact to produce an orthogonally polarized frequency doubled beam.

The efficiency of the crystal was measured to be 0.75—1.25 % . The input energy was measured using a Scientech Joule meter and that of the doubled output with a pyroelectric detector. This efficiency is less than the 2% reported

by Dunning *et al.* (1973) however these authors made no comment on the crystals susceptibility to damage in prolonged use. The damage threshold quoted by the supplier is $20MWcm^{-2}$ and the beam expander ensured that this value was not exceeded during the experiment.

Earlier tests at higher power densities produced damage after a few hundred shots. Even at power densities lower than $20MWcm^{-2}$ the crystal eventually showed slight damage though this did not seriously affect the efficiency.

Since the experimental signal level was rather low other frequency doubling crystals capable of higher efficiencies were considered. A Urea crystal was obtained from Quantum Technology but was of rather poor optical quality. Other sources have reported efficiencies of up to 8% using this crystal to frequency double to 249nm. Unfortunately the efficiency is strongly dependent on wavelength and at 254nm was found to be 1.5–2.0 % . Furthermore, although the single shot damage threshold is high, the crystal is very susceptible to damage in prolonged use. Beam expanding to a power density insufficient to cause multiple shot damage drops the efficiency to well below that attainable with LFM.

Phase matching can be achieved at this wavelength in a refrigerated crystal of Ammonium Dihydrogen Phosphate (ADP) however such a system was unavailable. More recently a new crystal, β–phase Barium Borate, has been discovered. It can be phase matched at 2537Å and has a very high damage threshold and a high efficiency. Such a crystal is presently on order and will be used in the continuation of this work.

4.3.7 Optical System: Layout and Alignment.

The term "optical system" refers to optical components after the frequency doubling crystal, leading to the experimental cell and optical components between the output window of the cell and the photomultiplier (figure 4.1). After the frequency doubler the beam was harmonically separated using a quartz prism. The remaining fundamental light was terminated on a screen. The tunable ultra violet light was passed through lens L1 and then reflected at the mirror. Lens

L2 focused the beam to a spot in the experimental cell. The spot size was measured to be $70\mu m$ in diameter (FWHM) using a $10\mu m$ pinhole on a translation stage and an ultra violet photodiode.

The system was aligned by passing a Helium–Neon (He–Ne) laser beam through the exit window of the cell, in the opposite direction to the ultra violet propagation direction. The He–Ne beam was horizontal and grazed the inset, output window.

A one metre, Czerney–Turner, f/10 monochromator (Monospec) was used as a filter against directly scattered light. It was equipped with an 1800 l/mm grating blazed for 5000Å . It was used in second order and was tuned to the Hg $^3P_1$—$^1S_0$ 2537Å transition. The slits were set at $80\mu m$ during the experiment.

The periscope acted as a height adjuster and optimally imaged the horizontal laser focal region in the cell onto the vertical monochromator entrance slit. The lens was positioned half way between the slit and the object plane, a distance of $2f$ from both. The focal length of the lens at 2537Å was measured using a thermaline Hg lamp and a 2537Å line filter and was found to be 13.5cm, a 10% correction on its quoted focal length of 15cm. A diaphragm was placed at the lens to limit the signal collection to f/10 to match the monochromator. A larger solid angle of detection would also have lead to inaccuracy in the measured polarization.

The signal collection optical path was also aligned using a He–Ne laser. The monochromator was tuned to 632.8nm and the He–Ne beam sent *into* the monochromator through the *exit* slit ensuring that the beam was centrally positioned on the slit. The laser mount was adjusted so that the beam hit the output mirror of the monochromator centrally. Adjustment of the grating only, then ensured that the beam passed correctly through the monochromator and exited the entrance slit centrally.

The periscope lens was removed and the periscope mirrors adjusted so that the He–Ne beam hit the centre of the output window of the experimental cell. At the same time it was ensured that the portion of the beam between the lower periscope mirror and the cell window was horizontal and orthogonal to the ultra violet laser beam axis. The periscope lens was then replaced and its position

adjusted until the He–Ne beam again formed a spot at the centre of the cell window.

4.3.8 Polarization Rotator

Fluorescence polarization measurements were made by alternating the polarization of the input light between vertical and horizontal and using a fixed vertical polarizer (J.Phillips Optical) as an analyser. This was accomplished by automatic rotation of a $\lambda/2$ plate (B. Halle Nachfl.) in a computer controlled optical mount. The $\lambda/2$ plate was housed in a rotating gearbox unit with a gear ratio of 8:1 linked to a 1.8° per step stepper motor with a resolution of 0.1° via a flexible connector. The motor was activated from the IBM PC via a control unit and a power supply housed in a 19 inch Eurocard rack on the CAMAC crate holder. The control unit could be directly operated from its front panel, bypassing the computer.

The use of a Pöckels cell was unnecessary for this application since rotation could be carried out between laser shots and therefore speed was not a consideration.

4.4 Cells.

4.4.1 Heated Filter Cell.

Preliminary tests showed a very poor signal to background ratio of roughly 1:1. Here signal refers to PM events recorded with Hg and Kr present in the experimental cell and background refers to PM events taken with Hg only in the cell. The background was drastically reduced by removing the Hg from the cell and was therefore attributed to resonantly scattered light from the wings of the laser line. This source of background had been encountered in the continuous wave experiments of Alford *et al.* (1984) but was only found to be appreciable at large detunings ($> 200cm^{-1}$). They circumvented the problem by using prisms to disperse the laser background emission.

Figure 4.4 shows the spectrum of the ultra violet output. This was taken by scattering the ultra violet beam off a card placed in front of the experimental cell window. The monochromator slits were closed down to achieve maximum resolution. The monochromator was then scanned across the laser line. The light level was insufficient to saturate the PM, even when tuned to the centre of the laser line. Since it was necessary to vary the voltage applied to the PM during the course of the test the relative gain of the PM was checked at the voltage levels used. The data were adjusted accordingly.

The result shows a laser peak with the expected FWHM superimposed on a plateau of ASE extending out beyond $100cm^{-1}$. Broadband amplified spontaneous emission is a much more severe problem in pulsed dye laser systems than in continuous wave systems. Rather than attempting to disperse the ASE, a different solution was sought. The ultra violet light was passed through a cell containing Hg only, before reaching the experimental cell. Any resonant component in the laser emission has a strong probability of exciting a Hg atom in this cell. The Hg atom thus excited radiates isotropically, effectively removing the unwanted photon from the beam.

The cell is a fused silica tube with Brewster angled windows at either end and a small dip in the centre holding a drop of Hg. It is wrapped with nichrome heater wire attached to a variable voltage power supply and then with fibreglass heat resistant sheathing acting as insulation. A thermocouple is attached to the cell to monitor its temperature.

The minimum detuning from line centre used in the experiment was $5cm^{-1}$. The cell was operated at 95°C. Operation at higher temperatures increases the opacity to a level that causes attenuation of the laser beam at the minimum detuning.

4.4.2 Experimental Cell,

The experimental cell is a fused silica cross with an inset, output window. The windows were optically contacted to the ends of the 1.3cm internal diameter tubes. The cross is connected to a pyrex section via a graded seal. The pyrex

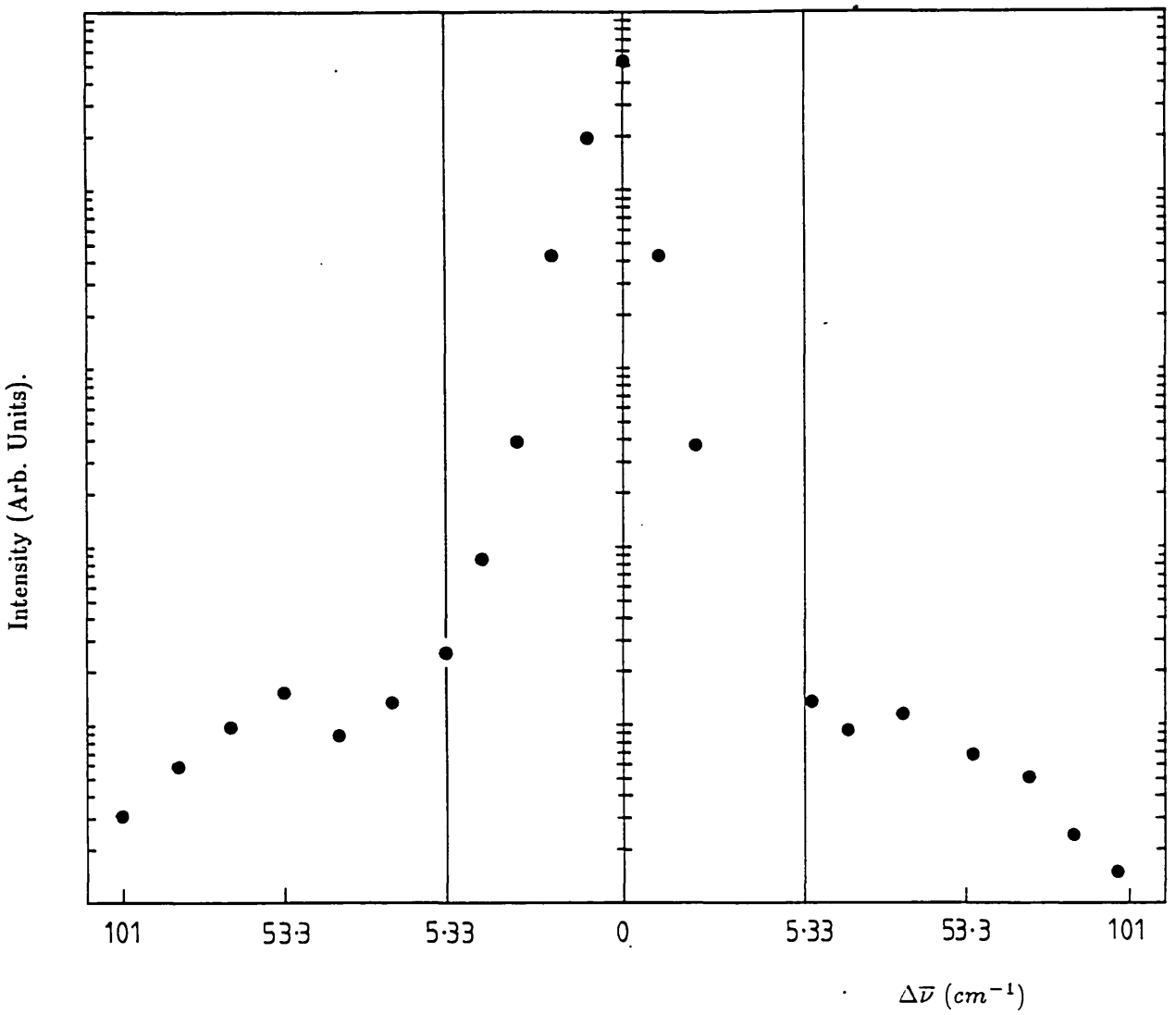


Figure 4.4 Frequency spread of tunable ultra violet output. The vertical scale is logarithmic while the horizontal scale is linear. Note the change of horizontal scale at $\pm 5.33 cm^{-1}$ to show the wide plateau.

section leads to the vacuum pumps and houses the mercury reservoir, the vacuum gauges and the Rare Gas admission valve. The mercury reservoir and the section containing the vacuum gauges can be separately valved off. The gauges are a Pirani (Edwards PR–K), a Penning (Edwards CP–25K) and a miniature McLeod gauge (Edwards vacustat 1) which together cover the range from 10mBar to 10^{-6}mBar.

The cell was connected to a mercury diffusion pump and an Edwards two stage rotary pump. With the vacustat removed and the mercury reservoir valved off the cell was evacuable down to 4×10^{-5}mBar. Closed off from the vacuum pumps the cell leaks up to $\sim$ 1mBar in 12 hours. Unsuccessful attempts were made to find the source of the leak using a helium leak detector. It is thought that the fault lies in the presence of the large number of O ring sealed valves and junctions. A new cell is presently under construction which should overcome this problem and incorporate other desirable features not available with the present cell.

Data collection runs were limited to $\sim$ 1 hour to ensure that any background signal due to collisions with impurity gasses was kept down to a level at which there was a negligible effect on the data.

4.5 Data Acquisition and Control.

4.5.1 Photomultiplier

The photomultiplier used was an RCA C31034 with a gallium arsenide photocathode. It is specifically designed for use at low temperatures in photon counting applications. A Pacific Instruments model 3457 thermoelectric PM housing and a model 33 Power Supply/Temperature Controller unit were used. Dark count is a logarithmic function of temperature, and for this photomultiplier, can be as low as 50cps at $-30°$C. We operated the photomultiplier at 0°C giving a nominal dark count of 1.5×10^{3}cps. The experimental gating time was 250ns giving a nominal count rate due to dark current of 3.75×10^{-4} counts per laser shot. The maximum anode–cathode voltage permissible is 2200V. 2000V

was not exceeded during the experiment. The photomultiplier transit time is 33ns.

4.5.2 CAMAC: General.

CAMAC is an international standard to which manufacturers of sophisticated modular electronics packages comply. Its standards govern the physical size and shape of the plug in modules as well as the protocol through which they communicate with each other and/or a computer. A CAMAC crate is a 19 inch rack comprising 25 stations, each capable of accepting one module. The modules slot into the crate and connect with an 86 pin dataway running along the back of the crate. Station 25 is reserved for the crate controller which is an interface between the CAMAC crate and the computer.

The present system uses a Transiac crate controller which is two stations wide. The crate controller is supplied with software in the form of four machine code subroutines which can be called from basic. Their functions are to clear the dataway, to send commands, to receive data and to ask the controller if there are any data to be collected. Software pertinent to the present setup was written in Basic around these subroutines. The following sections discuss the operation of the CAMAC and other electronics modules used in the experiment.

4.5.3 Pulse Delay Generator (PDG).

The PDG (LeCroy 4222 four channel PDG) was the module responsible for the coordination of the experiment, from the firing of the laser (§ 4.3.1) to the gating of the data collection modules. It is capable of setting four delays in the range 100ns—16.7777215ms in 1ns increments with an accuracy of ± 200ps. The delays can be operated in tandem creating a time window rather that just a simple trigger. The relationship between the PDG and the other modules is shown in figure 4.5.

In the present system one of the channels is used to trigger the Yag laser and two channels were operated in tandem as the data collection gate (figure 4.6). The 200ns delay between the firing of the Pöckels cell and the beginning

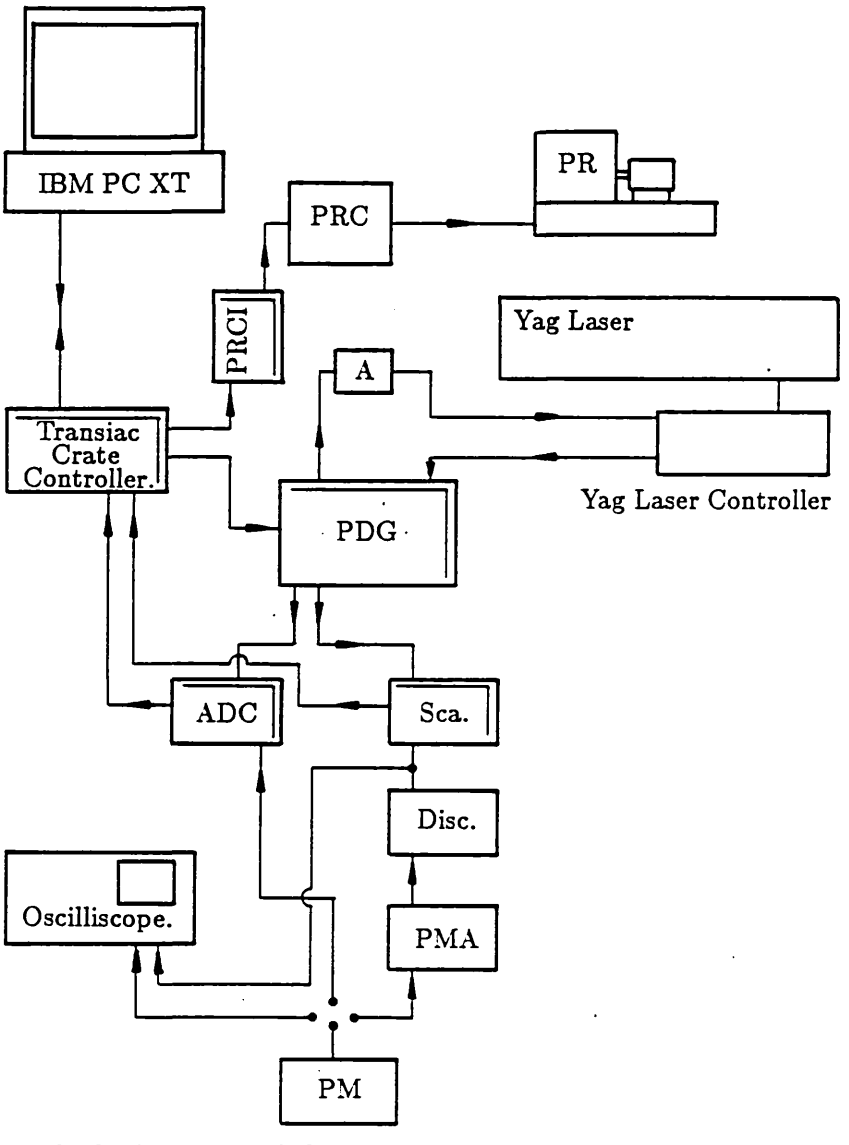


Figure 4.5 Block diagram of data acquisition and experimental control system. Units marked] are CAMAC modules. The PDG is at the centre of the figure to emphasize its importance in controlling the other modules.

PDG	Pulse Delay Generator
PR	Polarisation Rotator
PRC	PR Controller
PRCI	PRC Interface
ADC	Analogue to Digital Converter
PM	Photomultiplier
PMA	PM amplifier
Sca.	Scaler
Disc.	Discriminating amplifier
A	Amplifier

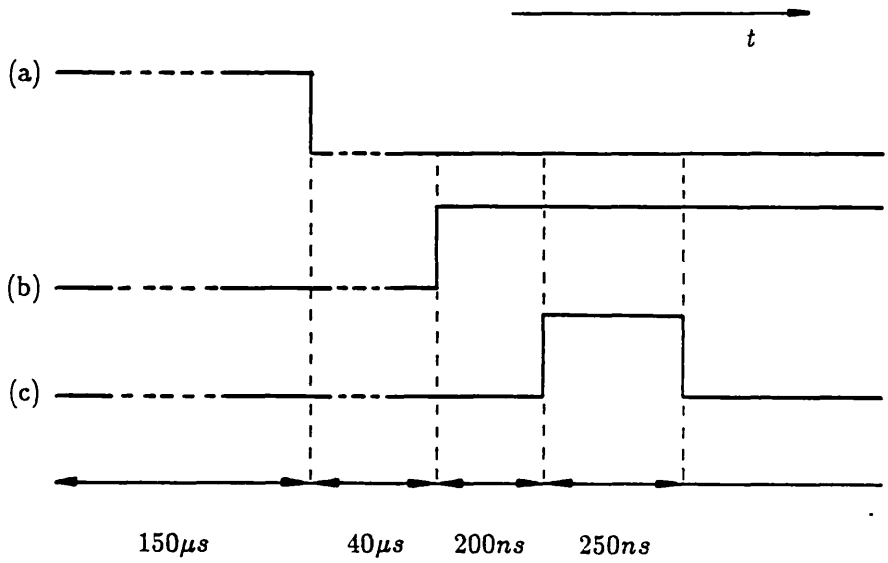


Figure 4.6 Pulse timing. (a) Sync pulse provided by Yag laser controller fed to PDG, (b) Laser Q-Switch trigger pulse sent from PDG, (c) Gating pulse sent from the PDG to either to the ADC, in the case of analogue signal collection or to the Scaler, when operating in photon counting mode.

of the data collection gate includes the time taken for the trigger pulse to travel down ~ 7m of cable and register at the laser control unit, as well as the optical delay between the Yag laser pulse and the monochromator exit slit and the photomultiplier transit time.

4.5.4 Analogue to Digital Converter (ADC).

A LeCroy 2249 12 channel ADC was used. Its input sensitivity is 0.25pC/count with a full scale range of 256pC. The ADC registers ~ 2 counts per detected photon with the PM at 2000V. The ADC registers a value in the absence of input which is dependent on the gate length. This false count is referred to as the pedestal and must be subtracted from the registered value to retrieve the actual signal dependent count.

The pedestal value was found to be 30 with a gate length of 250ns. Unfortunately the pedestal value was not always steady but would, at times, alternate between 30 and 29. When taking data the pedestal was tested for 200 shots before and after an experimental run of 2000 shots. The average pedestal value was computed and subtracted from each of the 2000 registered experimental values. The random error generated by this occasional drift was minimal when signal levels were greater than ~1 photon/shot. At signal levels much lower than this considerable error could be incurred. Photon counting using a scaler was therefore adopted at lower signal levels.

4.5.5 Photon Counting: PM Amplifier, Discriminator and Scaler.

The scaler used was a Le Croy 12 channel 100MHz CAMAC model 2551 with an input threshold of −600mV and a minimum acceptable pulse width of 5ns at > -700mV. The single photon pulses from the photomultiplier (0.5pC in 5ns, ie 5mV through 50 Ω) were unsuitable for direct input into the scaler. They were therefore fed into a photomultiplier amplifier linked to a discriminating amplifier the output of which was sent to the scaler. The scaler was gated using the PDG by inhibiting it except during the time window of interest. A second output from the scaler was fed to an oscilliscope (Schlumberger OCT588A) to allow visual checks on the signal level.

The photomultiplier amplifier was a NIM model 612AM with a maximum gain of 40 and a $<$ 3ns rise time. The discriminator used was a LeCroy quad 100MHz NIM model 821 with an input threshold variable between -30mV and -1000mV. Output pulses were -800mV and 5ns long. The discriminator double pulse resolution was $<$ 9ns.

The Yag laser Pöckels cell was a strong source of radio frequency noise and care had to be taken to shield the photomultiplier amplifier input cable. This was done by sheathing the cable in aluminium foil. The ADC data collection method was not susceptible to this source of noise.

4.6 Signal Level.

4.6.1 Line–centre Signal.

The signal obtained with the experimental cell at room temperature and with the laser tuned to resonance was found to be $\sim 4\times10^3$ photons per shot. Voltage versus time plots of the line centre signal, taken using a Tektronix 7912AD 1GHz transient digitizer, are shown in figure 4.7. The fluctuations seen in (b) and (c), taken at lower laser power, are due to photon statistics. The effect of putting a small bar magnet ~10cm away from the interaction region of the cell is shown in (d). This behaviour is an example of the Hanle effect discussed in the next chapter.

Comparison between this observed signal and a calculated line– centre signal can act as a check on the experimental setup. The expected line–centre signal can be estimated by calculating the number of Hg atoms present in the laser interaction volume and estimating how many of the subsequent decays are detected at the PM after passage of the photons through the apparatus. First it is necessary to show that the laser pulse saturates the transition leaving one half of the Hg atoms in the excited state.

When the source of exciting radiation is broad band with respect to the doppler and natural widths the problem can be treated in terms of rate processes. The bandwidth of our laser has been quoted as 10GHz which is comfortably larger than the Doppler width of $\sim$ 1GHz. Since Doppler broadening

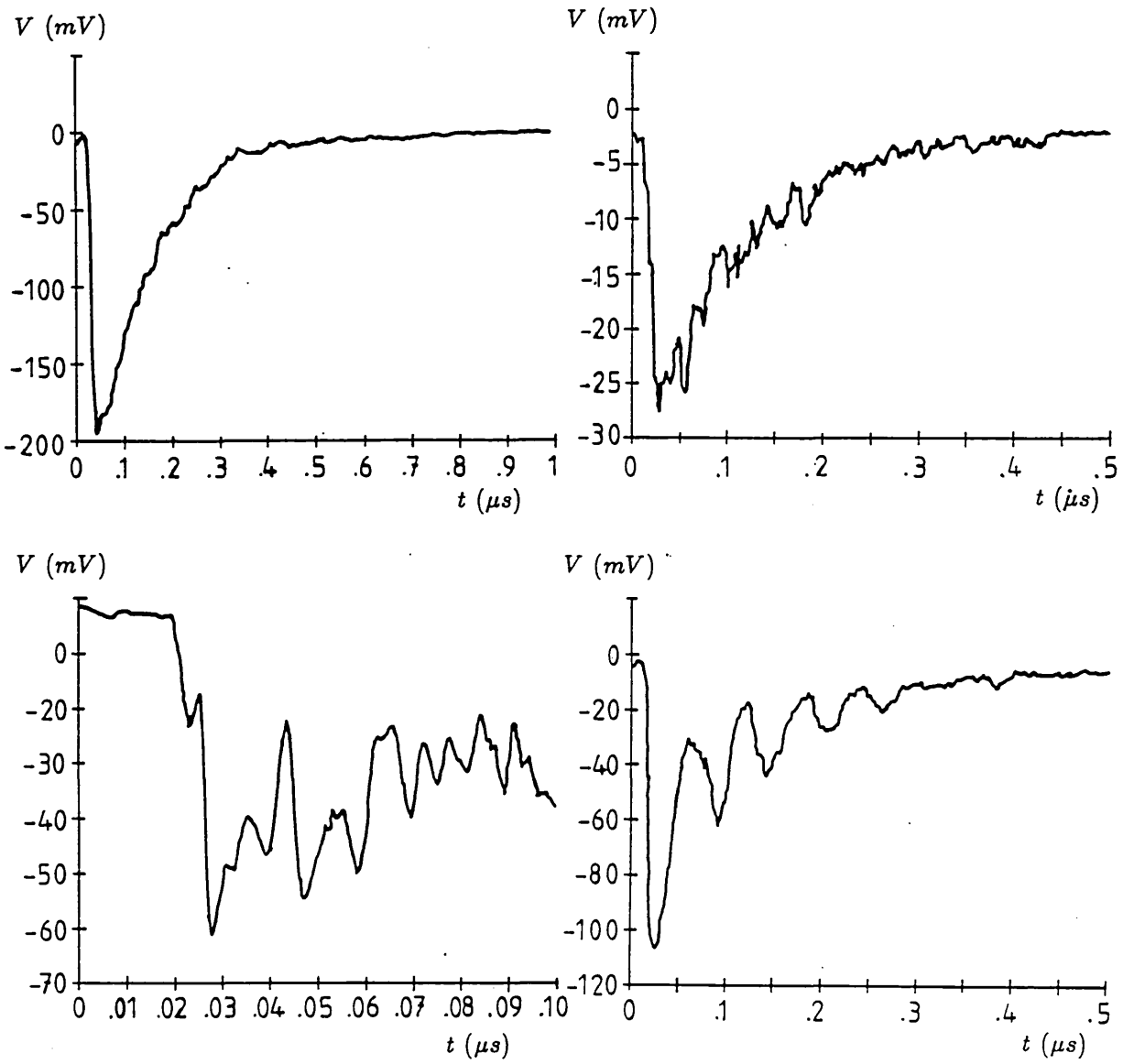


Figure 4.7 Transient digitiser plots of line centre signal. Photomultiplier output terminated into 50Ω. (a) Typical line centre trace, (b) & (c) Traces taken at lower input light level illustrating photon statistics, (d) The effect of placing a small bar magnet near the cell; oscillations due to the time dependent Hanle effect.

dominates natural broadening for a strong spectral line being emitted by an ensemble of atoms in a cell at room temperature, the rate process approach should suffice. Consideration of the usual Einstein A and B coefficients (see for example Loudon 1983) for spontaneous emission, stimulated emission and absorption leads to the rate equation

$$\frac{dN_1}{dt} = -\frac{dN_2}{dt} = N_2 A + (N_2 - N_1) BW(\omega) \tag{4.2}$$

where $(A/B) = (\hbar\omega^3)/(\pi^2 c^3)$ for a 2 level atom, N_1 and N_2 are the populations of the lower and upper states respectively and $W(\omega)$ is the energy density of radiation at frequency ω. If a beam of constant $W(\omega)$ is switched on at time $t = 0$ when all the atoms are in their ground state the solution of equation 4.2 is

$$N_2 = \frac{NBW(\omega)}{A + 2BW(\omega)} \left[1 - e^{-(A+2BW(\omega))t}\right] \tag{4.3}$$

with $N = N_1 + N_2$. For times that are long, when $(A + 2BW(\omega))t \gg 1$, the number of excited atoms approaches the steady state value of $N_2 = NBW(\omega)/(A+2BW(\omega))$ which has a limiting value of $N/2$ when $BW(\omega) \gg A$.

A spot of diameter 70μm, a pulse length of 5ns and a pulse energy of 100μJ gives $I = 5 \times 10^{12}\mathrm{Wm}^{-2}$ as the fluence of the beam. Using

$$I = I(\omega)\, d\omega = \frac{cW(\omega)\, d\omega}{\eta} \tag{4.4}$$

where η is the refractive index and will be taken as unity and taking $d\omega = 2\pi \times 1 \times 10^{10}$ as the laser bandwidth gives $W(\omega) = 1.7 \times 10^{-6} Jm^{-3} Hz^{-1}$. Substitution of these values gives $(A+2BW(\omega))t = 9 \times 10^5$ which easily satisfies the saturation condition giving $N_2 = N/2$.

Experiments were carried out at a perturber pressure of 2mBar. As will be shown in the following chapter, at such a high perturber pressure the fluorescence is largely isotropic. Signal detection at f/10 means that $\sim 6 \times 10^4$ of the emitted photons pass through the collecting lens. The quantum efficiency of the PM is quoted as 15% in the spectral region of interest. The transmission of the analyser was found to be $\sim$ 50% . This low value can be attributed to reflection losses at the four surfaces, two of which are angled. Reflection losses are also

suffered at the output window of the experimental cell and at the monochromator mirrors and PM windows yielding a throughput of ~70% . Allowing a nominal grating efficiency of 30% gives an overall collection efficiency of $\sim 10^{-5}$.

The density of Hg atoms at room temperature was $3 \times 10^{13} cm^{-3}$. The volume of the interaction region V is given by $V = \pi R^2 l = 4 \times 10^{-5} cm^3$. This gives the number present in the interaction region as $\sim 10^9$. Of these one half are excited giving $N_e = 5 \times 10^8$. Multiplication by the collection efficiency gives 5000 photons detected per shot. This compares very favourably with the observed behaviour.

4.6.2 Detuned Signal.

The signal at a detuning of $5cm^{-1}$ and a Kr pressure of 2mBar was found to be $\sim$ 5 photons per shot. In order to make an estimate of the expected signal under these conditions it is first necessary to estimate the population created in the excited state by the detuned laser pulse. A detuning of $5cm^{-1}$ in the Hg($^3P_1$—$^1S_0$)–Kr system corresponds to the region where the impact and quasistatic approximations meet. By treating the problem in the impact limit we can make an order of magnitude estimate of the expected signal. Loudon (1983) solves the optical Bloch equations for an ensemble of atoms undergoing collisions within the impact approximation. The steady state solution for ρ_{22}, the population of the excited state, is

$$\rho_{22} = \frac{1}{\gamma_N} \cdot \left\{ \frac{\frac{1}{4}\gamma' |\Omega|^2}{\Delta^2 + \gamma'^2 + \frac{1}{2}(\gamma'/\gamma_N)|\Omega|^2} \right\} \tag{4.5}$$

where

- Δ $=(\omega_0 - \omega)$ =Detuning
- γ' $=(\gamma_C + \gamma_N)$
- $|\Omega|$ $=e^2|r|^2E^2/\hbar^2$ = Rabi Frequency

To estimate the excited state population created through excitation during a short pulse we can write Excited State Population $\approx$ Rate of Excitation/Rate of Decay. Taking γ_N to be the rate of decay, the rate of excitation is given by

$\{...\}$ in equation 4.5. We can then write the excited state population created in a pulse as

$$\rho_{22_P} = \left\{ \frac{\frac{1}{4}\gamma'|\Omega|^2}{\Delta^2 + \gamma'^2 + \frac{1}{2}(\gamma'/\gamma_N)\,|\Omega|^2} \right\} .T_P \qquad (4.6)$$

where T_P is the pulse duration.*

In order to calculate ρ_{22_P} we must first estimate $|\Omega|$, Δ and γ_C. $\Delta = (\omega_0 - \omega)$ is $\approx 1 \times 10^{12}\ rad s^{-1}$ for a detuning of $5cm^{-1}$. We can find γ_c using equation 2.11 with $\overline{v} = 322ms^{-1}$, at a pressure of $2mBar$ and with $\sigma_R = 227 \pm 10 \times 10^{-16} cm^2$ (see table 6.1). Using these values we find $\gamma_c = 3.7 \times 10^7 s^{-1}$.

$|\Omega|$ can be estimated from $|\Omega|^2 = e^2|r|^2E^2/\hbar^2$. Now $e^2|r|^2$ is just the electric dipole strength S (see Thorne 1977) which can be found using $S \approx 3.5 \times 10^{-77}\lambda^3 A_{21}$ where λ is in Å and A_{21} is the Einstein A value of the excited state. For the system under study we find $S = 5.7 \times 10^{-60} C^2 m^2$. The electric field strength E can be calculated using $P = (1/2)\epsilon_0 cE^2$ where P is the power. For a pulse of energy $100 \times 10^{-6} J$ lasting $5 \times 10^{-9} s$ acting on an area of $\pi(50 \times 10^{-6})^2 m^2$ we find $E^2 = 1.9 \times 10^{15} V^2 m^{-2}$ and substituting this into the expression for $|\Omega|^2$ gives $|\Omega|^2 = 1 \times 10^{24} (rad s^{-1})^2$.

Substituting these values of $|\Omega|^2$, Δ and γ_C into equation 4.6 gives $\rho_{22_P} \approx$ 1 % . Multiplying this value by the number of atoms present in the interaction region and by the overall collection efficiency given in the previous section gives an expected count rate of 100 photons/shot. This is a factor of 20 greater than the observed signal.

It should however be noted that at linecentre the imaging of the laser focal region onto the slits is quite uncritical since even the spatial wings of the laser pulse were at high enough power densities to saturate the ensemble of atoms. When detuned to the wing the imaging is much more critical since the amount of excitation is proportional to the local laser power. With a 70μm laser focal diameter and 80μm slits it is easy to envisage at least a loss of signal of a factor of 2 as a result of poor imaging. Furthermore the PM is unlikely to have performed at its quoted quantum efficiency of 15% as a result of general shelf deterioration (it had been in stock for $\sim$ 18 months prior to the experiment). Allowing for these mitigating factors brings the calculated expected signal to

$\gamma_N (\equiv \gamma_n$ elsewhere) = the natural decay rate = $8.47 \times 10^6 s^{-1}$.

within a factor of 2 or 3 of the observed signal. Given the approximate nature of the calculation this seems a reasonable agreement.

Chapter 5

Data Correction and Results.

5.1. Introduction.

Towards the end of this chapter we will present our results. Before this can be done it is necessary to examine carefully any unwanted processes that can lead to depolarization of the collisionally redistributed fluorescence. We will be discussing processes affecting the asymptotically free atom that emerges from the collision. We can therefore draw on the literature of resonance fluorescence in much of the following analysis. There will be little discussion of the physics of collisional redistribution in this chapter.

The processes to be considered are ; 1) The effect of hyperfine structure. 2) The Hanle effect. 3) Radiation trapping and 4) Collisional depolarization. We will also consider the way in which these processes interact. A distinction should be drawn between the type of collisional depolarization that occurs as a result of excitation *during* a collision, which is the main subject of this thesis, and the less interesting case of collisions which disturb the polarization of an atom already in its excited state. It is the latter case which will be dealt with in this chapter.

5.2 Time-Dependent, Finite-Pressure Correction.

5.2.1 Theoretical Background.

The mercury atom leaves the collision with an alignment $\alpha^{(2)}(\Delta\omega)$ given by eq.2.53. The atom then decays to its ground state according to its natural lifetime. During the time spent in the excited state, between the collision and subsequent decay the atom has a finite probability of experiencing a second collision with a perturber atom, reducing the alignment. Ideally one would perform experiments in a pressure regime in which this effect was negligible however limitations on signal often require the experiment to be performed at

higher pressures. It is therefore necessary to seek a method of correcting for this effect when data have been collected at finite pressure.

Omont (1965a) has shown that the alignment decays exponentially as a result of this process with a time constant $\gamma_c^{(2)}$ dependent on perturber gas pressure. Using eq.2.52 we can write

$$\alpha^{(2)}(\Delta\omega,t) = \alpha^{(2)}(\Delta\omega)e^{-\gamma_c^{(2)}t} = \frac{I_{\|}(t) - I_{\perp}(t)}{I_{\|}(t) + 2I_{\perp}(t)} \tag{5.1}$$

At the same time the total population in the upper state decays with the time constant γ_n:

$$I(t) = \gamma_n e^{-\gamma_n t} = I_{\|}(t) + 2I_{\perp}(t) \tag{5.2}$$ *

where the total fluorescence radiated has been normalized ($\int_0^\infty I(t)\,dt = 1$). Equations 5.1 and 5.2 can be solved giving $I_{\|}(t)$ and $I_{\perp}(t)$ in terms of γ_n,$\gamma_c^{(2)}$ and $\alpha^{(2)}(\Delta\omega)$.

$$I_{\|}(t) = \gamma_n e^{-\gamma_n t}\left\{1 - \frac{2}{3}(1 - \alpha^{(2)}(\Delta\omega)e^{-\gamma_c^{(2)}t})\right\} \tag{5.3}$$

$$I_{\perp}(t) = \gamma_n e^{-\gamma_n t}(1 - \alpha^{(2)}(\Delta\omega)e^{-\gamma_c^{(2)}t}) \tag{5.4}$$

Defining $I_{\|}^T = \int_0^T I_{\|}(t)\,dt$ and $I_{\perp}^T = \int_0^T I_{\perp}(t)\,dt$ we can write the quantity α^T, representing the alignment measured using a gate of length T, as follows

$$\alpha^T = \frac{I_{\|}^T - I_{\perp}^T}{I_{\|}^T + 2I_{\perp}^T} \tag{5.5}$$

and substitution of eq.5.3 and eq.5.4 into eq.5.5 gives

$$\alpha^T = \frac{\alpha^{(2)}(\Delta\omega)\gamma_n}{\gamma_c^{(2)} + \gamma_n}\,\frac{[e^{-(\gamma_c^{(2)}+\gamma_n)T} - 1]}{[e^{-\gamma_n T} - 1]} \tag{5.6}$$

Previous polarization monitored collisional redistribution experiments (eg. Alford *et al.*1984) have been conducted using a continuous wave (CW) laser and boxcar integrated detection. It is therefore profitable to mention the steady state solution of equation 5.6 to facilitate comparison with previous work.

The alignment measured in a CW experiment is identical to the alignment measured in a pulsed experiment in which the gate length is infinite. When,

* I(t) is the number of photons emitted per second. γ_n appears as the constant of proportionality in eq. 5.2 as a result of normalization. This normalization is not strictly necessary since the constant drops out in evaluating equation 5.5.

as in our case , the gate length is finite, the very depolarized tail end of the fluorescence is not collected. The alignment measured is therefore higher than the steady state value. The steady state result is obtained by substituting $T = \infty$ into eq.5.6. yielding

$$\alpha^{\infty} = \frac{\alpha^{(2)}(\Delta\omega)\gamma_n}{\gamma_c^{(2)} + \gamma_n} \tag{5.7}$$

And substitution of this into eq.2.51 yields

$$P = \frac{3\alpha^{(2)}(\Delta\omega)}{2 + \alpha^{(2)}(\Delta\omega) + \frac{2}{\gamma_n}\left(\frac{\gamma_c^{(2)}}{n_p}\right) n_p} \tag{5.8}$$

which is identical to the result of Burnett and Cooper (1980b). Returning to the case of finite gate length and defining a parameter β through

$$P = \frac{3\beta}{2 + \beta} \tag{5.9}$$

we have

$$\frac{3 - P}{2P} \equiv \frac{1}{\beta} = \frac{1}{\alpha^{(2)}(\Delta\omega)K}\left[1 + \frac{1}{\gamma_n}\left(\frac{\gamma_c^{(2)}}{n_p}\right) n_p\right] \tag{5.10}$$

with K given by

$$K = \frac{1 - e^{-(\gamma_n + \gamma_c^{(2)})T}}{1 - e^{-\gamma_n T}} \tag{5.11}$$

Equation 5.10 predicts a straight line for a plot of $1/\beta$ versus perturber pressure (such a plot for the case of Sr–Ne is shown in fig 5.1). The slope and $1/\beta$ intercept are dependent on detuning but the pressure intercept is independent of detuning. In the systems studied previously (Alford *et al.* 1984) values of $\gamma_c^{(2)}/n_p$ were not known from independent sources and the above analysis provided a means of determining these constants. In the case of Hg-Kr values of $\gamma_c^{(2)}/n_p$, arrived at through Hanle effect experiments, are tabulated in the literature (see Lewis 1980 for a review and some useful tables).

5.2.2 Application to the Case of Hg-Kr.

We have carried out an experiment in which the polarization was measured as a function of perturber pressure at a fixed detuning. The results are shown in

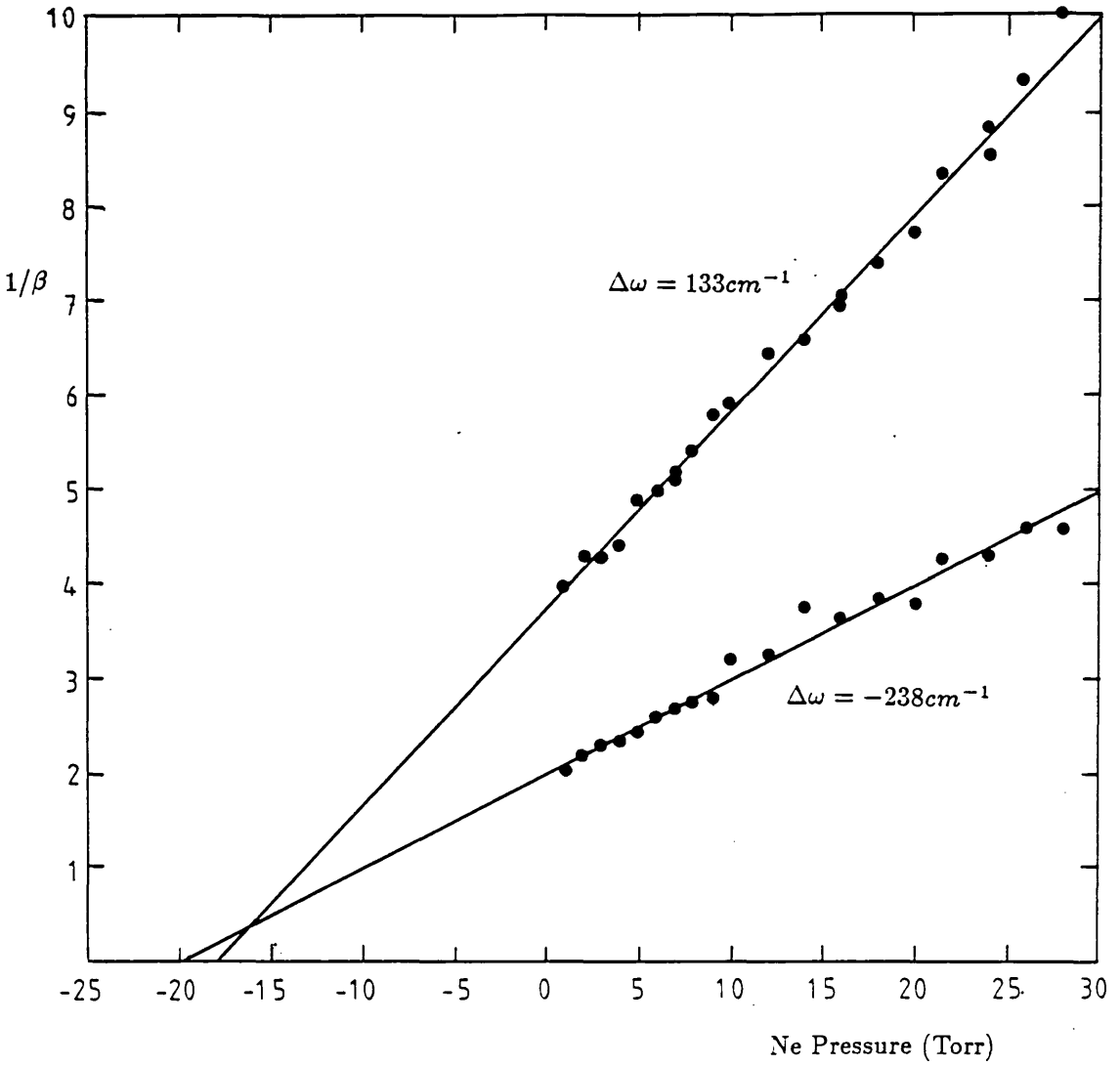


Figure 5.1 Plot of $1/\beta$ vs. pressure for Sr($^1P_1$–$^1S_0$)–Ne. The parameter $1/\beta$ plotted against perturber pressure yields a straight line. The slope varies with detuning but the pressure intercept is constant. The quantity $\gamma_c^{(2)}/n_p$ is determined from the pressure intercept. (From Alford (1984))

figure 5.2. The error bars reflect the statistical error associated with shot noise. The experimental points show a reasonable scatter about the fitted line. There is good agreement between the extrapolated value of the $1/\beta$ intercept and the theoretical value given by Lewis (1980).

This plot can be compared with similar ones for Sr–Ne published by Alford *et al.* (1984) (see fig 5.1). They were able to perform their detuning experiments at a perturber pressure at which the effect of secondary collisions on the polarization was minimal ($\sim$ a few per cent). They used equation 5.8 and their experimental value of $\gamma_c^{(2)}/n_p$ to correct their data, giving the "zero pressure" polarization.

Lack of sufficient experimental signal forced us to perform our detuning experiments at a perturber pressure at which the effect of secondary collisions was considerable. It was therefore fortuitous that the value of $\gamma_c^{(2)}/n_p$ was well known for Hg perturbed by Kr. This allowed us to increase our signal by increasing the perturber pressure. The "zero pressure" result was then retrieved by the application of equation 5.10.

5.3 Depolarization as a Result of Hyperfine Structure.

Naturally occurring mercury consists of a mixture of isotopes with abundances of 70% for $I = 0$, 17% for $I = 1/2$ and 13% for $I = 3/2$, where I represents the nuclear spin (Percival & Seaton 1958). When $I \neq 0$ a hyperfine interaction can occur in which J and I couple to form a resultant F. If the J–I interaction is sufficiently weak to be regarded as a perturbation a coupling scheme analogous to L–S coupling can be employed. The result is that when $I = 1/2$ or $3/2$ the fluorescence is depolarized somewhat by the precession of J about F. In mercury the size of the hyperfine interaction is such that the hyperfine structure has time to develop almost fully before decay ($\Delta\omega_{\rm hfs}\tau_n >> 1$) whilst it does not play a role *during* the collision ($\Delta\omega_{\rm hfs}\tau_c << 1$). The Hyperfine splittings for Hg are given in table 5.1.

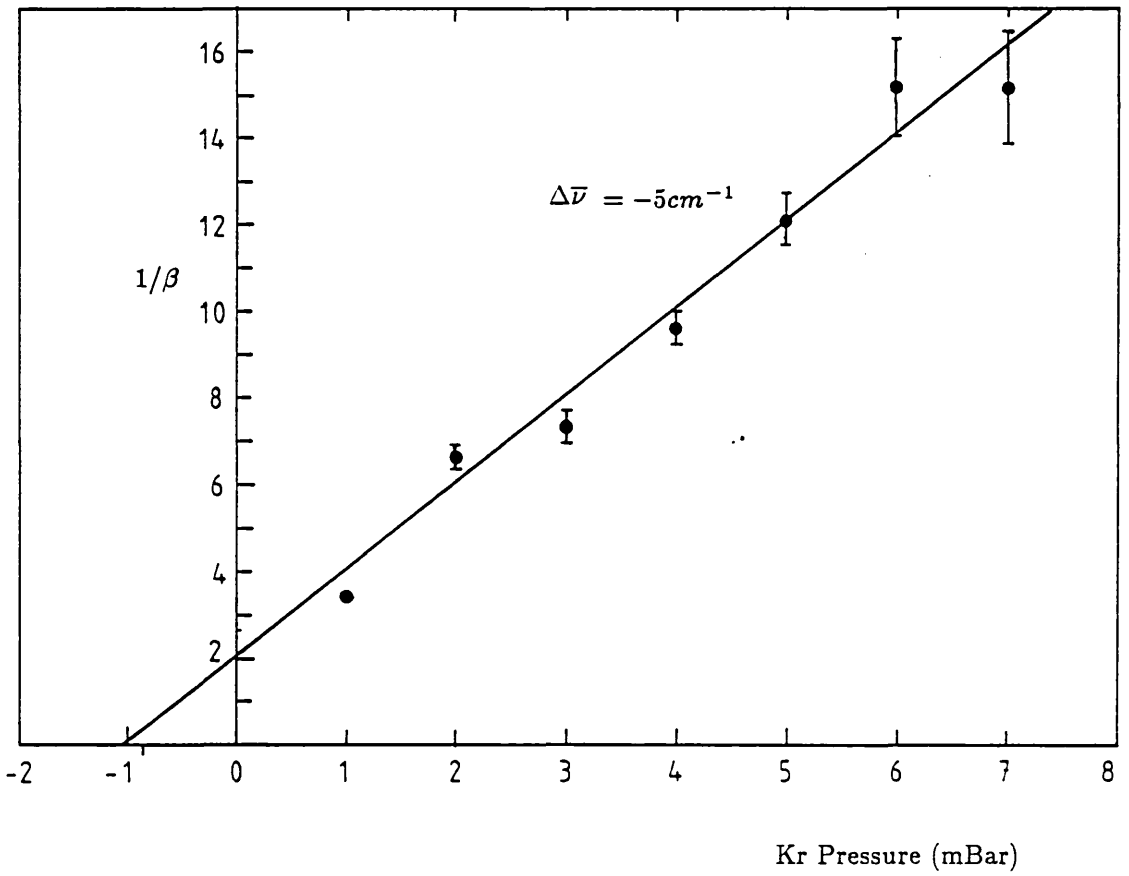


Figure 5.2 **Plot of $1/\beta$ vs. pressure for Hg($^3P_1$—$^1S_0$)–Kr.**

Table 5.1

Isotope	F	$\Delta\overline{\nu}(cm^{-1}_{\times 10^3})$
201	1/2	+229.4
199	3/2	+224.6
198	1	0
201	3/2	−22.6
200	1	−160.4
202	1	−337.2
201	5/2	−489.3
204	1	−511.1
199	1/2	−514.3

Hyperfine structure of the Hg 2537Å line. The detunings of the hyperfine components are measured with respect to the position of the component for the isotope ^{198}Hg. (From Corney 1977).

Percival & Seaton (1958) have analysed the analogous problem in L–S coupling. They consider the depolarization arising from the precession of L about J in the collection of fluorescence from an unresolved L–S multiplet following excitation by electron impact. In order to use their analysis we make the identification

$$\begin{aligned} L &\rightarrow J \\ S &\rightarrow I \\ J &\rightarrow F \end{aligned} \tag{5.12}$$

They show that the polarization can be written as

$$P^I = \frac{G(\sigma_0 - \sigma_1)}{h_0\sigma_0 + h_1\sigma_1} = \frac{I^I_{\|} - I^I_{\perp}}{I^I_{\|} + I^I_{\perp}} \tag{5.13}$$

where $\sigma_{|M_L|}$ are the sublevel populations and G , h_0 and h_1 are expressed as sums over Clebsch-Gordan coefficients. The superscript I expresses the fact that G, h_0 and h_1 are different for different nuclear spins. They tabulate these constants for various values of L and S. For $S = 1/2$ and $L = 1 \rightarrow 0$ they find

$G = 3$, $h_0 = 7$, $h_1 = 11$. Making the transformation of eq.5.12 these constants apply to hyperfine structure of the 2537Å line in Hg isotopes with $I = 1/2$.

Alford *et al.* calculated G , h_0 and h_1 for the case of $I = 3/2$ in order to analyse their results for naturally occurring Barium, which contains 18% isotopes with $I = 3/2$. They found for $I = 3/2$, $G = 111$, $h_0 = 337$ and $h_1 = 563$. If we take n as the fraction of $I = 1/2$ isotopes and m as the fraction of $I = 3/2$ isotopes in the mixture we can normalize the total fluorescence through

$$\begin{aligned} 1 - (n+m) &= I_{\|}^{0} + 2I_{\perp}^{0} \\ n &= I_{\|}^{1/2} + 2I_{\perp}^{1/2} \\ m &= I_{\|}^{3/2} + 2I_{\perp}^{3/2} \end{aligned} \tag{5.14}$$

where again the superscript refers to nuclear spin. If we write

$$P = \frac{\sigma_0 - \sigma_1}{\sigma_0 + \sigma_1} \tag{5.15}$$

then P is the polarization that would be measured in the absence of any hyperfine structure. We can then calculate

$$P_0 = \frac{I_{\|}^{0} - I_{\perp}^{0} \; + \; I_{\|}^{1/2} - I_{\perp}^{1/2} \; + \; I_{\|}^{3/2} - I_{\perp}^{3/2}}{I_{\|}^{0} + I_{\perp}^{0} \; + \; I_{\|}^{1/2} + I_{\perp}^{1/2} \; + \; I_{\|}^{3/2} + I_{\perp}^{3/2}} \tag{5.15}$$

where P_0 is the actual polarization measured. Solution of equations 5.13 , 5.14 and 5.15, with the appropriate values for G , h_0 and h_1 yields P in terms of P_0:

$$P = P_0 \Big/ \left[1 - \left(\frac{2n}{9} + \frac{113m}{450}\right)(3 - P_0)\right] \tag{5.16}$$

Although samples of enriched even isotopes of Hg are available they are very expensive and their use can only be justified in experiments where the effects if hyperfine structure obscure the processes under direct investigation. Since the effects of hyperfine structure on our experiment are well understood the complications that arise when naturally occurring mercury is used, do not greatly obscure the physics of interest.

5.4 Depolarization as a Result of Radiation Trapping.

When there is a large concentration of ground state atoms in the experimental cell a photon radiated from an atom has a certain probability of being reabsorbed by one of these ground state atoms before leaving the cell and travelling to the detector. Information about the polarization of the original atom in its excited state may be partially transmitted to the next atom. A classical picture of the process is shown schematically in figure 5.3.

The original atom A radiates preferentially in the xz plane with the usual dipole pattern. If an atom near the z axis (B) traps the radiated photon the re-emitted photon will be polarized identically to the original photon. Atom B will radiate with the dipole pattern. The re-emitted photon will have a far smaller chance of reaching the detector. If the re-emitted photon does reach the detector the process will have effectively doubled the lifetime of the excited state for this route.

There is a smaller probability of the original photon being emitted off axis towards atom C. This atom will be linearly polarized perpendicular to the photon's propagation direction. The dipole radiation pattern from atom C now has a y component. Light re-emitted from C in the direction of the detector is therefore depolarized with respect to the light emanating from A.

Radiation trapping was first noticed in experiments designed to measure excited state lifetimes. The two methods in use were optical double resonance techniques and the Hanle effect. It was noted that the experimental widths became smaller as the pressure of the emitting gas was increased and the effect was dubbed coherence narrowing.

Barrat (1959a,b,c) developed a density matrix theory describing radiation trapping (or multiple diffusion). He showed that for even isotopes, the decay rates for population, orientation, and alignment are decreased by trapping according to

$$\Gamma_{\text{eff}}^{(k)} = \Gamma^{(k)}(1 - \alpha^{(k)}x) \tag{5.17}$$

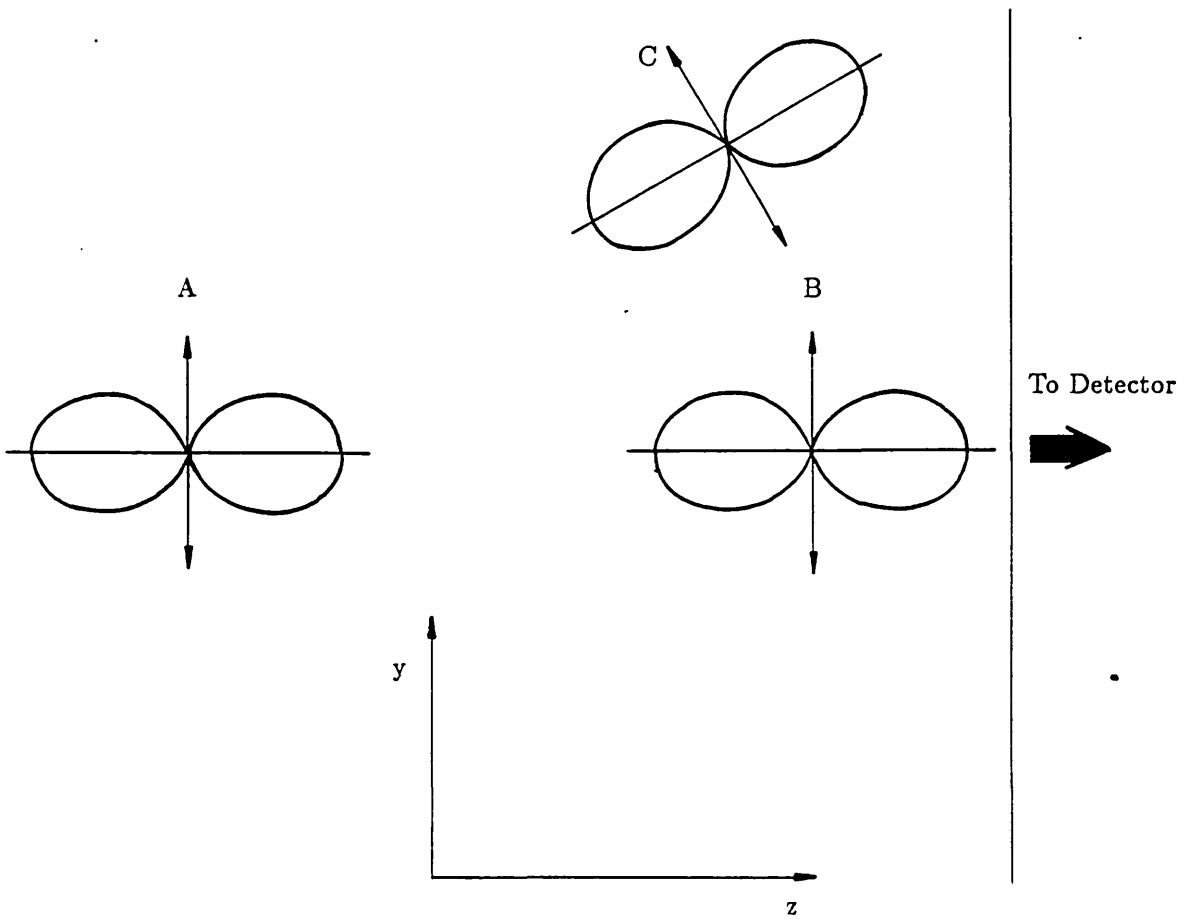


Figure 5.3 The origin of depolarisation via radiative trapping. A classical picture of the process is given. If atom A radiates in the $+z$ direction, atom B may absorb the photon and re–emit it towards the detector. This route leads to a delay but no depolarisation. If atom A radiates towards atom C where the photon may be absorbed then light re-emitted from C to the detector is both delayed and partially depolarised, since the oscillation of the dipole on C has a z component.

where

Population	$k = 0$	$\alpha^{(0)} = 1$
Orientation	$k = 1$	$\alpha^{(1)} = 1/2$
Alignment	$k = 2$	$\alpha^{(2)} = 7/10$

and x is the fraction of emitted photons that are trapped. He also calculated $\alpha^{(k)}$ values for odd isotopes. Barrat proposed a form for x however D'Yakonov & Perel (1965) improved upon this and calculated x to be given by

$$x = 1 - \frac{1}{\sqrt{\pi}} \int_{-\infty}^{+\infty} exp\{-k_0 L e^{-y^2}\} e^{-y^2} \, dy \tag{5.18}$$

where the length parameter L is of the order of the dimensions of the resonance cell and k_0 is the absorption coefficient at line centre given by

$$k_0 = \frac{\lambda_0^3 n_p}{8\pi} \frac{g_k}{g_0} A_{k0} \left[\frac{M}{2\pi k T} \right]^{1/2} \tag{5.19}$$

where n_p is the number density of atoms, A_{k0} is the Einstein A value for the transition and λ_0 is the wavelength of the absorption line.

Barrat also showed that the polarization of the fluorescence from atoms excited with π polarized light and subject to radiation trapping is given by

$$P = \frac{1 - x}{1 - 4x/5} \tag{5.20}$$

for even isotopes. He calculated similar formulae for the odd isotopes. It should be noted that in the limit of complete trapping , when x=1 , $(1-\alpha^{(k)}x)$ takes on a finite value for $k = 1$ and $k = 2$. $\alpha^{(k)}$ represents the average coherence transferred from one atom to another through the exchange of a photon. It should be noted however that the actual polarization measured , given by equation 5.20 , approaches zero in the limit of large trapping.

5.5 Depolarization of Resonance Fluorescence by External Magnetic Fields (The Hanle Effect)

In experiments on the Hg 2537Å line Wood & Ellet (1924) showed that it is possible to destroy the polarization of resonance fluorescence by the application

of a small external magnetic field. Hanle (1924) carried out further experimental investigations into this effect for the same system and was able to work out a classical theory which accounted for his results. He found that fields of the order of 5 Gauss were sufficient to almost completely depolarize the 2537Å radiation. The effect of the Earth's magnetic field ($\sim$ 0.5 Gauss) cannot therefore be assumed to be negligible. A comprehensive treatment of the classical and quantum mechanical theories of the Hanle Effect appears in Corney (1977). In the quantum mechanical formulation Corney shows that, for pulsed excitation and with the experimental geometry of figure 5.4, $dI/d\Omega$, the intensity of fluorescence radiated into a solid angle $d\Omega$ is given by

$$\frac{dI}{d\Omega} = \frac{U(\omega)}{8\pi\epsilon_0^2}\left[\frac{\omega}{\hbar c}\right]^3 \sum_{\substack{mm' \\ \mu\mu'}} F_{mm'}G_{m'm}\rho_{\mu\mu}exp[-\{\Gamma + i\omega_L(m-m')\}(t-t_0)] \tag{5.21}$$

Here $F_{mm'} = \langle m|\hat{\underline{e}}.\underline{D}|\mu\rangle\langle\mu|\hat{\underline{e}}^*.\underline{D}|m'\rangle$ is the excitation matrix and $G_{m'm} = \langle m'|\hat{\underline{e}}'.\underline{D}|\mu'\rangle\langle\mu'|\hat{\underline{e}}'^*.\underline{D}|m\rangle$ is the de-excitation matrix with $\hat{\underline{e}}.\underline{D}$ given by

$$\hat{\underline{e}}.\underline{D} = -(\epsilon_{+1}D_{-1} + \epsilon_{-1}D_{+1}) + \epsilon_0 D_0 \tag{5.22}$$

where $\epsilon_{\pm 1}$, ϵ_0 are spherical unit vectors defined through

$$\begin{aligned} \epsilon_\pm &= \mp\frac{1}{\sqrt{2}}(e_x + ie_y) = \mp\frac{1}{\sqrt{2}}(\cos\theta\cos\alpha \pm i\sin\alpha)e^{\pm i\phi} \\ \epsilon_0 &= e_z = -\sin\theta\cos\alpha \end{aligned} \tag{5.23}$$

and D is defined similarly in terms of $D_{\pm 1}$ and D_0. Here $U(\omega)$ is the Planck spectral density, $\omega_L = g_J eB/2M$ is the Larmor frequency and t_0 is the time at which the excitation pulse arrives at the cell. Equation 5.17 is found assuming a rectangular excitation pulse which is much shorter than the natural lifetime and the Larmor period. (See Corney 1977 for a full discussion of the derivation up to this point.) For the case of a $J_g = 0$, $J_e = 1$ transition and after some algebraic manipulation it can be shown that

$$\frac{dI}{d\Omega} = \frac{dI}{d\Omega}(\Delta m = 0) + \frac{dI}{d\Omega}(\Delta m = 1) + \frac{dI}{d\Omega}(\Delta m = 2)$$

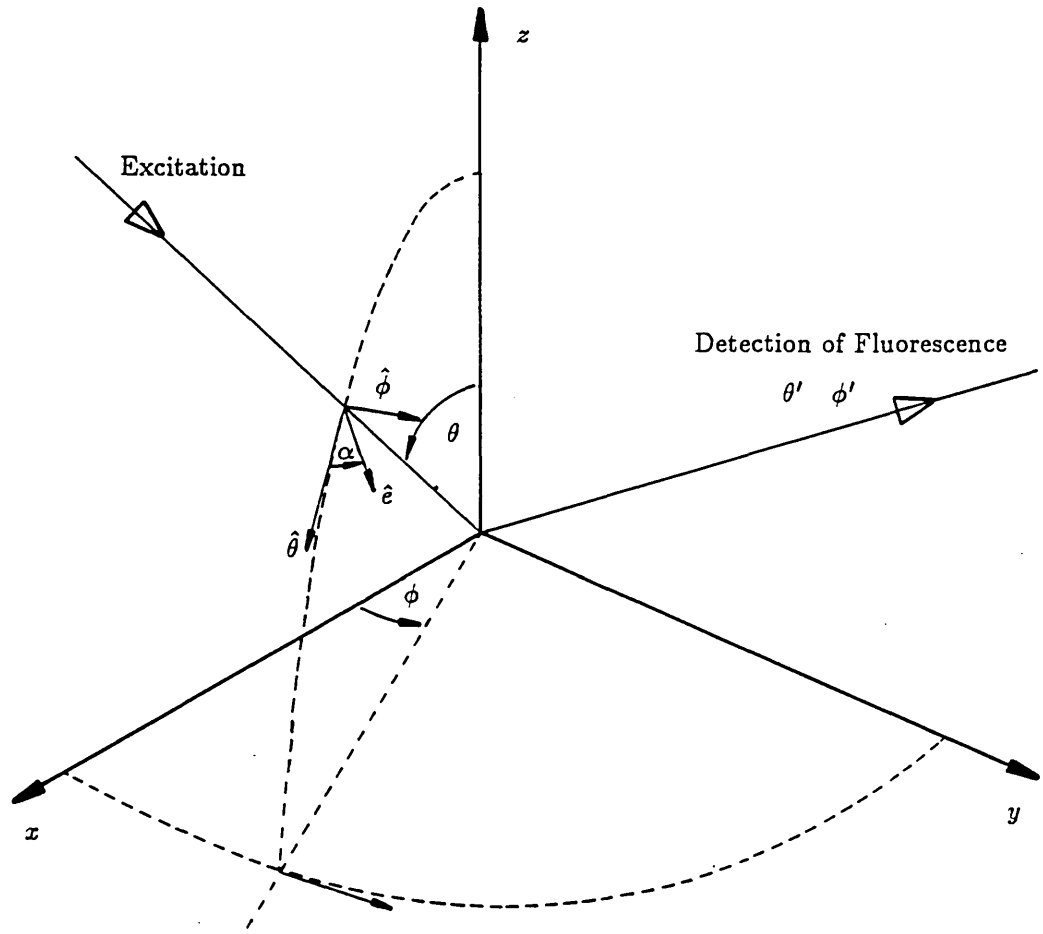


Figure 5.4 Geometry for the theoretical description of the Hanle effect. With **B** along z we are free to define $\phi = 0$. The directions are then defined once θ, θ' and ϕ' have been found. For our experiment $\alpha = 0$ or $\pi/2$, $\alpha' \neq 0$. (From Corney (1977)).

$$\frac{dI}{d\Omega}(\Delta m = 0) = \frac{C}{2}(1 + 3\epsilon_0^2\epsilon_0'^2 - \epsilon_0'^2 - \epsilon_0^2)e^{-\gamma_n t}$$
$$\frac{dI}{d\Omega}(\Delta m = 1) = -2C\epsilon_0\epsilon_0'(f\cos\omega_L t - g\sin\omega_L t)e^{-\gamma_n t}$$
$$\frac{dI}{d\Omega}(\Delta m = 2) = \frac{C}{2}(h\cos 2\omega_L t - j\sin 2\omega_l t)e^{-\gamma_n t} \qquad (5.24)$$

where

$$j = 2gf$$
$$h = f^2 - g^2$$
$$f = \cos\theta\cos\alpha\cos\theta'\cos\alpha' - \sin\alpha'\sin\alpha$$
$$g = \cos\theta\cos\alpha\sin\alpha' + \ sin\alpha\cos\theta'\cos\alpha'$$
$$C = \frac{U(\omega)}{8\pi\epsilon_0^2}\left(\frac{\omega}{\hbar c}\right)^3\langle D\rangle^4\rho_{00} \qquad (5.25)$$

Here ρ_{00} is the density of atoms in the ground state and $\langle D\rangle = \langle\gamma 0||D||\gamma' 0\rangle$ is the reduced matrix element of D. (Much of the detail of the derivation concerns calculation of elements contained within the constant C. This constant determines the intensity of the fluorescence but drops out when calculating such quantities as the polarization or the alignment. For our purposes we need only consider the angle and time dependent parts of eq.5.24.). The geometry of our experiment is described by the angles

$\theta = 78°$	$\phi = 0°$	$\alpha_{\|\|} = 15.3°$
$\theta' = 75°$	$\phi' = 93.3°$	$\alpha_{\perp} = 105.3°$
		$\alpha' = -12.4°$

where the subscripts $\|$ and $\perp$ refer the orientation of the analyser relative to the polarizer. These angles were found by measuring the Earth's magnetic field at the position of the cell. The field was found to be 0.5 Gauss and the angles θ and θ' reflect the steep angle of dip in the lab. (The Earth's magnetic field points towards magnetic north and dips in towards the centre of the earth at an angle dependent on lattitude and to some extent on the local environment ie. the proximity to large masses of ferromagnetic material)

$\alpha(t)$ as defined by eq.2.52 and calculated using equations 5.20 is plotted in figure 5.5. In order to find the polarization measured when light is collected up

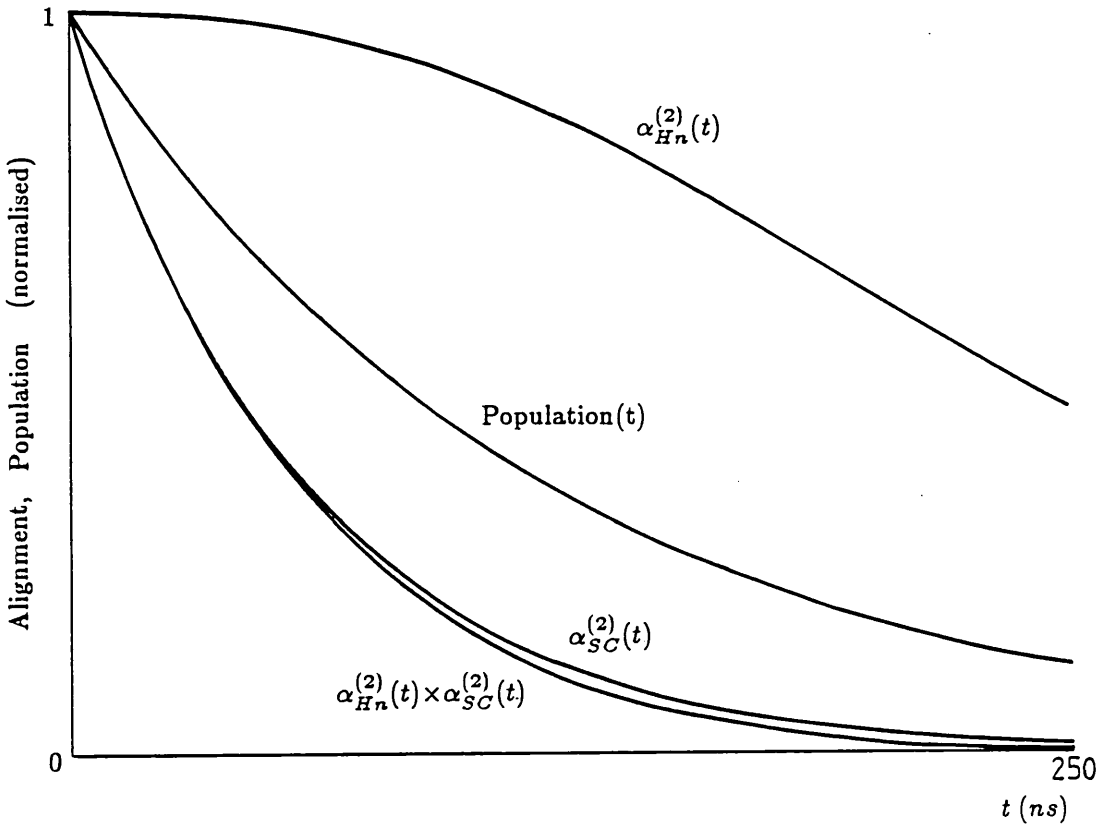


Figure 5.5 Decay of alignment via secondary collisions and the Hanle effect. The decay of alignment due to secondary collisions is calculated at $\gamma_c^{(2)} = 2\gamma_n$. The decay of alignment associtated with the Hanle effect alone, when convolved with the decay of population, can have an appreciable effect. However, the decay of alignment due to secondary collisions is much more rapid. When the two effects act together depolarisation via secondary collisions dominates. The dipole has insufficient time to precess appreciably in the external magnetic field before secondary collisions have caused a large degree of depolarisation.

to a time T the expressions 5.24 were integrated from $t = 0$ to T and the values of $dI^T/d\Omega$ substituted into eq.2.51.

In the absence of any other depolarizing effects these calculations give a polarization of 93% for the time dependent case with a 250ns gate. (The steady state result is 87%). The small degree of depolarization is the result of a modest B field, which sets the frequency of modulation of $\alpha(t)$, and a very steep dip angle which affects the depth of modulation. As is borne out by the preceding sections, the Hanle effect does not act independently of other depolarizing effects in our experiment. The interplay between the various processes is the subject of the next section.

5.6 Corrected Data.

5.6.1 Competition Between Depolarizing Processes: Timescales.

The timescale over which a given depolarizing process becomes effective has been discussed in each of the preceding sections. When the timescales for the different processes are of the same order the effects occur together. If an expression for the alignment as a function of time, $\alpha_i^{(2)}(\Delta\omega, t)$ can be found for each process then a resultant $\alpha_R^{(2)}(\Delta\omega, t)$ can be written as

$$\alpha_R^{(2)}(\Delta\omega, t) = \prod_i \alpha_i^{(2)}(\Delta\omega, t) \tag{5.26}$$

A simplification can arise if the time scales for the competing processes differ greatly. In that case the effects can be treated independently and the corrections for the effects can be applied consecutively. Two other timescales, τ_c, the collisional duration and τ_n, the natural lifetime also play a role. This was seen in § 5.3. in the context of the hyperfine effect.

We can now examine the modification to the pressure correction that occurs in the presence of hyperfine structure. Equations 5.16 and 2.51 can be solved to give

$$\alpha_M^{(2)}(\Delta\omega) = \alpha^{(2)}{}_{(\Delta\omega)} \left(1 - \left(\frac{2n}{3} + \frac{113m}{150}\right)\right) \tag{5.27}$$

where $\alpha^{(2)}(\Delta\omega)$ is the value in the absence of any hyperfine interaction. The time scale for the development of the hyperfine structure is much shorter than the alignment decay lifetime $1/\gamma_c^{(2)}$ resulting from secondary collisions (set by the perturber pressure used). The hyperfine correction discussed in § 5.3 therefore only affects the pressure correction of § 5.2 through a modification of $\alpha^{(2)}(\Delta\omega)$ in equation 5.10. That is one can consider the atom to exit the collision with an alignment $\alpha^{(2)}(\Delta\omega)$ which is reduced to the value $\alpha_M^{(2)}(\Delta\omega$ through the hyperfine interaction *before* the destruction of alignment through secondary collisions takes effect.

We can also examine the interplay between depolarization due to secondary collisions and the Hanle effect. Fig 5.5 shows four curves: a) The decay of alignment via the Hanle effect for our system , b) The decay of alignment via secondary collisions with $\gamma_c^{(2)} = 2\gamma_n$, c) The decay of alignment as a result of the Hanle effect *and* secondary collisions (found by multiplying a×b as in equation 5.26) and d) The decay of population.

Fig 5.5 shows clearly that while the Hanle effect causes significant depolarization on its own, its effect on the decay of alignment is negligible when interacting with depolarization via secondary collisions at the perturber pressure used . Again this arises because the timescale for the Hanle effect, set by the Larmor period, is greater than the time set by $1/\gamma_c^{(2)}$.

5.6.2. Application of the Theory of Radiation Trapping to our Experimental Geometry.

Sections 5.2, 5.3 and 5.5 each expose the theory of a depolarizing process and apply that theory to the experiment that we have performed. It has been possible in these cases to correct for the process and retrieve the "true"polarization. In the case of radiation trapping treated in § 5.4 the theory is by no means as straightforward or rigorous. The theory in its present form suffers from two major drawbacks. Firstly it is a steady state theory and would require modification to describe the situation in our pulsed experiment. Secondly and more seriously , is the problem of choosing a value for the length parameter L.

In the experiments of Barrat (1959c) and Omont (1965b), which tested Barrat's theory, cubic cells of side 2.5 cm were used. The length parameter was taken to be 0.8 cm or 1.0 cm by Barrat and 1.1 cm by Omont. These values were found to give the best fit to the experimental results however no strict criteria were established for the choice of L. In our experiment the choice of a length parameter is not particularly obvious. The quartz tubes that comprise our cell have diameters between 1.5cm and 2.5cm however this is probably of little significance since the transverse dimension of the region of the cell with which the laser beam interacts is much smaller. The spot size in the cell was measured to be 70μm. It seems reasonable therefore to suggest $L = 100\mu$m as a trial length parameter.

We have calculated x to be 0.15 for this value of L (ie. 15% of the radiated photons are trapped). Substitution into equation 5.20 gives a polarization of 96.6% (for a polarization of 100% in the case of no trapping).

As will become apparent in the following section the degree of depolarization attributable to trapping was found experimentally to be far greater then this (depolarization to $\sim$ 81%). Choosing a length parameter L as 500μm gives $x = 0.53$ and $P = 81.6\%$. It is certainly true that the laser beam width at the edges of the output window is greater than the size of the beam waist (at the centre of the output window) and that this larger width determines the mean distance between the beam and the output window however it seems unlikely that this could account for such a large discrepancy.

It seems more likely that the unusual geometry of our experiment is not adequately described by the theory in its present form. A test would be to perform experiments similar to those of Barrat, that measure Γ^k_{eff} directly, using our experimental set up. If a fit could be achieved to the data of that experiment through the choice of a single value of L then the theory would be deemed appropriate. It could then be used to perform the necessary correction to our detuning data (subject to extending the theory to cover pulsed excitation and detection).

5.6.3 Experiment to Determine the Correction for Radiation Trapping

As a result of this unsatisfactory situation as regards the theory a more empirical approach to the trapping correction was adopted. The degree of depolarization due to trapping was measured directly , under the same experimental conditions as existed during the detuning experiment. (With the exception that the pressure of mercury was varied and that the perturber gas used was argon. In fact experiments similar to those reported in this thesis for Hg-Kr were also performed in Hg-Ar. The Argon experiments will be reported elsewhere.)

An amount of mercury was released from the reservoir into the cell. The reservoir was then shut off from the experimental cell and 2mBar of Argon was allowed into the cell. The mixture was then sealed off and an experimental point taken. This process was repeated for mixtures of 2mBar of argon and different amounts of mercury. The polarization was measured and plotted against the total fluorescent intensity (which acted as a monitor of the Hg pressure in the cell). Due to the difficulties encountered in attempting to heat the cell uniformly we were limited to reducing the Hg pressure to values lower than that used in our detuning experiment. Extending the results to very low Hg pressures was limited by the degradation of the signal to background ratio.

The "no trapping" polarization was retrieved by assuming a straight line fit to the data and taking the polarization value of the ordinate intercept (see figure 5.6). There is an obvious source of error inherent in this process in that no justification is given for the assumption of straight line behaviour. Despite the limitations of this method it is expected that the "no trapping" polarization can be estimated to within $\pm 1.5 - 2.0\%$ on the 25% extrapolated polarization.

5.6.4 Corrected Red Wing Detuning Data

We have performed an experiment in which the polarization of the collisionally redistributed light was plotted as a function of detuning from linecentre. The results of this experiment for the red wing of the Hg 2537Å line perturbed by Kr are given in figure 5.7. The corrections were applied in the following order. Since the justification for the trapping correction was empirical it was

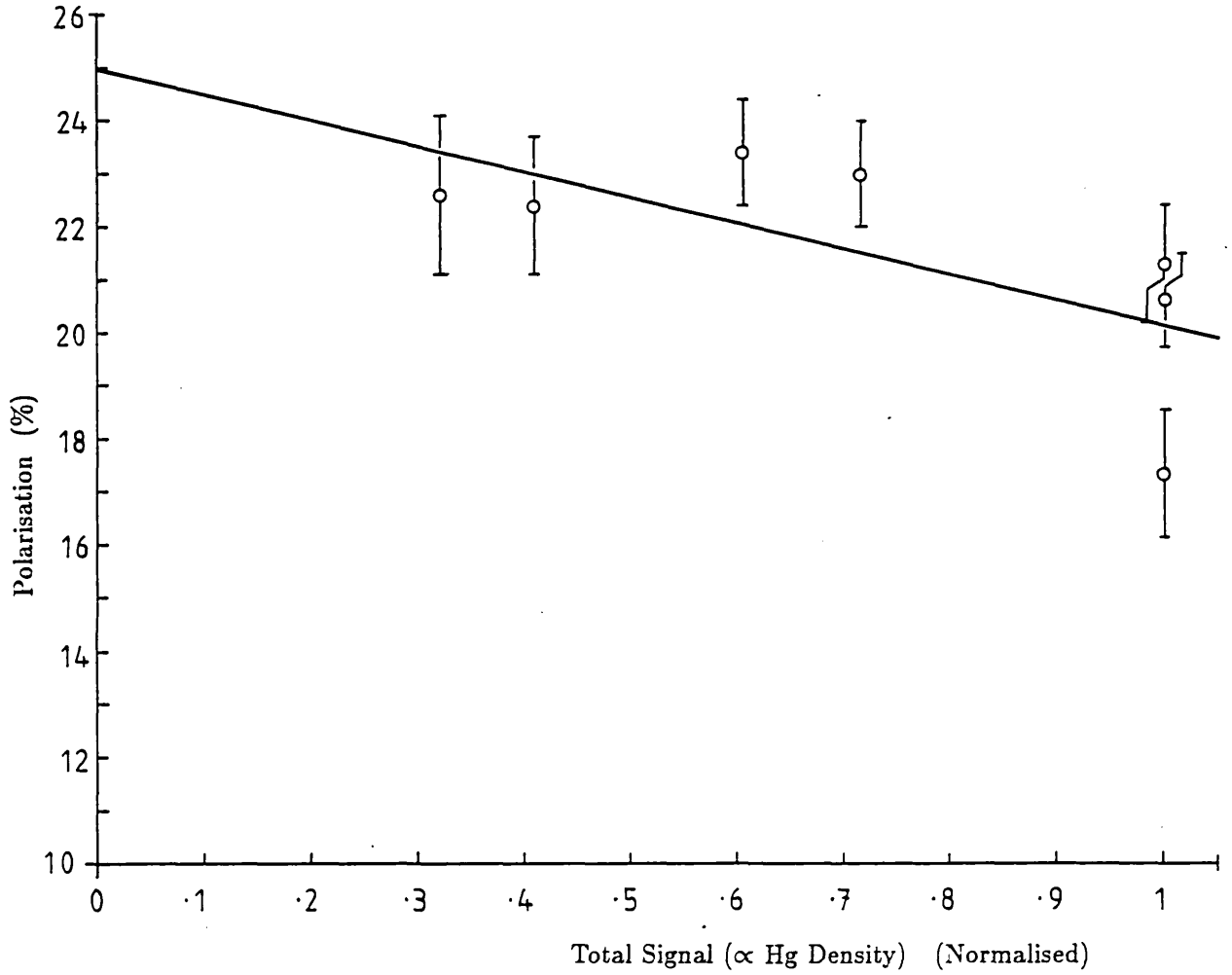


Figure 5.6 Experiment to determine degree of radiative trapping. The experiment was conducted at a detuning of $5cm^{-1}$ in the red wing. The pressure of Hg in the cell was varied and the polariastion of the redistributed light was measured at a perturber pressure of $2mBar$. A best straight line was drawn and extrapolated back to the Polarisation axis to find the "no trapping" result.

applied first. Secondly $\alpha^{(2)}(\Delta\omega)$ was tabulated from the values of P. $\alpha^{(2)}(\Delta\omega)$ was then corrected for hyperfine structure and the resultant alignment inserted into equation 5.10 to perform the pressure correction. The final value of P was then tabulated. As explained § 5.6.2 it was unnecessary to make any correction for the Hanle effect.

The hyperfine structure and finite pressure corrections are expected to be reliable whilst the trapping correction brings with it an associated error. The error bars in figure 5.7. reflect this error convolved with the statistical error. At low detunings the trapping correction error is dominant whilst at higher detunings the statistical error dominates. The large error bars at high detunings reflect the low experimental signal in this region (as low as 1 photon in ten laser shots)

5.6.5 Blue Wing Detuning Data.

Inspection of figure 3.5 reveals the asymmetry of the lineshape for Hg($^3P_1$—$^1S_0$)–Kr. Absorption in the near red wing is held up by the presence of the satellite at 10-12cm^{-1}. By contrast the blue wing lineshape falls off very steeply indeed. Our experimental signal was accordingly found to drop off extremely quickly in the blue wing. As a result it was not possible to plot a full polarization curve in the blue wing. In order to get some information about this spectral region we measured the polarization with the laser detuned to the positions of the two strongest blue wing satellites at 20cm^{-1} and at 123cm^{-1}. The corrected results are given in table 5.2.

Table 5.2

$\Delta\overline{\nu}(cm^{-1})$	Pol(%)
20	65 ± 14
123	76 ± 11

Blue wing polarization data.

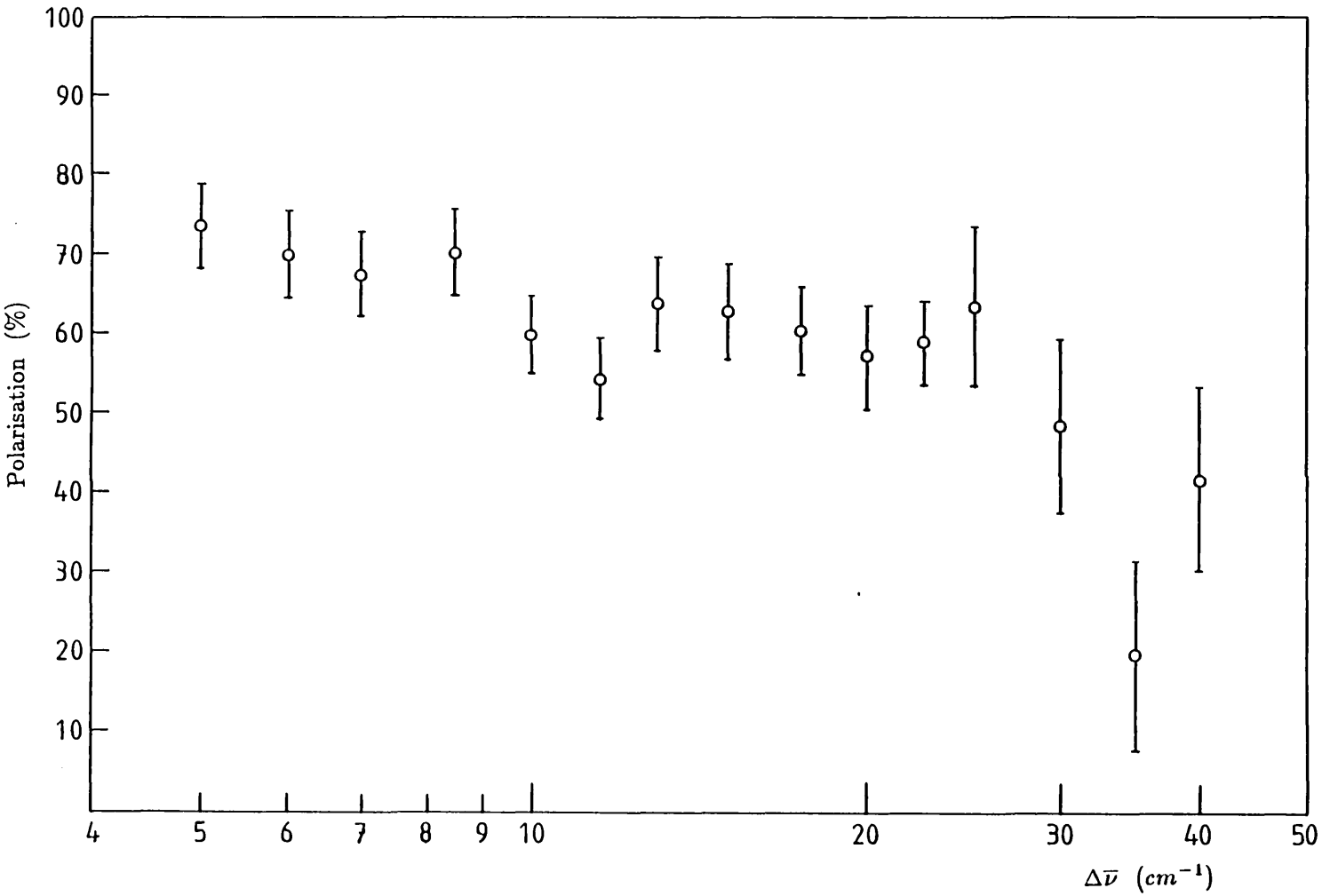


Figure 5.7 Red wing polarisation data. The error bars include shot noise and an estimated error due to the trapping correction. Shot noise dominates in the far wing.

Chapter 6.

Analysis.

6.1 Introduction : Qualitative Features.

In this chapter we will present our analysis of the experimental results based on the molecular model described in Chapter 2. For the sake of comparison we will first outline some of the features of the analysis performed by Alford *et al.* of their results for the Ba–RG and Sr–RG systems.

The main qualitative features are brought out in fig 6.1 which shows, for Ba–Xe , the three components of the problem ie. the interatomic potentials, the lineshape and the polarization spectrum $P(\Delta\omega)$. These three elements are easily inter-compared by using the relationship between detuning and the difference potential (eq.2.17) and by plotting $\Delta\omega$ on a logarithmic scale as a common abscissa. (In the case of the interatomic potentials it is more usual to find $\Delta\omega$ plotted as ordinate.)

As the detuning is increased the minimum of the Σ difference potential is approached and a satellite results. Here the total cross section for absorption increases and, since this state is effective in reorientation (see fig 2.8), a dip in the polarization is observed at this detuning. The enhanced overall absorption tells us that there is a minimum in the difference potential whilst the dip in the polarization labels it as a Σ well. As the detuning is increased further the polarization increases to a value dictated by excitation to the Π curve alone since this is now the only accessible curve.

6.2 Quantitative Analysis Performed by Lewis *et al.* of Sr–Ar Results.

Fig. 6.2 shows a comparison between the experimental results of Alford *et al.* (1984) for Sr–Ar and some theoretical curves based on the molecular model of Chapter 2, reported by Lewis *et al.* (1983). The qualitative features show a similarity to the Ba–Xe results quoted in the previous section. These features are less pronounced in the Sr–Ar case as a result of the low polarizability of

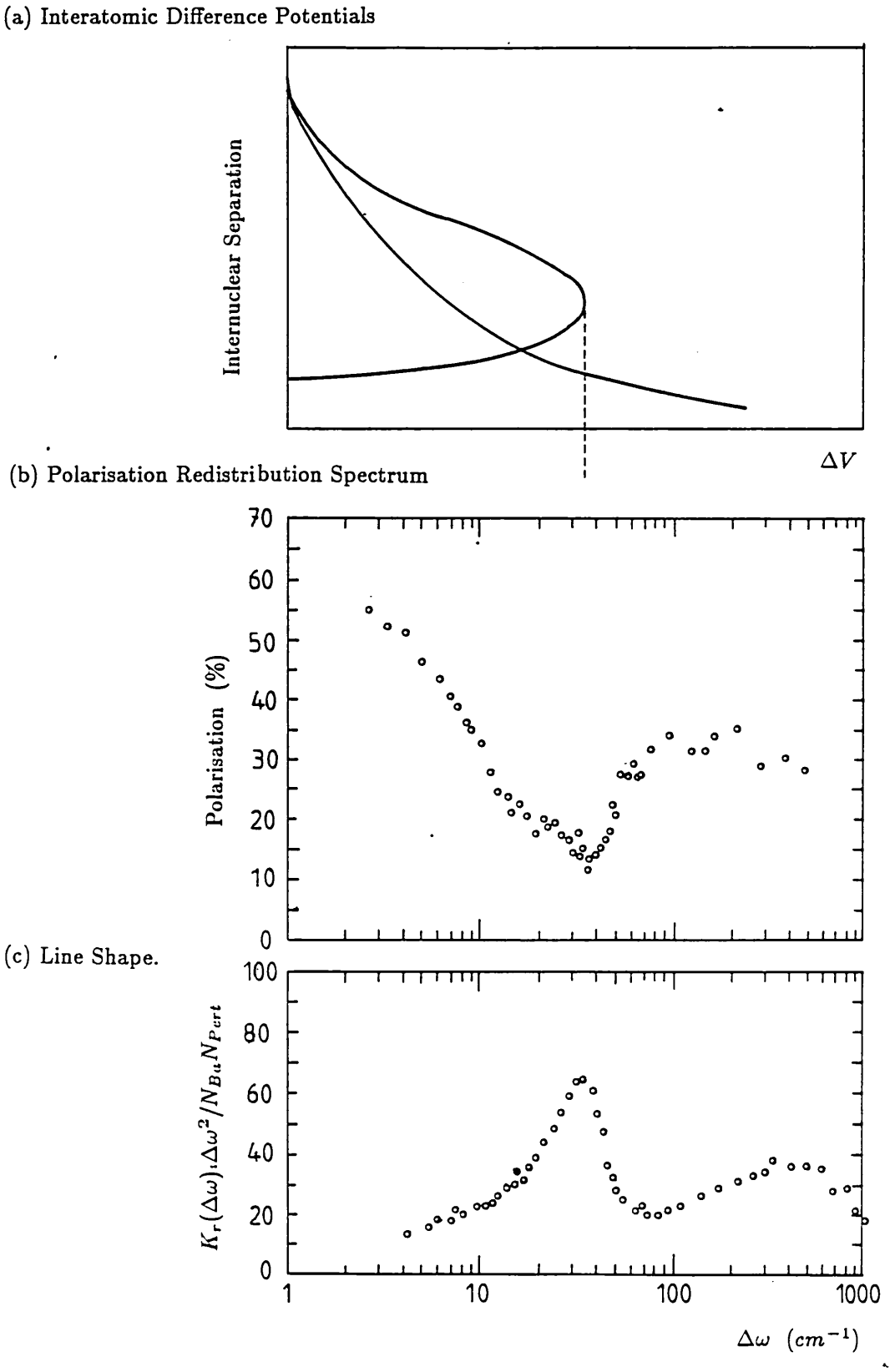


Figure 6.1 Ba–Xe interatomic difference potential, polarisation spectrum and line shape. The relationship between these three elements of the problem is shown. The minimum in the difference potential causes a satellite in the line shape and a dip in the polarisation. The interatomic potentials are schematic. Their shape has been partly inferred *from* the polarisation data. (From Alford (1984))

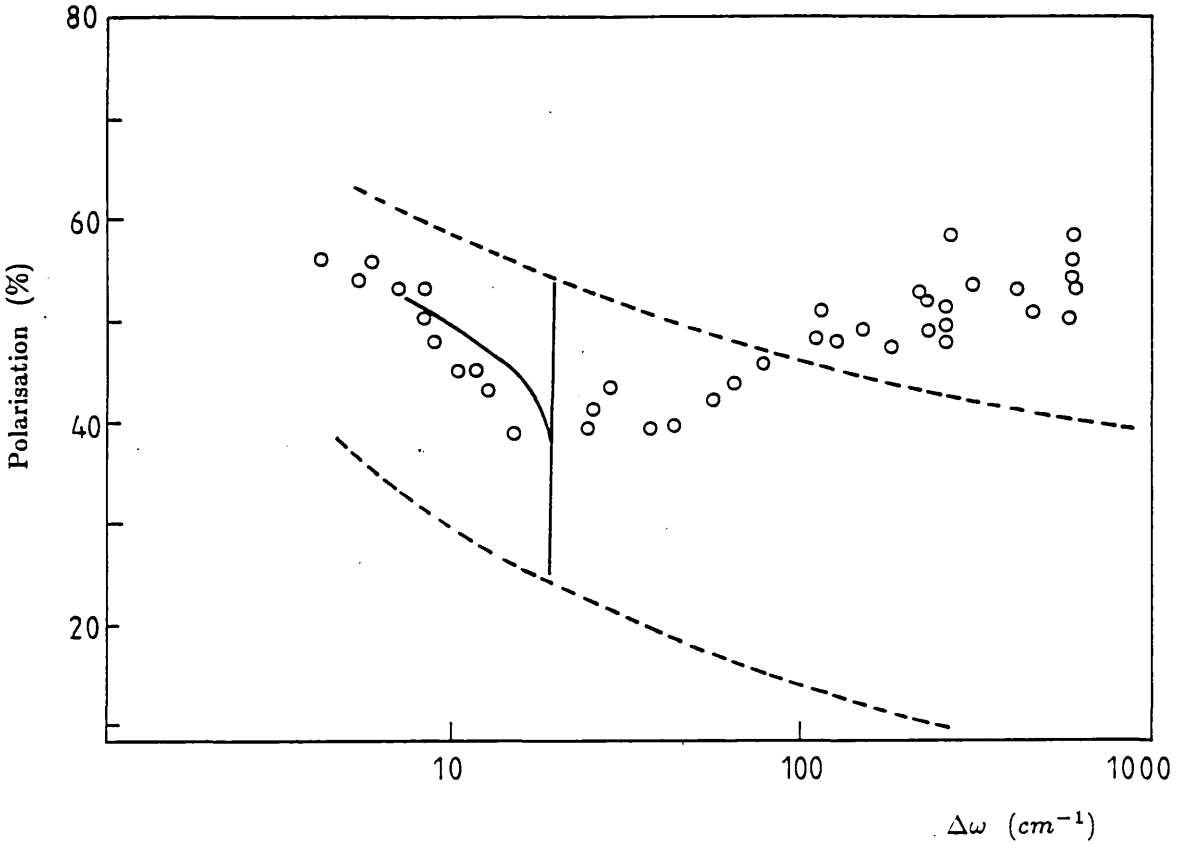


Figure 6.2 Polarisation redistribution spectrum for the red wing of Sr–Ar: Comparison with theory. The full curve is the theory using Lennard–Jones potentials in the molecular model while the dashed curves assume van der Waals potentials. The data points are from Alford (1984). (From Alford *et al.* (1983))

Argon compared with that of Xenon. The dip in the red wing curve reported by Alford *et al.* for Sr–Xe is similarly more pronounced than that for Sr–Ar.

In order to perform a quantitative test of the molecular model the interatomic potentials must be known. The potentials enter the model in two ways : firstly through the $\Delta V_\alpha(r)$ which, when inverted, give $R_\alpha(\Delta V) \equiv R_\alpha(\Delta\omega)$ and secondly through the derivatives of the difference potentials $d(\Delta V_\alpha)/dr$. Within the quasistatic approximation, these determine $g(\Delta\omega)$ and in effect control the relative weight of excitation to the Σ or Π states.

Lewis *et al.* calculated polarization curves for several trial potential forms. They first assumed van der Waals r^{-6} potentials for the ground and excited states and calculated the dashed curves in figure 6.2.

While the assumption of a van der Waals form should give a feel for the kind of difference to be expected in polarization due to Σ or Π excitation the inclusion of $g(\Delta\omega)$ cannot give a good account of the relative strengths of the two components of excitation since the satellite in the Σ state is completely ignored using pure r^{-6} forms. $g(\Delta\omega)$ was accordingly set at either 0 or ∞ and the hypothetical limiting cases of pure Σ and pure Π excitation were calculated.

Carlsten *et al.* (1977) obtained a reasonable fit to the lineshape for $C_6 = 9.8 \times 10^{-31} cm^6 s^{-1}$. Lewis *et al.* adopted this value and calculated *both* curves under this assumption. They also investigated the more realistic case in which the C_6 values differs for the Σ and Π potentials. Withe $C_6(\Sigma)/C_6(\Pi) = 7/4$ they obtained a curve roughly parallel to the Π curve but lowered by $\sim 12\%$ although they did not actually publish this curve.

They assess their curves as follows. They point out that the polarization initially is intermediate between Σ and Π and falls off with roughly the correct slope. The polarization then dips more steeply towards the Σ– only curve at around $\Delta\overline{\nu} = 10^{-20} cm^{-1}$. Lineshape experiments of Carlsten *et al.* (1977) and Harima *et al.* (1981) show a diffuse near wing satellite indicating a minimum in one of the difference potentials with a depth of $\sim 20 cm^{-1}$. General arguments would suggest that the minimum is likely to occur in the Σ difference curve rather than in the Π. Lewis *et al.* take the extra decrease in polarization noted

in this region to be due to the enhancement of Σ excitation resulting from the satellite.

Once the position of the satellite has been passed the polarization climbs to a value close to that predicted by the Π curve. The polarization the increases to even higher values than those predicted by the curve. Lewis *et al.* suggest that the disagreement in this region is due to bent trajectory effects. They argue that at such large detunings the begin to probe the repulsive wall of the ground state potential. They have modelled this effect by assuming that in such strong collisions the atoms act as hard spheres and bounce off each other. This results in less reorientation during a given collision than would occur under the assumption of a straight line trajectory. Since our experiments do nor extend as far into the red wing as those of Alford *et al.* we need not consider this effect in detail.

In order to test eq.2.. directly Lewis *et al.* went on to describe the potentials using a Lennard–Jones form capable of producing the known satellites. (An extreme red wing satellite, attributed to a minimum in the Π difference potential was apparent at $\sim 1000cm^{-1}$). Following Harima *et al.* (1981) and Carlsten *et al.* (1977) they took $\sigma(\Sigma) = 5.9\mathring{A}$, $\epsilon(\Sigma) = 20cm^{-1}$ and $\sigma(\Pi) = 3\mathring{A}$, $\epsilon(\Pi) = 1000cm^{-1}$. Using these potentials the long range behaviour of the Σ and Π states is identical. Insertion of these potentials into equation 2.. yielded the full curve of fig 6.2. The curve reproduces the near wing polarization reasonably well up to the position of the satellite. The cusp in the curve is due to the classical singularity in the lineshape at this position. After the cusp the full curve reverts to the Π–only curve. It is obvious that, just as a semiclassical analysis removes the singularity in the lineshape, the use of a similar analysis to define $g(\Delta\dot{\omega})$ would remove the sharp cusp in the polarization curve. An attempt to do just this has been made by Bieniek (1987) and will be discussed in § 6.4.

6.3 Mercury – Krypton Analysis.

6.3.1 Impact Limit Polarization.

Omont, Smith and Cooper (1972,1973) applied quantum mechanical impact theory to the problem of collisional redistribution. Ballagh and Cooper (1977) used the results of Omont *et al.* to derive explicit expressions for the angular and frequency dependence of radiation scattered by a spatially degenerate atom undergoing collisions. They did this for the three specific cases of a) Linear incident and scattered polarization , b) circular incident and linear scattered polarization and c) unpolarized incident radiation and no monitoring of the scattered polarization. Since their interest was primarily the transport of radiation in stellar atmospheres the full description of case c) was their main goal. We can however make use of their results for case a) which is the one relevant to our experiments. Their equation 25 gives a general expression for the intensity of the scattered radiation including both Rayliegh scatter and the redistributed component. For our purposes we isolate the redistributed component and write, for $J_g = 0$

$$I \propto \left[\frac{2\gamma_{ei}^{(1)} - \gamma_e^{(2)}}{\gamma_e^{(2)}} 3(\epsilon_1.\epsilon_2)^2 + 2\gamma_{ei}^{(1)} \left(\frac{1}{\gamma_e^{(0)}} - \frac{1}{\gamma_e^{(2)}} \right) \right] \tag{6.1}$$

where $\epsilon_{1,2}$ are the vectors describing the orientation of the input and output polarizers. With our experimental geometry we find for $I_{||}$ $\epsilon_1.\epsilon_2 = 1$ and for $I_\perp$ $\epsilon_1.\epsilon_2 = 0$. The correspondence between their notation and that employed in this thesis is given by

$$\gamma_{ei}^{(1)} \equiv \gamma_c + \gamma_n/2$$
$$\gamma_e^{(2)} \equiv \gamma_c^{(2)} + \gamma_n$$
$$\gamma_e^{(0)} \equiv \gamma_c^{(0)} + \gamma_n$$

If we neglect quenching collisions we have $\gamma_e^{(0)} \equiv \gamma_n$. Substitution of these values into eq 6.1 gives $I_{||}$ and $I_\perp$ in terms of γ_c , $\gamma_c^{(2)}$ and γ_n and a constant of

proportionality. This constant drops out when $I_{||}$ and $I_{\perp}$ are substituted into eq.2.51 yielding α in terms of γ_c , $\gamma_c^{(2)}$ and γ_n^*. The result is

$$\alpha = \frac{2\gamma_c - \gamma_c^{(2)}}{2\gamma_c + \gamma_c^{(2)}/\gamma_n} \tag{6.2}$$

and taking the "zero pressure" limit where $\gamma_c^{(2)} << \gamma_n$ we have

$$\alpha = \frac{2\gamma_c - \gamma_c^{(2)}}{2\gamma_c} \tag{6.3}$$

substitution into eq. 2.51 gives

$$P = \frac{6(\gamma_c/\gamma_c^{(2)}) - 3}{6(\gamma_c/\gamma_c^{(2)} - 1} \tag{6.4}$$

Values of γ_c and $\gamma_c^{(2)}$ can be related to the nominal cross sections σ_R and $\sigma^{(2)}$ respectively through eq.2.11. Values of σ_R and $\sigma^{(2)}$ for Hg–Kr reported by various authors are quoted by Lewis (1980) and are shown in table 6.1.

Table 6.1.

σ $(\times 10^{-16} cm^2)$	Authors
$\sigma_R = 227 \pm 10$	J.Buteaux *et al.* (1965,72,74)
$\sigma^{(2)} = 119 \pm 6$	J.Buteaux *et al.* (1965,72,74)
$\sigma^{(2)} = 124 \pm 3$	J.P Barrat *et al.* (1966)
$\sigma^{(2)} = 101 \pm 4$	R.A.Phaneuf *et al.* (1973)
$\sigma^{(2)} = 122$	F.W.Byron *et al.* (1964)

Values of σ_R and $\sigma^{(2)}$ for Hg($^3P_1$—$^1S_0$)–Kr. Taken from Lewis (1980).

Substituting the resulting γ_c and $\gamma_c^{(2)}$ values into equation 6.4 gives an impact limit polarization of $(82 \pm 5)\%$.

Taking the estimate of the collisional duration given in chapter 2 as $\sim 2.6ps$ and using the validity criterion for impact theory, eq.2.15a , we find that the

* γ_c and σ_R are related through equation 2.11. $\gamma_c^{(2)}$ (defined by eq.5.1) is related to $\sigma^{(2)}$ in a similar manner. The superscript (2) refers to alignment.

boundary of the impact region occurs at $\sim 2cm^{-1}$ for Hg–Kr. Our experimental results do not extend closer to linecentre than $5cm^{-1}$ and hence we do not actually probe the impact region properly. However an extrapolation of the trend shown in our data suggests that the agreement between the calculated impact polarization and that which can be inferred experimentally is quite good. This agreement lends confidence in the method of correcting for spurious depolarizing effects described in chapter 5.

This rather high polarization is due to the relatively low value of $\gamma_c^{(2)}$ for the Hg(2537 Å)–Kr interaction. This arises from the fact that the A and B state difference potentials are not well separated in the region of interest. The failure of these curves to separate as well as the analogous Σ and Π potentials in the case of a $^1P_1$–$^1S_0$ transition can be understood by examining the make-up of the A and B states in terms of their Λ components. The electrostatic forces between the colliding atoms still depend on Λ even in the case of an intercombination transition. As pointed out in chapter 3 the A state is made up entirely of Π states whilst the B state contains a mixture of Σ and Π states. The electrostatic difference between collisions proceeding along the A and B states is therefore not as pronounced as it is in the singlet–singlet case where the states are of pure Σ and Π character.

6.3.2 Choice of R_{dc} for Hg-Kr

A simple way of estimating R_{dc} would be to use $\sigma^{(2)} = \pi R_{dc}^2$. Using an average value of $\sigma^{(2)}$ taken from table 6.1 gives R_{dc} =6.1Å. Applying the criterion for R_{dc} used by Lewis *et al.* (1983) given as eq. 2.44b and using the potentials proposed in chapter 3 gives $R_{dc} \sim 6.5\mathring{A}$ for the Hg-Kr system. At this point certain difficulties can be noted in attempting to apply the molecular model in its form described in chapter 2 to the potentials of the Hg($^3P_1$—$^1S_0$)–Kr system.

It should be noted that the maximum energy difference between the A and B states is $\sim 5cm^{-1}$ which is not markedly greater than our estimate of the detuning at which the states decouple. It is in precisely such a situation that the concept of a well defined decoupling radius loses its validity. A physical picture

based on the molecular model is that the atomic orbitals never lock tightly to the molecular axis but merely slew under the influence of the molecular forces. Such a process is badly modelled by the use of a locking radius no matter how small that radius is chosen to be (given that R_α should remain smaller than R_{dc} throughout the region of interest). The molecular model as it stands will always predict *more* reorientation than actually occurs under such circumstances.

It is interesting to compare the maximum polarization (62% for Σ excitation when $R_{dc} = R_\Sigma$) permitted by the molecular model of chapter 2 with calculations for the impact limit polarization. In a system for which the molecular model is truly applicable one would expect these two polarizations to be in rough agreement. In the case of Ba–Ar the impact limit was found to be $(68 \pm 2)\%$. Since the corresponding value for Hg–Kr of 82% is much higher than this the molecular model without modification will be unable to give a high enough polarization in the near wing to be asymptotically compatible with the impact value.

6.3.3 Polarization Curve for Hg–Kr; Red Wing.

We have performed an analysis for Hg–Kr similar to that of Lewis *et al.* (1983) for Sr–Ar. In our case however the potentials used were far more reliable than those available for the Sr–Ar case. Analytical forms were available for the B and X states (Morse potential and Maitland–Smith function respectively) whilst the A state was only available graphically for 30 data points. For convenience we have fitted the A state data to a modified Maitland–Smith function. This was achieved by fixing ϵ and r_m at the values given by Grycuk & Czerwosz (1981) and allowing the α and β parameters to vary to achieve a best fit to the data. The fit was achieved using a least–squares programme available in the NAG library. Since we were only interested in providing a good fit to the data in the region between $\Delta\overline{\nu} = 0 - 40cm^{-1}$, only the data points lying in this region were included in the fitting proceedure. The optimum values were found to be $\alpha = 7.84$ and $\beta = 4.11$. With these values the data points were found to be scattered quite evenly about the fitted curve and the sum of the squared residuals was $13cm^{-2}$ with the worst residual being $\sim 2cm^{-1}$. This reflects

the error in the data as well as error incurred in obtaining the data from the published figure of Grycuk & Czerwosz.

With all the states determined by analytical forms it was easy to differentiate the difference potentials for insertion into $g(\Delta\omega)$. The difference potentials $\Delta V_\alpha(R)$ were inverted numerically to give $R_\alpha(\Delta\omega)$ for substitution into the molecular model. A complication arises when there is an extremum apparent in a given difference potential. When this happens the function $R_\alpha(\Delta\omega)$ is double valued and equation 2.56 is only valid for single valued $R_\alpha(\Delta\omega)$. In order to be able to proceed we make the approximation that excitation to the outer condon point is prevalent and neglect the inner condon point. This is a reasonable approximation for a number of reasons. For a given detuning the slope of the difference potential is always greater for the inner condon point than for the outer one. Since the weighting of the contribution of a particular Condon point is inversely proportional to the slope of the difference potential the inner point will always contribute less for the usual asymmetric well. The inner Condon point will also lose out by virtue of the R_α^2 term in equation 2.55. These arguments become progressively less valid as the minimum in the potential is approached however in this region the difference in the reorientation experienced after excitation at one Condon point or the other becomes small.

At this point the meaning of the Σ and Π labels in equations 2.48—2.58 must be clarified. These labels were introduced in eq 2.48 to draw a distinction between laser excitation to a molecular "angular momentum"state with $\mathbf{J} = 1$ and excitation to a state with $\mathbf{J} = 0$. The equations in chapter 2 were developed in the context of a ${}^1P_1$—${}^1S_0$ transition in which $\mathbf{J} \equiv L$ is a good atomic angular momentum quantum number (correlating with Λ in the molecular picture). In the case of a ${}^3P_1$—${}^1S_0$ transition $\mathbf{J} \equiv J = L + S$ is the relevant angular momentum quantum number (correlating with Ω in the molecular case). Consequently it is necessary to rewrite equations 2.48—2.58 with the labels Σ and Π replaced with $\Omega = 0$ and $\Omega = 1$ respectively.

With these changes made we see that the $A(\Omega = 0)$ state, which is a superposition of $\Lambda = 1(\Pi)$ states, actually behaves like the more depolarizing state of figure 2.8.* The $B(\Omega = 1)$ state which is a superposition of $\Lambda = 1$ and 0 , (ΠandΣ) states acts as the less depolarizing state.

* Compare figure 2.4 showing potentials for the ${}^1S_0$–${}^1P_1$ case with figure 3.5 showing potentials for the ${}^1S_0$–${}^3P_1$ case. In the context of the molecular model calculation the A($\Omega = 0$) state of the latter case plays the same role as the $\Pi(\Lambda = 1)$ state or the former case. The roles of the B($\Omega = 1$) and $\Sigma(\Lambda = 0)$ states are similarly inverted.

The result is that as the satellite in the B state is approached we see enhancement of excitation to a *less* depolarizing state. After the satellite has been passed the polarization collapses to the value prescribed by excitation to the more depolarizing A state alone.

Figure 6.3 shows the results of our calculation superimposed on our experimental data for various values of R_{dc}. As anticipated the curve for $R_{dc} = 6.5\mathring{A}$ lies well below the experimental data. The theoretical curve shows the expected classical cusp similar to the one shown in fig 6.2 but reversed in direction. The curves with R_{dc} smaller than $6.5\mathring{A}$ appear to give better agreement than the one for $R_{dc} = 6.4\mathring{A}$ however these curves should be approached with caution for low detunings since they contain components for which $R_\alpha > R_{dc}$ which is outside the region of validity of eq 2.58. These curves can be expected to give a reasonable fit to the further wing where $R_\alpha < R_{dc}$ despite the low value of R_{dc}. The polarization is seen to hold up well after the position of the satellite but does eventually drop to a value in agreement with the theoretical curves.

6.3.4 Blue Wing.

Insufficient signal was available to perform a systematic detuning experiment in the blue wing. Furthermore the exact form of the interatomic difference potential in the blue wing is not known. We can however make a comment on the limited data available. These data points were taken at detunings corresponding to the peaks of the two satellites at $\Delta\omega = 20cm^{-1}$ and $\Delta\omega = 123cm^{-1}$. Grycuk & Czerwosz discuss the possible origin of these satellites concluding that the distant satellite is of the usual variety and is associated with an extremum in the difference potential. They suggest that the near satellite is likely to be due to bound– free transitions from a high lying vibrational level in the ground state.

We can be sure that the only potential to which excitation can occur in the blue wing is the $B^3 1$ state. Whilst lack of information on the exact form of the potential prevents us from calculating the polarization at $\Delta\omega = 123cm^{-1}$ we note that since excitation occurs entirely to the less depolarizing B state the polarization should be relatively high. This is borne out by the experimental measurement.

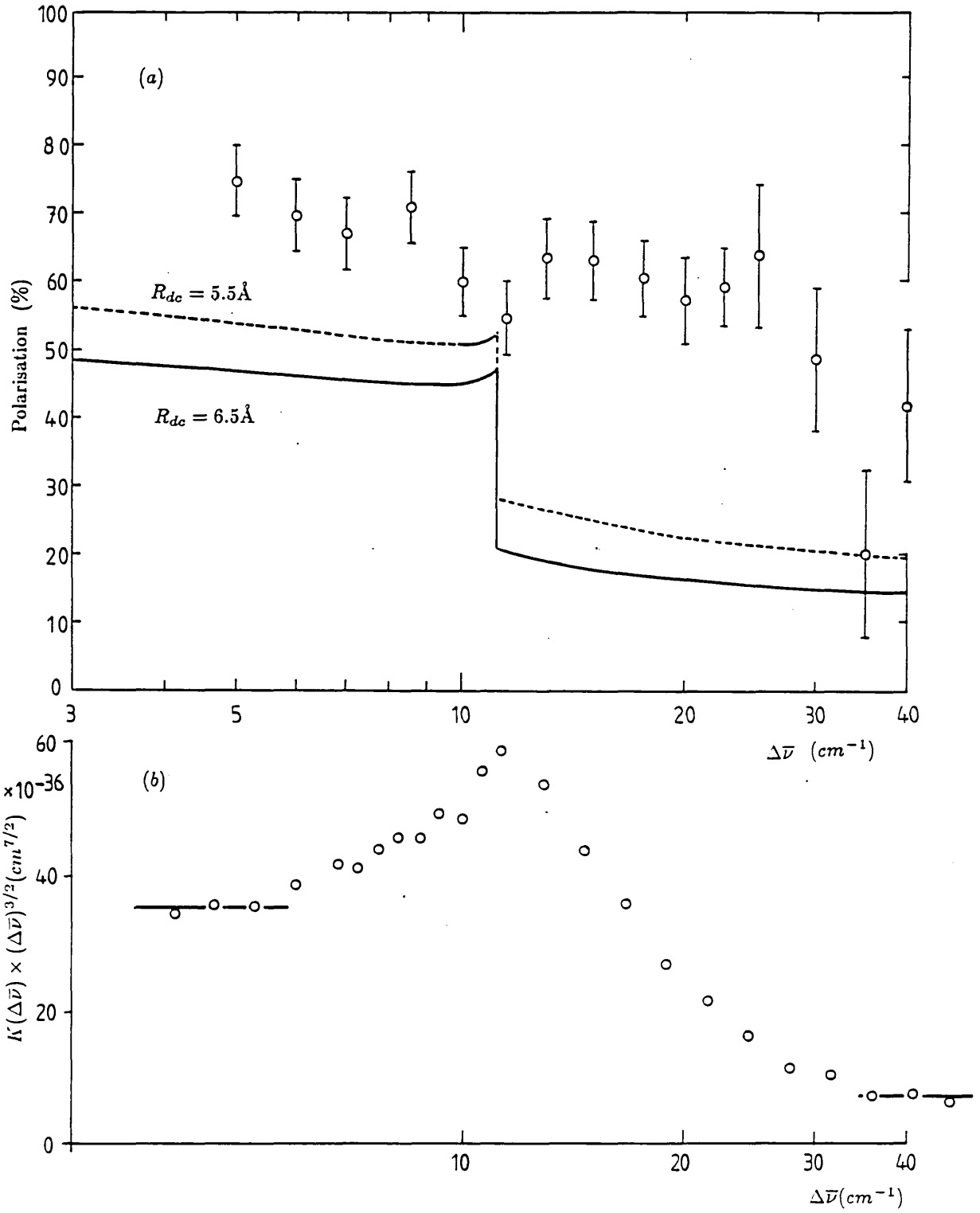


Figure 6.3 Polarisation redistribution spectrum for the red wing of Hg($^3P_1$—$^1S_0$)-Kr: Comparison with theory. (a) Measured polarisations are higher than predicted by the simple molecular model. This results from the proximity of the interatomic difference potentials in the region of interest. The polarisation drops in the far wing to a value in better agreement with theory. (b) Sketch of the satellite taken from the data of Grycuk & Czerwosz. The curves in (a) are the results of the primitive molecular model with purely a purely classical quasistatic satellite. An analysis based on the model proposed by Bieniek (see section 6.4) would use the true form of the satellite, removing the sharp cusp in the polarisation curve.

6.4 Extensions to the Molecular Model.

Bieniek (1987) has addressed some of the deficiencies of the molecular model and has proposed means of correcting for them. Of these deficiencies the most serious is the poor account given of the polarization measured at detunings near the classical satellite. Bieniek proposes a modification of the molecular model that deals with the satellite semiclassically thus smoothing out the cusp in equation 6.. He also proposes a method of dealing with collisions when $R_{dc} < R_\alpha$. Under these conditions the existing formula predicts more reorientation than would actually be apparent. Bieniek applies his modified version of the molecular model to the case of Sr ($^1S_0$—$^1P_1$) + Ar collisions.

In dealing with the satellite two aspects need to be considered. Firstly one must include the possibility of multiple (specifically two) condon points, on a single potential curve. It is necessary to find a way of weighting the contributions to excitation at each condon point. Secondly one must use a semiclassical form for the line profile and thus a semiclassical $g(\Delta\omega)$.

Inspection of eq.2.53 shows that $\alpha^{(2)}(\Delta\omega)$ depends on terms like $\langle\cos(\phi - \theta_\alpha)\rangle$. Bieniek asserts that had the possibility of two condon points occurring on a single potential been allowed in the derivation such terms would appear as

$$\frac{w_1}{w_1 + w_2}\cos(\phi - \theta_\alpha^1) + \frac{w_2}{w_1 + w_2}\cos(\phi - \theta_\alpha^2)$$

where 1 and 2 label the condon points. Here the w_c are weighting factors for excitation to a particular Condon point c and are assumed to be given by the classical quasistatic expression in the form

$$w \propto R_c^2 \left|\Delta V(R_c)\right|^{-1}$$

Although w is singular at the minimum of the difference potential the denominator $w_1 + w_2$ ensures that the weighting factors remain finite. The resulting modification appears as the replacement of the angle average defined by equation 2.57 by

$$\langle \ldots \rangle = \frac{1}{2}\sum_c \frac{R_c^2 \left|\Delta V_\alpha'(R_c)\right|^{-1}}{\left(\sum_n R_n^2 \left|\Delta V_\alpha'(R_n)\right|^{-1}\right)} \int_{-\pi/2}^{\pi/2} \cos(\phi - \theta_\alpha^c)\cos\theta \, d\theta \qquad (6.5)$$

where the $\cos(\phi - \theta_\alpha^c)$ term has been included to stress the dependence on c. For the case of Sr–Ar a quantal $g(\Delta\omega)$ was available from the generalized pressure broadening coefficients reported by Julienne and Mies. Bieniek used this form of $g(\Delta\omega)$ in preference to the classical form given in equation 2.56 resulting in an enhancement of of the depolarization at the satellite position without the unrealistic cusp.

Allowance was made for the situation when $R_\alpha > R_{dc}$ by noting that the rotation occurs in this case is either 2ϕ or 0° depending on whether excitation occurs when the atoms are approaching or receding. He consequently amends the molecular model by changing the terms $\langle\cos(\phi - \theta_\alpha^c)\rangle$ to $\langle\cos(\phi - \frac{\theta}{|\theta|}\phi)\rangle$ in the region where $R_\alpha > R_{dc}$.

Bieniek uses a different method of defining R_{dc} reported by Hertel *et al.* (1985) whereby

$$\left| \int_{R_{dc}}^{\infty} [\Delta V_\Pi(R) - \Delta V_\Sigma(R)]\, dr \right| = \hbar v(\Delta\omega)\, \Delta\eta_{dc} \qquad (6.6)$$

where $v(\Delta\omega)$ is the asymptotic velocity in the excited state and $\Delta\eta_{dc}$ is some critical value of the difference between the local scattering phase shifts for the Σ and Π states. $\Delta\eta_{dc}$ should be $\sim$ unity and acts as a parameter which is adjustable around this value. Figure 6.4 shows his results for $\Delta\eta_{dc} = \pi/4$. These results show reasonable agreement with the quantal results of Julienne and Mies also shown in the figure. He attributes the discrepancy at low detunings to the problem associated with $R_\alpha > R_{dc}$ which becomes more acute in this spectral region.

6.5 Beyond the Molecular Model.

6.5.1 Validity of Approximations

It is apparent that the theory used to analyse our data is incapable of giving a good account the experimental results. We must therefore address the approximations made in formulating the theory and decide which of these is likely to break down in the case of the Hg($^3P_1$—$^1S_0$)–Kr interaction. The following

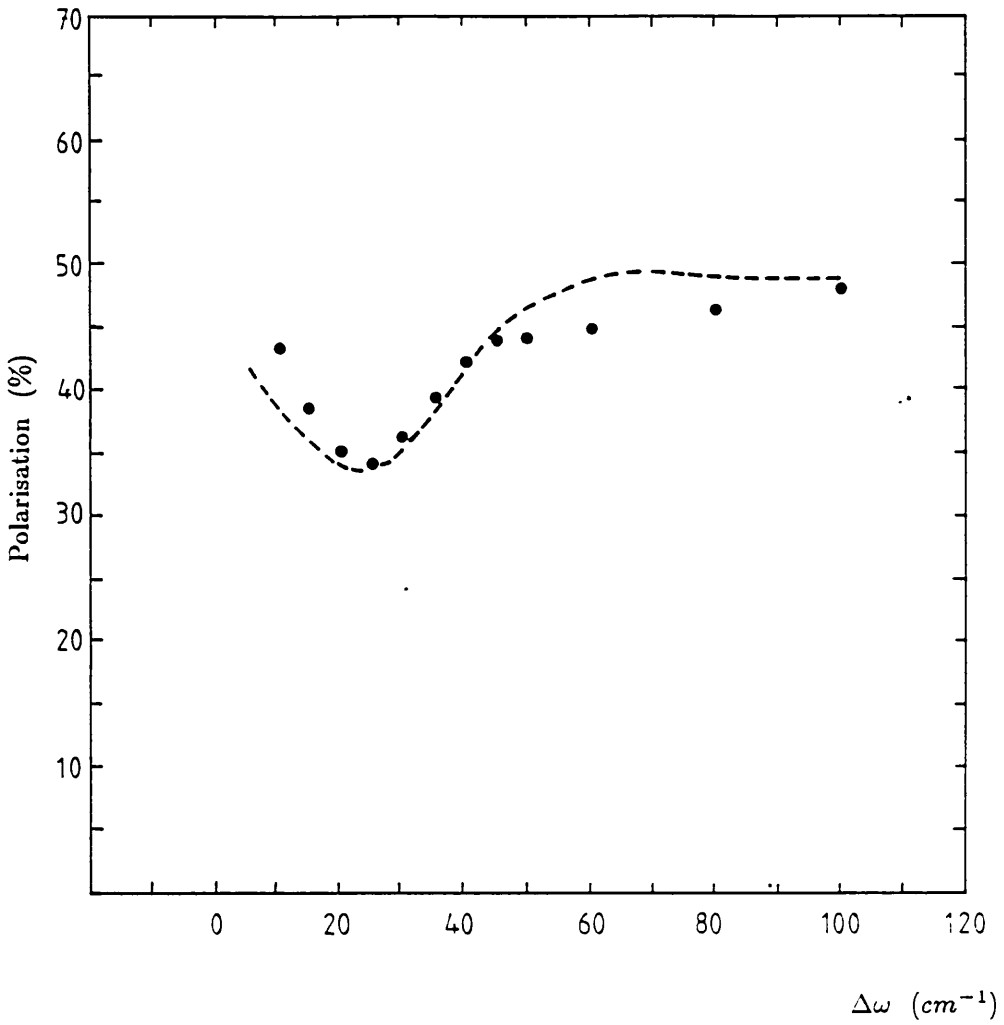


Figure 6.4 Improved theoretical curves for the polarisation redistribution spectrum of Sr–Ar. The dashed curve is the result of Bieniek's improved molecular model calculation. •: close–coupled, quantal non–adiabatic calculations (Julienne & Mies (1986)). Note that although the classical satellite occurs at $\sim 20cm^{-1}$ the polarisation dip continues out to $\sim 40cm^{-1}$. (From Bieniek (1986))

approximations are made in formulating the molecular model: The atoms are taken to follow *classical trajectories* and to be excited *quasistatically* at Condon points. The model also assumes that this excitation occurs *independently* to the $\Omega = 0$ and $\Omega = 1$ states. The atoms are then taken to undergo *adiabatic reorientation* until a fixed *decoupling radius* is reached. The last three points essentially assume that there is no mixing of the molecular states either at excitation, during the rotation or after decoupling. The following sections examine the validity of these assumptions in turn.

6.5.2 Classical Trajectories and Quasistatic Excitation

By treating the problem of two interacting particles in their centre of mass frame the dynamics can be reduced to those of a single "particle" of reduced mass μ moving in a potential V(R). The assumption of classical trajectories breaks down if the de Broglie wavelength of the "particle" is of the order of a typical scale length for the interatomic potential. Taking $p = \mu v_{rel}$ and using $\mu v_{rel}^2/2 = 3kT/2$ we find $p = \sqrt{3kT\mu}$. Using the de Broglie relation $\lambda = h/p$ we find $\lambda = 0.19$Å for Hg–Kr thermal collisions at room temperature. The minima in the A, B and X potentials occur at ~ 4Å which can be taken as a measure of the scale of the potential. The assumption of classical trajectories is therefore good for the collisions we have studied. If any discrepancy occurs as a result of this assumption it will occur near the turning points where dV/dR is large ie. the potential changes appreciably over a de Broglie wavelength.

Also related to the classical path assumption is the question of the angular momentum of the collisions or equivalently the rotational energy level spacing. Classically the angular momentum L and the impact parameter b are related through

$$L = b\mu v_{rel} \tag{6.7}$$

The assumption of well defined trajectories implies that b can take any value. However we know the left hand side of eq 6.7 to be quantized according to

$$L = \sqrt{l(l+1)}\hbar \tag{6.8}$$

It is an example of the correspondence principle that at large values of l the distribution of allowed impact parameters becomes almost continuous. Combining equations 6.7 and 6.8 and assuming an impact parameter of 3Å we find $l \sim 100$ for the collisions we have been considering. At such high values of l we can replace $\sqrt{l(l+1)}$ with l with negligible effect and the system behaves to all intents and purposes classically.

The condition for quasistatic excitation is given as equation 2.15b. This condition is well fulfilled for Hg($^3P_1$—$^1S_0$)–Kr at the detunings investigated. However, as previously pointed out, the theory itself is inadequate in certain circumstances. Classical quasistatic theory fails to predict the correct form for the satellite. This particular aspect has been dealt with using the analysis of Bieniek discussed in § 6.4.

6.5.3 Excitation, Reorientation and Decoupling.

The work of Hertel *et al.* (1985) and Grosser (1981) has shown the concept of a locking radius to be useful when the potentials involved separate rapidly. As has been discussed the concept is not useful when the potentials remain close together over a large region of R. Since this is the case for Hg($^3P_1$—$^1S_0$)–Kr we now discuss ways in which the theory could be amended to take account of this problem. Since the model is based on the three processes of excitation, rotation and decoupling we examine these three processes in turn.

The molecular model assumes that, at excitation, dipoles of either pure $\Omega = 0$ or pure $\Omega = 1$ character are created. Excitation therefore occurs to states with the well defined wavefunctions Ψ_0 (pointing along the molecular axis) or Ψ_1 (at right angles to the molecular axis). In an exact quantum mechanical treatment of this aspect, excitation occurs to a state whose wavefunction is a linear superposition of these two wavefunctions, $\Psi = C_1\Psi_1 + C_0\Psi_0$. In a perturbation approach the C's, which control the admixture of the states involved, are inversely proportional to the energy difference between the states. When, as in our case, excitation occurs at points where the energy separation of the states is small, the correct form of the wavefunction must be used.

In the inexact treatment of the molecular model it is assumed that the Ψ_1 and Ψ_0 wavefunctions rotate adiabatically. That is the rotation does not induce transitions between the two states. These wavefunctions are therefore independent solutions of the Schröedinger equation. In reality the proximity in energy of the two states will lead to further mixing between them during the collision. In order to describe this situation we must solve a pair of coupled equations. The wavefunctions $\Psi = C_1\Psi_1 + C_0\Psi_0$ are the solutions of these coupled equations.

In the exact method it is unnecessary to introduce the concept of a decoupling radius since the behaviour at all R is taken care of automatically once the correct form of the wavefunction is used.

In summary the effects of assuming quasistatic excitation and classical trajectories are either negligible or can be allowed for by making the reasonably simple amendments to the model as described in § 6.4. Far more serious difficulties arise, for our system, from the assumptions of incoherent excitation, adiabatic reorientation and the use of a decoupling radius. The next step would therefore be to retain the former approximations but to treat the excitation and reorientation processes as described above.

It is possible to treat the entire problem quantum mechanically. Work along these lines is under way at present in this laboratory. The drawback of the full quantum mechanical calculation is that it does not lend itself to simple physical interpretation.

Chapter 7

Conclusions and Suggestions for Further Work.

7.1 Summary.

We have designed and built the experimental rig described in chapter 4 and have used it to perform a sensitive photon counting experiment. The chief experimental problem was the low signal level. This was due in large part to over optimistic claims (made by the suppliers) for the efficiencies of the various frequency doubling schemes available. The experiment was made possible by reducing the amount of background light to a level comparable to the photomultiplier dark current. We have measured the polarization of collisionally redistributed light in the Hg($^3P_1$—$^1S_0$)—Kr system, as a function of detuning over the range 0—40cm^{-1} in the red wing and at selected detunings in the blue wing.

Due to the low signal level, the experiment was performed in a regime in which the polarization measured did not result solely from the collisional dynamics but was also affected by other "spurious" effects. These effects have been corrected for and the "true" polarization curve has been retrieved. Of all the spurious effects considered, our method for dealing with radiation trapping is the least satisfactory and this is the source of the greatest systematic error. The chief source of random error is shot noise.

We have attempted to analyse our results using the molecular model outlined in chapters 2 and 6. A knowledge of the interatomic potentials is essential to this analysis. We have therefore examined potentials available in the literature and suggested which of these are the most accurate in the region of R of interest to us.

7.2 Conclusions.

The choice of Hg($^3P_1$—$^1S_0$)–Kr as a system worthy of study has been supported throughout this thesis by the availability of the interatomic potentials, allowing

quantitative tests of theory. However, even the qualitative features of our polarization curve differ from those of the corresponding curve for Sr($^1P_1$—$^1S_0$)–Ar. The chief qualitative feature in that system was the dip in the polarization near the minimum in the Σ difference potential. It has been shown that in the case of Hg($^3P_1$—$^1S_0$)–Kr this trend is reversed and we see an enhancement of the polarization near the minimum in the $\Omega = 1$ difference potential. Just as this qualitative feature allowed Alford *et al.* to definitively label the potential curves as Σ and Π we are able, through this work, to label the Hg($^3P_1$—$^1S_0$)–Kr potentials definitively as $\Omega = 0$ and $\Omega = 1$.

The stated aim of this work was to provide a test of the molecular model presented in chapter 2. It would be unfair to attribute the failure of our analysis of chapter 6 to account for our data to the general inadequacy of the theory used. The problem clearly lies in the fact that some of the underlying assumptions of the model are invalid for a system such as ours in which the $\Omega = 0$—$\Omega = 1$ potential difference is small.

The model as it stands has therefore not been tested in a region where it can be expected to be adequate. An alternative approach to performing such a test would be to conduct experiments to elucidate the interatomic potentials for Sr—RG and Ba—RG systems since for these systems the polarization data available in the literature is excellent. Such experiments are difficult to perform but have been proposed and are being pursued by other experimenters in the field.

It is arguable that once the stated aim of testing the molecular model had been achieved the logical next step would have been to examine systems for which the validity criteria of the inherent approximations are less well satisfied. In order that such a model be worthy of pursuit it should be widely applicable and should survive, with little modification, reasonable changes in the system studied. The purpose of examining such marginal systems would be to test the range of applicability of the molecular model. Hg($^3P_1$—$^1S_0$)–Kr is just such a marginal system and our results bring into sharp focus the inadequacies of the molecular model. The possible benefits of extending this work to systematically cover all the rare gasses will be discussed in § 7.3.2.

7.3 Suggestions for Further Work.

7.3.1 Improvements to the Experimental set up.

It would be possible to make some radical improvements to the experimental set up. Firstly, in the last year a new nonlinear crystal capable of frequency doubling to 2537Å has become available. Beta phase Barium Borate (BBO) has quoted efficiencies well in excess of 10% . The resulting factor of ten improvement in the signal level would make practicable a far more systematic survey of Hg($^3P_1$—$^1S_0$)–RG interactions in both the red and blue wings. A further increase in the signal level could be achieved by removing the monochromator from the experimental rig and replacing it with an ultra violet Pöckels cell. Since the timescale of the fluorescence is $\sim 100ns$ it would be possible to gate against the prompt Rayleigh and specular scatter temporally rather than in frequency. The gains in signal would come from dispensing with the inefficient dispersive element (grating) and through the total absence of slits which hamper the throughput.

A new cell is presently under construction which should overcome many of the shortcomings of the one used in this work. The main drawbacks with the old cell were that it could not be heated uniformly and that it did not hold its vacuum particularly well when sealed off. The first of these meant that the vapour pressure of Hg was not easily or effectively controllable. It was only possible to obtain pressures at, or lower than the room temperature vapour pressure. A well controlled heatable cell along with an increase in the experimental signal would allow us to perform a far more satisfactory experiment to resolve the effect of radiation trapping.

If this effect could be well characterized a further increase in signal might be achieved at higher vapour pressures with a sacrifice in the level of the measured polarization. It is not however clear whether there would be any net gain in adopting such a proceedure.

The second drawback, that of the vacuum not being well maintained in the absence of pumping, meant that we were limited to short ($\sim$ 1 hour) runs on a given gas fill. Care had to be taken that signal resulting from collisions

with spurious impurity gasses was not allowed to become so large as to seriously affect the experimental accuracy. A well sealed and baked active cell volume would lend greater ease of experimental operation.

7.3.2 Further Experiments.

An obvious extension to the present work would be to perform similar experiments in the Hg($^3P_1$—$^1S_0$)–Xe system since the qualitative features should be more pronounced with this heavier, more polarizible perturber. Furthermore, work has been done on the interatomic potentials for Hg($^3P_1$—$^1S_0$)–Xe (Fuke *et al.* 1986, Grycuk & Findeisen 1983, Lam & Gallagher 1978). It is likely that the A—B state separation is greater for this system than for Hg($^3P_1$—$^1S_0$)–Kr, whilst the decoupling radius would occur at a smaller state separation as a result of the longer collision time τ_c. Hg($^3P_1$—$^1S_0$)–Xe should therefore be closer to an ideal system in which the molecular model might be expected to work. A systematic study using all the rare gasses would expose in a very clear way the onset of difficulties with the molecular model, as one progresses from Xe down to He.

Grycuk & Czerwosz (1981) discuss the origins of the blue satellites in the Hg($^3P_1$—$^1S_0$)–RG line profiles. We have shown that the polarization of the collisionally redistributed light at these satellites is high but were unable to perform a systematic study in the blue wing due to the sharp decrease in experimental signal in this spectral region. A full study of the blue wing polarization curve could help greatly in resolving the origin of these satellites.

Another direction which would be experimentally trivial given the present apparatus would be to perform similar experiments in mixtures of Hg with molecular gasses such as N_2 and CO_2. In such instances quenching collisions become important and the depolarization cross sections, particularly that of CO_2 are very large.

Another type of experiment originally envisaged for this experimental rig was to probe Hg–Hg resonance collisions since the potentials for this system are given by a simple analytical form. In order to achieve any appreciable signal it would be necessary to work at high mercury pressures and a scheme to overcome

the effects of radiation trapping would need to be employed. One scheme would be to use different isotopes of Hg as perturber and emitter and to depend on the isotope shift to make the cell transparent to the emitted fluorescence. Another scheme would be to shift the atom out of resonance using the Stark shift in a strong laser field.

The present laser and detection system could be adapted to work with a molecular beam rather than a thermal cell. At the simplest level one could perform bound state spectroscopy on van der Waals dimers in such a beam. By using a dye laser oscillator with a smaller bandwidth ($\sim 1GHz$) one could resolve the rotational structure of the bound–bound molecular spectrum. This would allow a full RKR analysis and a corresponding increase in the quality of the interatomic potentials available for testing theories. Such experiments for Hg–He, Hg–Ne, and Hg–Ar have recently been reported by Yamanouchi *et al.* (1988).

One could also perform experiments in which a laser photon is used to photodissociate the van der Waals molecules thus forming a different type of half–collision process. The availability of information on the two different types of half–collision process (collisional redistribution and photodissociation) for the same system, would be unique.

References.

Alford W J, (1984) *Thesis.* University of Colorado.

Alford W J, Burnett K, Cooper J, (1983) Phys. Rev. A **27**, 1310.

Alford W J, Andersen N, Burnett K and Cooper J, (1984) Phys. Rev. A **30** 2366.

Allard N and Kielkopf J, (1982) Rev. Mod. Phys. **54**, 1103.

Andersen N, (1985) in proc. of XII *Summer School on Quantum Optics.* edited by J. Fiutak and J. Mizerski.

Anderson P W and Talman J D (1956) *Pressure broadening of spectral lines at general pressures.* Bell System Technical Publication No. 3117 (New Jersey).

Ballagh R J and Cooper J, (1977) Astrophys. J. **213**, 479.

Barrat J P, (1959a) J. Phys. Radium (Paris) **20**, 541.

Barrat J P, (1959b) *ibid.* **20**, 633.

Barrat J P, (1959c) *ibid.* **20**, 657.

Barrat J P, Casalta D, Cojan J L and Hamel J, (1966) J. de Phys. **27**, 608.

Behmenburg W, Kroop V and Rebentrost F, (1985) J. Phys. B **18**, 2693.

Ben Lakhdar Z B, Perrin D and Lennuier R, (1976) J. de Phys. **37**, 831.

Ben Lakhdar Z, Perrin D and Lennuier R, (1978) J. de Phys. **39**, 137.

Bieniek R J, (1987) Phys. Rev. A **35**, 3663.

Blum K, (1981) *Density Matrix Theory and Applications.* (Plenum Press, London.)

Bransden B H and Joachain C J, (1983) *Physics of Atoms and Molecules.* (Longman, London.)

Brink D M and Satchler G R, (1962) *Angular Momentum.* (Clarendon Press, Oxford.)

Brossel J and Bitter F, (1952) Phys. Rev. **86**, 308.

Burnett K, Cooper J, Ballagh R J and Smith E W, (1980a) Phys. Rev. A **22** 2005.

Burnett K and Cooper J, (1980b) *ibid.* **22**, 2027.

Burnett K and Cooper J, (1980c) *ibid* **22**, 2044.

Burnett K, (1985) in *Spectral Line Shapes, Vol. 3,* edited by F. Rostas (de Gruyter, Berlin, 1985), p. 353.

Burnett K, (1985) Physics Reports. **118**, 339.

Buteaux J, Schuller F and Lennuier R, (1974) J. de Phys. **35**, 361.

Buteaux J and Lennuier R, (1965) Comptes Rendus **261**, 671.

Buteaux J, (1972) *Thesis.* University of Paris.

Byron F W and Foley H M, (1964) Phys. Rev. **124**, A625.

Carlsten J L, Szöke A and Raymer M G, (1977) Phys. Rev. A **15**, 1029.

Cooper J, (1967) Rev. Mod. Phys. **39**, 167.

Cooper J, (1979) Astrophys. J. **228**, 339.

Corney A, (1977) *Atomic and Laser Spectroscopy.* Oxford Univ. Press, Oxford.

Corney A and McGinley J V M, (1981) J. Phys. B **14** 3047.

Drummond D L and Gallagher A, (1974) J. Chem. Phys. **60**, 3426.

Dunning F B, Tittel F K and Stebbings R F, (1973) Optics Comm. **7**, 181.

D'Yakonov M I and Perel V I, (1965) Soviet Phys. JETP **20**, 997.

Foley H M, (1946) Phys. Rev. **69**, 616.

Foth H J, Polanyi J C and Telle H H, (1982) J. Chem. Phys. **86** 5027.

Fuke K, Saito T and Kaya K, (1984) J. Chem. Phys. **81**, 2591.

Fuke K, Saito T, Kaya K, Yamanouchi K, Fukuyama J, Horiguchi H and Tsuchiya S, (1986) J. Chem. Phys. **85**, 1806.

Greene C H and Zare R N, (1982) Ann. Rev. Chem. **33**, 119.

Grosser J, (1981) J. Phys. B **14**, 1449.

Grycuk T and Czerwosz E, (1981) Physica C **106**, 431.

Grycuk T and Findeisen M, (1983) J. Phys. B **16**, 975.

Hanle W, (1924) Z. Phys. **30**, 93.

Hänsch T W, (1972) Appl. Opt. **11**, 895.

Harima H, Fukuzo Y, Tachibana K and Urano Y, (1981) J. Phys. B **14**, 3069.

Hedges R E M, Drummond D L and Galagher A, (1972) Phys. Rev. A **6**, 1519.

Hertel I V, Schmidt H, Bähring A and Meyer E, (1985) Rep. Prog. Phys. **48**, 375.

Holtsmark J, (1919) Ann. Phys. (Leipzig) **58**, 577.

Huber D L, (1969a) Phys. Rev. **178**, 93 ; (1969b) *ibid* **187**, 392.

Jablonski A, (1931) Z. Phys. **70**, 723.

Kent L W J, (1985) *Thesis.* University of London.

Kong C M and Chakrabarty M R, (1973) J. Phys. Chem. **77**, 2668.

Kroop V and Behmenburg W, (1980) Z. Phys. A **294**, 299.

Kuhn H G, (1934) Philos. Mag. **18**, 987.

Lam L K and Gallagher A, (1978) J. Chem. Phys. **68**, 4411.

Lenz W, (1924) Z. Phys. **25**, 299.

LeRoy R J, (1972) J. Chem. Phys. **57**, 573.

LeRoy R J and Bernstein R B, (1970) Chem. Phys. Lett **5**, 42.

Lewis E L, (1980) Phys. Rep. **58**, 1.

Lewis E L, Harris M, Alford W J, Cooper J and Burnett K, (1983) J. Phys. B **16** 553.

Lindholm E, (1945) Ark. Fys. A **32**, No. 17, 1.

Littman M and Metcalf H, (1978) Appl. Opt. **17**, 2224.

London F, (1930a) Z. Phys. **63**, 245.

London F, (1930b) Z. Phys. Chem. (Leipzig) B **11**, 222.

Loudon R, (1983) *The Quantum Theory of Light.* Clarendon Press, Oxford.

Maitland G C, Rigby M, Smith E B and Wakeham W A, (1981) *Intermolecular forces – Their origin and determination.* Clarendon Press. Oxford.

Mies F H and Julienne P S, (1986) Phys. Rev. A **34**, 3792.

Mihalas D, (1970) *Stellar Atmospheres.* (Freeman, San Fransisco.)

Mollow B R, (1970) Phys. Rev. A **2**, 76.

Nienhuis G, (1983) J. Phys. B **16**, 1.

Nienhuis G and Schuller F, (1977) Physica (Utrecht) C**92**, 397.

Omont A, (1965a) J. de Phys. **26**, 26.

Omont A, (1965b) C. R. Hebd. Séanc. Acad. Sci. (Paris) **260**, 3331.

Omont A, Smith E W and Cooper J, (1972) Astrophys. J **175**, 185; (1973) *ibid.* **182**, 283.

Percival I C and Seaton M J, (1958) Phil. Trans. Roy. Soc. (London) A **251**, 113.

Phaneuf R A, Pitre J, Hammond K and Krause L, (1973) Can. J. Phys. **51**, 724.

Powers J R and Cross R J, (1972) J. Chem. Phys. **56**, 3181.

Rayleigh, Lord (1922) Proc. R. Soc. **102**, 190.

Sando K M and Wormhoudt J, (1973) Phys. Rev. A **7**, 1889.

Saxon R P, Olson R and Liu B, (1977) J. Chem. Phys. **67**, 2692.

Shoshan I, Danon N N and Oppenheim U P, (1977) J. App. Phys. **48**, 4495.

Smith K M, Rulis A M and Scoles G, (1977) J. Chem. Phys. **67**, 152.

Szudy J and Baylis W E, (1975) J. Quant. Spectrosc. Rad. Transfer **15**, 641; (1977) *ibid.* **17**, 681.

Tanaka Y and Yoshino K, (1970) J. Chem. Phys. **53**, 2012.

Telle H H, (1984) Act. Phys. Pol. **A66**, 359.

Thomann P, Burnett K and Cooper J, (1980) Phys. Rev. Lett. **45**, 1325

Thorne A P, (1977) *Spectrophysics.* (Chapman and Hall, London.)

Vidal C R, Cooper J and Smith E W, (1970) J. Quant. Spectrosc. Rad. Transfer **10**, 1011.

Vigué J, Grangier P, Roger G and Aspect A, (1981) J. de Phys. Lett. **42**, L531.

Voslamber D, (1969) Zs. Naturforsch. **249**, 1458.

Voslamber D and Yelnik J B, (1978) Phys. Rev. Lett. **41**, 1233.

Voslamber D and Yelnik J B, (1979) Astrophys. J. **230**, 184.

de Vries A, (1982) Comm. At. Mol. Phys **11**, 157.

Wallenstein R and Zacharias H, (1980) Optics Comm. **32**, 429.

Weisskopf V, (1932) Z. Phys. **75**, 287.

Weisskopf V and Wigner E (1930) Z. Phys. **63**, 54. English translation in *Atomic Spectra.* by W R Hindmarsh, Pergamon Press, Oxford (1967).

Wood R W and Ellet A, (1924) Phys. Rev. **24**, 243.

Yamanouchi K, Isogai S, Okunishi M and Tsuchiya S, (1988) J. Chem. Phys. **88** (1), 205.

Acknowledgements.

I thank my supervisor Dr.K.Burnett for his constant enthusiasm and faith and for many enlightening discussions during my time at Imperial College. I also thank my colleagues Mr.W.Steer, Mr.I.Harris, Ms.C.Richter, and Dr.L.Kent for their invaluable help in diverse aspects of the experiment.

The experiment could not have been successful without the expert help and advice of Mr.P.Ruthven with respect to all things technical. I would also like to thank Dr.R.H.Phillips and his colleagues for their help with the apparatus. I thank all my friends in the Spectroscopy group, including all those mentioned so far in a scientific context, for their support and good humour and for making my time as a PhD student so enjoyable. A special vote of thanks goes out to Dr R.Clarke, Mr.P.Dwyer and Ms.A.Vrielink for their support in my duties as subwarden of Linstead Hall.

I gratefully acknowledge the financial support of the S.E.R.C.

I thank Helen for everything else and for being ... Helen.

